UCSF
UC San Francisco Electronic Theses and Dissertations

Title
Nanomechanical properties, composition, and mineral-density distributions of late-stage atherosclerotic calcifications

Permalink
https://escholarship.org/uc/item/2ff1x948

Author
Coughlin, Dezba Gannett

Publication Date
2005

Peer reviewed|Thesis/dissertation

eScholarship.org Powered by the California Digital Library
University of California

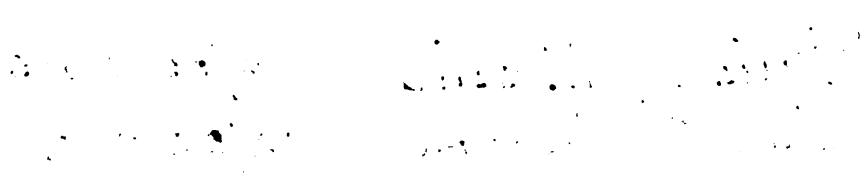

To the three most important people in my life:
my grandmother, mother, and husband

HARVARD LIBRARY

Acknowledgements

First, I would like to thank my grandmother, mother, and husband for all that they have done for me. Abuelita, thank you for always giving me your joy, love, and amazing food. Mom, thank you for always believing in me, giving me your unconditional love, and being supportive and encouraging. Ruben, of all the people, you are the one that most understands what I have gone through to reach this goal. I cannot thank you enough for all your love, encouragement, and support day to day. I do not know how I would have done it without you.

Prof. Pruitt, thank you for your patience and for giving me the freedom to explore and to teach. These opportunities have made me mature both intellectually and emotionally. The people in your lab have also been invaluable to my success. David, thank you for working with me and inspiring me to obtain a PhD. Jingli, Rita, and Donna, thank you for being my mentors, taking the time to teach me various techniques, and guiding me through graduate school. Ayyana, it was always nice to have a partner in crime during the quals process and while teaching and writing. Cheng, thank you for showing me how to use the FTIR and always encouraging me. It was also always nice to have the rest of the *MPG* to go to either when I needed guidance or simply, a break. During the writing process, I would like to thank Ruben, Donna, Katherine, Galateia, and especially my father for thoroughly editing my work.

I cannot forget the professors and friends outside of the lab that have also been so kind. Prof. Saloner and Prof. Nelson, you two were the only two professors, besides Prof. Pruitt, that encouraged me to continue with the PhD. I also appreciate that Prof. Keaveny,

Prof. Halloran, and Prof. Majumdar were kind enough to let me use their equipment and laboratory space. I especially need to thank Galateia for her suggestions on my FTIR project. Andrew, you were always very patient while explaining to me how to use the FTIR and micro-CT. I could not have done it without you.

Outside of the academic world, I really need to thank the rest of my family and friends for helping me keep my sanity. I especially need to thank *La Comadre* and *The Girls* for always taking care of me. All of you have been kind enough to understand my commitment to finishing this work although I have missed many events with family and friends. I would also like to recognize the *Club Cena* crew for the amazing dinners, salsa nights, and support. Finally, Dad, Ruben, Jessica, and Katherine, thank you for coming through at the end.

Abstract

Nanomechanical Properties, Composition, and Mineral-Density Distributions of Late-Stage Atherosclerotic Calcifications

by

Dezba Gannett Coughlin

Doctor of Philosophy in Bioengineering

University of California, Berkeley

Professor Lisa A. Pruitt, Chair

Atherosclerosis is a cardiovascular disease that is the leading cause of death in the United States. It is characterized by thickening of the arterial wall due to the accumulation of lipids, macrophages, smooth muscle cells, necrotic debris, calcifications, thrombosis and/or hematoma, which together form what is known as a plaque. Clinical events most commonly occur from plaque occlusions or ruptures. Although some factors affecting a plaque's vulnerability to rupture are known, it is not clear whether calcifications increase or decrease the probability of rupture. However, evidence suggests that calcifications affect the functionality and remodeling of arteries and sometimes intervene in the treatment of diseased arteries.

To better access how calcifications affect plaque vulnerability, arterial remodeling, and the treatments for atherosclerosis, it is imperative to learn more about the composition and physical properties of atherosclerotic calcifications. Hence, the objective of the present study is to further characterize atherosclerotic calcifications. The elastic mechanical properties were measured using nanoindentation for future use in finite

element models; the composition of calcifications was analyzed using Fourier transform infrared (FTIR) spectroscopy to ascertain the similarities and differences in the biomineralization process of bone and atherosclerotic calcifications; nanoindentation was coupled with FTIR to determine structure-property relationships; and micro-computed tomography (μCT) was used to determine the mineral-density distribution of atherosclerotic calcifications in order to evaluate general calcification-growth patterns.

In the nanoindentation study, improved sample-preparation techniques narrowed the range of reduced elastic moduli as compared to a previous study. In addition, the coupling of nanoindentation to FTIR suggested that, as with other calcified materials, an increase in mineral content increases the elastic modulus. Additional FTIR studies revealed that, although the biomineralization processes of bone and atherosclerotic calcifications may produce a similar mineral phase, other factors can raise the mineral content of atherosclerotic calcifications and make its mineral slightly more crystalline. The μCT study revealed that calcification formation may occur in complex growth patterns or in clearly concentric or sedimentary-like depositions.

Together, the results obtained in the present study provide initial information about the mechanical properties of calcifications and yield important clues about the development and progression of atherosclerotic calcifications.

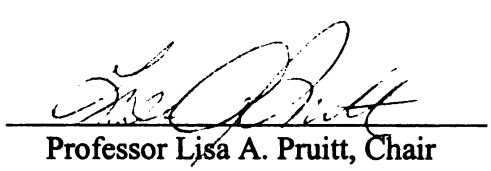

Professor Lisa A. Pruitt, Chair

Contents

List of Tables ..... **xi**

List of Figures ..... **xii**

Chapter 1. **Introduction** **1**

1.0. Atherosclerosis: An Overview, 1
1.1. Vulnerable Plaque, 5
1.2. Research Focus, 6
1.3. Objectives of this Work, 9
1.4. Outline of Thesis, 10
1.5. References, 12

Chapter 2. **Background** **20**

2.0. Introduction, 20
2.1. Anatomy of Normal Arteries, 20
2.2. Atherosclerosis, 21
  2.2.1. Development of Atherosclerosis, 21
  2.2.2. Plaque Vulnerability, 24
2.3. Arterial Calcifications and Bone, 26
  2.3.1. Function of Arterial Calcifications and Bone, 26
  2.3.2. Composition of Arterial Calcifications and Bone, 27
  2.3.3. Structure of Arterial Calcifications and Bone, 28
  2.3.4. Biomineralization of Arterial Calcifications and Bone, 30
2.4. Summary, 33
2.5. References, 34

Chapter 3. **Experimental Techniques** **47**

3.0. Introduction, 47
3.1. Nanoindentation, 47
  3.1.1. Triboindenter, 48
  3.1.2. Contact Mechanics Theory, 49
  3.1.3. Applying the Theory of Contact Mechanics, 51
3.2. Fourier Transform Infrared Spectroscopy, 53
  3.2.1. Spectrometer, 54
  3.2.2. Fourier Transform Infrared Spectroscopy Physics, 55
  3.2.3. Fourier Transform Infrared Spectroscopy Spectrum, 59
3.3. Micro-Computed Tomography, 61
  3.3.1. Micro-Computed Tomography System, 61
  3.3.2. Micro-Computed Tomography Physics, 63

3.3.3. Image Reconstruction, 65
3.3.4. Beam Hardening Corrections, 67
3.3.5. Mineral Density Calibration, 68
3.4. Conclusions, 69
3.5. References, 70

Chapter 4. **Nanomechanical Properties of Mineralized Tissue..... 85**

4.0. Introduction, 85
4.1. Materials and Methods, 89
4.1.1. Sample Preparation, 90
4.1.2. Roughness, 91
4.1.3. Hold Time Segments and Loading/Unloading Rates, 93
4.1.4. Nanoindentation of Atherosclerotic Calcifications and Bone, 94
4.1.5. FTIR-ATR of Atherosclerotic Calcifications and Bone, 95
4.2. Results and Discussion, 95
4.2.1. Roughness, 95
4.2.2. Hold Times and Loading/Unloading Rates, 98
4.2.3. Atherosclerotic Calcifications and Bone, 100
4.3. Conclusions, 106
4.4. References, 109

Chapter 5. **Characterization of Mineralized Tissue using Fourier Transform Infrared Spectroscopy..... 124**

5.0. Introduction, 124
5.1. Materials and Methods, 128
5.1.1. Sample Preparation, 128
5.2. Results and Discussion, 130
5.2.1. General Composition, 130
5.2.2. Mineral Content, 132
5.2.3. Relative Carbonate Content, 134
5.2.4. Degree of Crystallinity and Maturity, 135
5.2.5. Carbonate Substitution, 136
5.2.6. Details of the Mineral Phase, 137
5.2.7. Limitations of Study, 138
5.3. Conclusions, 139
5.4. References, 140

Chapter 6. **Mineral-Density Distributions in Atherosclerotic Calcifications..... 150**

6.0. Introduction, 150
6.1. Materials and Methods, 152
6.1.1. Sample Preparation, 152
6.1.2. Imaging, 152
6.2. Results and Discussion, 154
6.3. Conclusions, 157

6.4. References, 159

Chapter 7. **Summary and Future Directions 166**

7.0. Summary, 166
7.1. Future Directions, 169
7.1.1. Nanoindentation, 170
7.1.2. Spectroscopy, 172
7.1.3. Micro-Computed Tomography, 173
7.2. Concluding Remarks, 174
7.3. References, 175

Appendix A. **Microdissecting and Embedding Calcifications 178**

USF LIBRARY

Tables

1.1: Estimated number of procedures to treat atherosclerosis annually 16

1.2: Statistics for procedures to treat atherosclerosis 17

4.1: Reduced elastic moduli for various depth-to-rms roughness ratios 113

4.2: Maximum depth data at various depth-to-rms roughness ratios 114

4.3: Reduced elastic moduli for various holding times 115

4.4: Reduced elastic moduli for various loading rates 116

4.5: Properties of atherosclerotic calcifications and bone 117

5.1: Mineral properties of atherosclerotic calcifications and bone 144

5.2: Composition of atherosclerotic calcification as determined by FTIR 145

6.1: Mineral density of atherosclerotic calcifications 161

UCSF LIBRARY

Figures

1.1: Example of a highly calcified plaque 18

1.2: Procedures to treat atherosclerosis 19

2.1: Human cardiovascular system 40

2.2: Anatomy of a normal artery 41

2.3: Atherosclerotic disease progression 42

2.4: Atherosclerotic calcification microstructure 43

2.5: Cortical and trabecular bone 44

2.6: Bone microstructure 45

2.7: Endochondral ossification 46

3.1: Nanoindenter instrumentation 73

3.2: Berkovich tip 74

3.3: Hysitron's Triboindenter transducer 75

3.4: Schematic of the indentation process 76

3.5: Load versus displacement indentation curve 77

3.6: Schematic of the Michelson interferometer 78

3.7: High refractive index crystal used in FTIR-ATR 79

3.8: FTIR interferogram 80

3.9: FTIR spectrum of an atherosclerotic calcification 81

3.10: FTIR spectrum with side lobes 82

3.11: Schematic of the micro-computed tomography system 83

3.12: Computed tomography simple back-projection reconstruction 84

4.1: Viscoelastic behavior captured during nanoindentation 118

4.2: Nanoindentation load function 119

4.3: Magnetic resonance image of a highly calcified carotid plaque 119

4.4: Micro-FTIR two-dimensional image of calcification 120

4.5: Nanoindentation testing patterns 121

4.6: RMS roughness of three microtomed calcifications and one bone 122

4.7: Elastic properties of atherosclerosis calcification and bone 123

5.1: Typical FTIR spectra of bone and atherosclerotic calcification 146

5.2: A close-up of the v_4 phosphate peak 147

5.3: Second derivative of a FTIR spectra 148

5.4: Mineral content versus crystallinity 149

6.1: Degrees of bone mineralization 162

6.2: Sedimentary-like mineral deposition 163

6.3: Concentric-like mineral deposition 164

6.4: Complex growth patterns 165

USF LIBRARY

Chapter 1

Introduction

1.0. Atherosclerosis: An Overview

Cardiovascular diseases occur in over 70 million people in the United States (American Heart Association 2005). Given this prevalence and the expense of surgery, the annual health-care costs for this group of diseases have soared to over $395 billion (American Heart Association 2005). In addition, cardiovascular diseases cause 60% of all deaths, regardless of age, gender, or ethnicity (American Heart Association 2005). Of these deaths, three-fourths are caused by atherosclerotic-related strokes or myocardial infarctions (i.e., heart attacks) (American Heart Association 2005). This makes atherosclerosis the leading cause of death (≈ 45% of deaths) above cancer (≈ 23% of deaths) in the United States (American Heart Association 2005). Atherosclerosis occurs in 50% of people as young as 20 to 29 years old and in 80% of those between 30 to 39 years old (Tejada et al. 1968).

Atherosclerosis is a disease initially characterized by localized thickening of the arterial wall through the accumulation of lipids, macrophages, and smooth muscle cells (Stary 1997). In advanced stages of atherosclerosis, these lesions (also known as plaques) become more heterogeneous and complex as fibrous tissue, lipid pools, calcifications, necrotic tissue, hematoma, and/or thrombosis develop (Stary et al. 1995). These additional components further thicken the arterial wall and disrupt its structure and

UCSF LIBRARY

function (Fuessl et al. 2001; Stary et al. 1995). One example of an advanced, highly calcified plaque is shown in Figure 1.1. In worst-case scenarios, plaques may occlude a vessel or rupture. If the plaque ruptures, a thrombosis may form and perhaps occlude the vessel (Fuster et al. 1992). In either scenario, an occlusion in the coronary, cerebral, or peripheral arteries may cause insufficient blood flow to these areas and could cause, respectively, a heart attack, stroke, or gangrene.

Surgery is the most common treatment for a severe atherosclerotic occlusion (which is defined as greater than 50% stenosis, depending on location of the plaque). There are four common surgical procedures. The two most common techniques are balloon angioplasty and stenting. Both techniques are minimally invasive and mechanically dilate the plaque to restore the lumen diameter. In a balloon angioplasty procedure, a balloon located on the tip of a catheter is usually inserted into the femoral artery and routed to the affected location of the lesion. The balloon is then locally inflated to disrupt the plaque and then deflated and removed (Figure 1.2a). The stenting procedure is similar in that it first uses a balloon to disrupt the plaque and then channels a stent (a metallic or metallic polymer-coated cylindrical mesh) to the location of the plaque (Figure 1.2b). This mesh serves as a permanent scaffolding device. The stent may either be expanded by a balloon or self-expandable. The third most common surgery is invasive and consists of cardiac revascularization (bypass), which involves using a graft that acts as a shunt to bypass the affected area (Figure 1.2c). The final technique, endarterectomy, is also invasive and is mainly performed in the carotid arteries of the neck. It entails making an incision in the affected region of the artery, completely removing the plaque

USF LIBRARY

and a portion of the arterial wall, and suturing the arterial walls back together (Figure 1.2d).

The healthcare industry advocates low risk operations that are minimally invasive and less expensive. Table 1.1 lists the estimated number of operations in 2002, demonstrating the popularity of minimally invasive procedures as opposed to endarterectomy or bypass operations. This popularity may arise because minimally invasive procedures are less expensive and have lower in-hospital death rates (Table 1.2). The mean charges for a coronary artery bypass operation is about $71,000 compared to about $34,000 for coronary angioplasty (Healthcare Cost and Utilization Project 2002). Moreover, a coronary artery bypass surgery has a 2.3% in-hospital death rate as compared to 0.8% for coronary angioplasty (Healthcare Cost and Utilization Project 2002).

USF LIBRARY

Minimally invasive procedures, however, have shortcomings. Histological evidence suggests that balloon dilation causes the disruption and/or stretching of the plaque and/or arterial wall to achieve an increased lumen area (Castaneda-Zuniga et al. 1980; Chin et al. 1984; Waller 1989). This disruption can occur by the tearing of the innermost layer of the artery (intima) and dissection between the plaque and the arterial wall because of the differences in material properties of these structures (Castaneda-Zuniga et al. 1980; Waller 1987). However, tearing may even extend through the media and cause a severe dissection that can lead to hemorrhaging (Waller et al. 1983). The extent or location of dissection is unpredictable. In addition, it is not possible to predict the probability, location, or extent of plaque rupture and/or embolization before, during, or after minimally invasive procedures. Moreover, restenosis (re-narrowing of the arterial

wall) encompassing greater than 50% of the lumen cross-sectional area occurs in 30 to 50% of the coronary arteries that undergo angioplasty and 10 to 30% of those receiving stents (Bhargava et al. 2003). Due to restenosis, patients sometimes require multiple interventions. So, although minimally invasive atherosclerotic procedures may be less expensive and less risky, many of the mechanical aspects of the procedures and the tissue response to the procedures are still not understood adequately.

Finite element models help to predict the mechanical responses to these procedures. However, the models require comprehensive understanding of mechanical properties of the tissues to predict accurately their mechanical response to changes in loading, wall composition, or geometry. Thus, determining their mechanical properties is critical for understanding and predicting plaque dissection and ruptures and for designing and improving endovascular devices to treat atherosclerosis.

Tissue responses to the minimally invasive procedures, mainly those inducing restenosis, must also be addressed. Restenosis after angioplasty is thought to occur because of the elastic recoil of the vessels, neointima formation (i.e., smooth muscle cell proliferation and matrix deposition within the plaque), and thrombosis, while restenosis in stents is mainly due to neointimal proliferation and thrombosis (Bhargava et al. 2003; Waller et al. 1990). In the last three years, drug-eluting stents have emerged as a solution to preventing restenosis. They address some of the mechanical and tissue responses to plaque and artery wall compression. The stent prevents elastic recoil of the plaque and arterial wall after dilation; it holds any flaps (caused by dissection) against the plaque and away from the lumen; and it is coated by a polymeric or non-polymeric material that releases drugs that are antithrombotic, anti-inflammatory, antiproliferative,

immunosuppressive, and/or promote healing (Ellis et al. 2005; Palmaz 2004). However, better understanding of the composition of the constituents of plaque and restenosis lesions and the etiology and pathogenesis of atherosclerosis and restenosis would aid in the development of more effective pharmaceutical treatments and drug-delivery devices that reduce the risk of clinical complications.

1.1. Vulnerable Plaque

Currently patients are not routinely screened for the presence of atherosclerosis although it is known that this life-threatening disease may be asymptomatic (Hurst et al. 1994). Instead, patients are not treated until they present symptoms or experience a clinical event (e.g., acute myocardial infarction, or stroke) (Fisher et al. 1994; Hurst et al. 1994). These events are usually provoked by plaque ruptures or erosion of the plaque's surface (Falk 1991; Fuster et al. 1992). It is therefore important to develop more sensitive and predictive diagnostic techniques to identify a vulnerable plaque (one that is considered likely to rupture or erode) before it causes a clinical event.

Plaque vulnerability was initially thought to be correlated to the extent of stenosis (amount of narrowing), i.e., the greater the stenosis, the more vulnerable the plaque was to rupture. This is not necessarily true. Later angiographic studies revealed that patients with mildly narrowed (less than 50%) arteries still had myocardial infarctions (Ambrose et al. 1988; Little et al. 1988). Agreement exists, however, that four main factors affect plaque vulnerability to rupture: (i) size and composition of the lipid core, (ii) fibrous cap thinning, (iii) collagen degradation caused by inflammation of the fibrous cap, and (iv) regions of higher circumferential tensile stress (Cheng et al. 1993; Falk et al. 1995;

USF LIBRARY

Lendon et al. 1991; Loree et al. 1994; Richardson et al. 1989). More details about vulnerable plaque are provided in Chapter 2.

1.2. Research Focus

Of the constituents of atherosclerotic plaque, calcifications are the central focus of this work. Calcifications are present in about 40% of people between 40 to 49 years old and increase with age to as much as about 80% in individuals between 60 to 69 years old (Aldrich et al. 1979; McGuire et al. 1968). Men seem to have a higher risk of having calcifications than women, especially when below the age of 60 years old (e.g., about 70% for men and 45% for women between 50 to 59 years old (Aldrich et al. 1979; Frink et al. 1970; McGuire et al. 1968).

Although it is agreed that the four factors mentioned in the last section may lead to plaque rupture, there is still debate about other possible rupture mechanisms such as the presence of calcifications within the plaque. It is not clear whether calcifications increase or decrease a plaque's probability of rupture. Finite element models of calcified plaques demonstrate that calcifications bear much of the load during systole (heart ventricular contraction), causing a decrease in tensile stress in adjacent tissues but an increase in shear stresses in the load sharing region that could cause adjacent tissues to tear (Richardson et al. 1989). This is confirmed by postmortem evidence of the tearing of tissue adjacent to calcifications (Richardson et al. 1989).

The importance of the presence of calcification to clinical prognosis is also unclear. Margolis et al.'s investigation showed that of 800 mainly symptomatic cardiac patients with calcifications detected by fluoroscopy, 58% of them had a five-year survival

UCSF LIBRARY

rate versus 87% in those individuals without detectable calcium (Margolis et al. 1980). In contrast, Hudson and Walker's study of 78 asymptomatic cardiac patients found no difference in the five-year survival rate between patients with or without calcifications detectable by fluoroscopy (Hudson et al. 1976). The results from these two studies are questionable since there are methodological problems in both (Wexler et al. 1996). Detrano and colleagues' study of 1461 asymptomatic cardiac patients with a greater than 10% risk of coronary events within eight years (according to Framingham risk algorithm) revealed that calcification detectable within coronary arteries by cinefluoroscopy made patients 2.7 times more likely to have a coronary event within one year (Detrano et al. 1994). This risk was independent of standard risk factors. In addition, an x-ray computed tomography study of 241 older patients also showed that those with calcifications had higher chances of having a myocardial infarction than those without calcifications although the mortality rate was the same (Naito et al. 1990).

There does, however, seem to be a relationship between the presence or absence of calcifications and the degree of obstruction or risk of a clinical event. Electron beam computer tomography studies show that the presence of coronary calcifications in asymptomatic and symptomatic patients confirms the presence of a lesion; the greater the amount of calcification, the greater the chance of having an obstruction (Arad et al. 1996; Mautner et al. 1994) The relevance of this is unclear since, as mentioned before, angiograph studies revealed that patients with mildly narrowed (less than 50% occlusion) coronary arteries still suffer from myocardial infarctions (Ambrose et al. 1988; Little et al. 1988). The absence of calcifications detected in coronary arteries by electron beam computer tomography seems to be a better indicator of the absence of lumen narrowing

USF LIBRARY

(Mautner et al. 1994) or the low risk of a clinical event (Arad et al. 1996; Frink et al. 1970). In addition, individuals with coronary symptoms have higher percentages of calcifications detected by electron beam and ultrafast computer tomography than individuals without coronary symptoms (Agatston et al. 1990; Mautner et al. 1994). Unfortunately, all these studies make casual connections and do not provide evidence that link calcifications directly to ruptures (Doherty et al. 1995).

Although the importance of the presence of calcifications is still unclear, evidence suggests that calcifications affect the functionality of arteries. This is not surprising since the mechanical response of the plaque to loads depends on the boundary conditions, material geometry, and material properties of the constituents within the plaque. In vitro plaque-pressurization studies demonstrate that calcified arterial segments are 2.5 times less distensible than non-calcified plaques (Park et al. 1993). Calcified plaques are also stiffer in compression than non-calcified plaques (Lee et al. 1991; Salunke et al. 2001). In addition, Salunke and Topoleski's work indicated that calcified plaque behaves more elastically than other types of plaque by not exhibiting plastic (permanent) deformation and by showing minimal stress relaxation (time-dependent deformation). In addition, calcifications may affect vascular remodeling by causing constrictive remodeling as opposed to the expansive remodeling—thought to preserve lumen size—that occurs in soft plaque (Fuessl et al. 2001).

Calcifications have also been shown to intervene in minimally invasive treatments. Studies of balloon inflation of calcified atherosclerotic arteries from rabbits demonstrated that calcified plaques are less distensible than arteries with non-calcified plaque (Demer 1991). Because of the difference in mechanical properties between the

USF LIBRARY

stiff calcifications and softer surrounding tissue, balloon expansion in angioplasty causes non-uniform stress distributions that often lead to cracks or tears near calcifications. This is shown by the high incidence of dissection near calcified deposits (Fitzgerald et al. 1992). Histological observations of patients that died between a few hours to two years after angioplasty showed that tears extending into the middle or outer layer of the artery produce double the amount of intimal proliferation during restenosis than those lesions with only intimal dissection (Nobuyoshi et al. 1991).

1.3. Objectives of this Work

Predicting plaque vulnerability, dissection, and restenosis due to the deployment of invasive devices is a very difficult task. It requires more knowledge about tissue and mechanical responses to physiological conditions and interventional techniques and devices. Though atherosclerotic calcifications are only one constituent of plaque, the previous section establishes their possible link to plaque vulnerability and the importance of calcifications for patients' prognosis and the success of minimal invasive procedures. Hence, the objective of this work is to further characterize the mechanical behavior, composition, and physical properties of atherosclerotic calcifications. The elastic mechanical properties were studied using nanoindentation, a micromechanical testing modality that allows the measurement of the stiffness and elastic modulus. The composition of calcifications was analyzed and compared to bone using Fourier transform infrared spectroscopy, which specifically measures the energy absorbed by the different vibrational bonds within chemical functional groups of the calcifications. In addition, nanoindentation was coupled with FTIR to determine structure-property relationships. Finally, the mineral-density distribution of atherosclerotic calcifications

UCSF LIBRARY

was determined using micro-computed tomography (micro-CT), which uses x-ray technology to construct three-dimensional images of the calcifications.

The results obtained from this study are relevant to the future understanding of atherosclerotic development and treatments. The mechanical properties and the structure-property information can be used in finite element models that simulate the effect of blood pressure on atherosclerotic lesions and the use of minimally invasive devices to treat this disease. These models can be used to predict restenosis, plaque vulnerability to rupture, and to decide which minimally invasive device is optimal considering the plaque's composition and geometry. Furthermore, having more knowledge about the composition of atherosclerotic calcifications and the mineral-density distributions provide clues about its development and growth, which is important for the development of new pharmaceutical treatments.

UCSF LIBRARY

1.4. Outline of Thesis

The remainder of this thesis comprises six chapters. Chapter 2 reviews the anatomy of healthy arteries, the development and risk factors of atherosclerosis, the cause of plaque vulnerability, and the composition, structure and development of atherosclerotic calcifications as compared to bone. For many of the experiments, bone was used as a control material. Bone was chosen because it is a well-characterized mineralized tissue that serves as a good reference for comparison to calcified vascular tissue. Chapter 3 briefly presents the background and theory of the three techniques and apparatus used for the experiments. Chapter 4 explores the nanomechanical properties of arterial calcifications using nanoindentation and the composition using Fourier transform

infrared spectroscopy (FTIR). It also describes the structure-property relationship that exists in calcifications. Chapter 5 provides a more detailed study of the composition of arterial calcifications, particularly the mineral phase. Chapter 6 utilizes micro-CT and discusses the mineral-density distribution of arterial calcifications. Finally, Chapter 7 summarizes all the experiments and discusses future directions for this work.

1.5. References

Agatston, A. et al. 1990. Quantification of coronary artery calcium using ultrafast computed tomography. *Journal of the American College of Cardiology* 15(4): 827-832.

Aldrich, R. et al. 1979. Coronary calcifications in the detection of coronary artery disease and comparison with electrocardiographic exercise testing: Results from the National Heart, Lung, and Blood Institutes Type-I coronary intervention study. *Circulation* 59(6): 1113-1124.

Ambrose, J. et al. 1988. Angiographic progression of coronary artery disease and the development of myocardial infarction. *Journal of the American College of Cardiology* 12(1): 56-62.

American Heart Association. 2005. Heart Disease and Stroke Statistics: 2005 Update. Report by the American Heart Association, Dallas.

Arad, Y. et al. 1996. Predictive value of electron beam computed tomography of the coronary arteries: 19-month follow-up of 1173 asymptomatic subjects. *Circulation* 93(11): 1951-1953.

Bhargava, B. et al. 2003. New approaches to preventing restenosis. *British Medical Journal* 327(7409): 274-279.

Castaneda-Zuniga, W. et al. 1980. The mechanism of balloon angioplasty. *Radiology* 135(3): 565-571.

Cheng, G. et al. 1993. Distribution of circumferential stress in ruptured and stable atherosclerotic lesions: A structural analysis with histopathological correlation. *Circulation* 87(4): 1179-1187.

Chin, A. et al. 1984. A physical measurement of the mechanisms of transluminal angioplasty. *Surgery* 95(2): 196-201.

Demer, L. 1991. Effect of calcification on in-vivo mechanical response of rabbit arteries to balloon dilation. *Circulation* 83(6): 2083-2093.

Detrano, R. et al. 1994. Prognostic significance of cardiac cinefluoroscopy for coronary calcific deposits in asymptomatic high-risk subjects. *Journal of the American College of Cardiology* 24(2): 354-358.

Doherty, T. and Detrano, R. 1995. Coronary artery calcification. *Radiology* 195(2): 576-577.

Ellis, J. T. et al. 2005. Therapy considerations in drug-eluting stents. *Critical Reviews in Therapeutic Drug Carrier Systems* 22(1): 1-25.

Falk, E. 1991. Coronary thrombosis: Pathogenesis and clinical manifestations. *American Journal of Cardiology* 68(7): B28-B35.

Falk, E.; Shah, P.; and Fuster, V. 1995. Coronary plaque disruption. *Circulation* 92(3): 657-671.

Fisher, M. and Minematsu, K. 1994. Cerebrovascular disorders. *In*: J. Hurst and J. Alpert, eds. *Diagnostic Atlas of the Heart*. New York: Raven Press. pgs. 481-502.

Fitzgerald, P.; Ports, T.; and Yock, P. 1992. Contribution of localized calcium deposits to dissection after angioplasty an observational study using intravascular ultrasound. *Circulation* 86(1): 64-70.

Frink, R. et al. 1970. Significance of calcification of the coronary arteries. *American Journal of Cardiology* 26(3): 241-247.

Fuessl, R. et al. 2001. Vascular remodeling in atherosclerotic coronary arteries is affected by plaque composition. *Coronary Artery Disease* 12(2): 91-97.

Fuster, V. et al. 1992. Mechanisms of disease: The pathogenesis of coronary artery disease and the acute coronary syndromes. *New England Journal of Medicine* 326: 242-50 and 310-18.

Healthcare Cost and Utilization Project. 2002. 2002 National Statistics: Statistics for U.S. hospital stays, principal procedure based on clinical classifications software. Statistics collected by the Healthcare Cost and Utilization Project.

Hudson, N. and Walker, J. 1976. Prognostic significance of coronary artery calcification seen on fluoroscopy. *Clinical Radiology* 27(4): 545-547.

Hurst, J.; Becker, A.; and Alpert, J. 1994. Coronary artery disease. *In*: J. Hurst and J. Alpert, eds. *Diagnostic Atlas of the Heart*. New York: Raven Press. pgs. 83-130.

Lee, R. et al. 1991. Structure-dependent dynamic mechanical behavior of fibrous caps from human atherosclerotic plaques. *Circulation* 83(5): 1764-1770.

Lendon, C. et al. 1991. Atherosclerotic plaque caps are locally weakened when macrophages density is increased. *Atherosclerosis* 87(1): 87-90.

Little, W. et al. 1988. Can coronary angiography predict the site of a subsequent myocardial infarction in patients with mild-to-moderate coronary artery disease? *Circulation* 78(5): 1157-1166.

Loree, H. et al. 1994. Static circumferential tangential modulus of human atherosclerotic tissue. *Journal of Biomechanics* 27(2): 195-204.

Margolis, J. et al. 1980. The diagnostic and prognostic significance of coronary artery calcification: A report of 800 Cases. *Radiology* 137(3): 609-616.

Mautner, S. et al. 1994. Coronary artery disease: Prediction with in-vitro electron-beam CT. *Radiology* 192(3): 625-630.

McGuire, J.; Schneide, H.; and Chou, T. 1968. Clinical significance of coronary artery calcification seen fluoroscopically with image intensifier. *Circulation* 37(1): 82-7.

Naito, S. et al. 1990. Progression to ischemic heart disease in subjects with coronary calcification as evaluated by computed tomography. *Journal of Cardiology* 20(2): 249-58.

Nobuyoshi, M. et al. 1991. Restenosis after percutaneous transluminal coronary angioplasty: Pathological observations in 20 patients. *Journal of the American College of Cardiology* 17(2): 433-439.

Palmaz, J. 2004. Intravascular stents in the last and the next 10 years. *Journal of Endovascular Therapy* 11: 200-206.

Park, J.; Siegel, R.; and Demer, L. 1993. Effect of calcification and formalin fixation on in vitro distensibility of human femoral arteries. *American Heart Journal* 125(2 part 1): 344-349.

Richardson, P.; Davies, M.; and Born, G. 1989. Influence of plaque configuration and stress distribution on fissuring of coronary atherosclerotic plaques. *Lancet* 2(8669): 941-944.

Salunke, N. et al. 2001. Compressive stress-relaxation of human atherosclerotic plaque. *Journal of Biomedical Materials Research* 55(2): 236-241.

Stary, H. 1998. Natural history of atherosclerosis: The sequence of changes in lesion composition. *In*: B. Jacotot, D. Mathe, and J. Fruchart, eds. *Atlas of Atherosclerosis: Progression and Regression.* New York: Elsevier. pgs. 393-472.

Stary, H. et al. 1995. A definition of advanced types of atherosclerotic lesions and a histological classification of atherosclerosis: A report from the committee on vascular lesions of the council on arteriosclerosis, American Heart Association. *Circulation* 92(5): 1355-1374.

Tejada, C. et al. 1968. Distribution of coronary and aortic atherosclerosis by geographic location race and sex. *Laboratory Investigation* 18(5): 509-526.

USF LIBRARY

Waller, B. 1987. Pathology of transluminal balloon angioplasty used in the treatment of coronary heart disease. *Human Pathology* 18(5): 476-84.

Waller, B. 1989. Crackers breakers stretchers drillers scrapers shavers burners welders and melters the future treatment of atherosclerotic coronary artery disease a clinical morphologic assessment. *Journal of the American College of Cardiology* 13(5): 969-987.

Waller, B.; Dillon, J.; and Crowley, M. 1983. Plaque hematoma and coronary dissection with percutaneous transluminal angioplasty (PTCA) of severely stenotic lesions: Morphologic coronary observations in 5 men within 30 days of PTCA. *Circulation* 68(4): 144-144.

Waller, B. et al. 1990. Morphologic observations late after coronary balloon angioplasty mechanisms of acute injury and relationship to restenosis. *Radiology* 174(3 Part 2): 961-968.

Wexler, L. et al. 1996. Coronary artery calcification: Pathophysiology, epidemiology, imaging methods, and clinical implications: A statement for health professionals from the american heart association. *Circulation* 94(5): 1175-1192.

USF LIBRARY

Table 1.1: Estimated number of procedures to treat atherosclerosis annually*

(*Adapted from American Heart Association 2005*)

Type of procedure	Total no. of procedures
Angioplasty	1204
PTCA**	657
Stenting	537
Cardiac Revascularization (Bypass)	515
Endarterectomy	134

*Estimates are in the thousands

**PTCA is the abbreviation for percutaneous coronary artery

USF LIBRARY

Table 1.2: Statistics for procedures to treat atherosclerosis
(*Adapted from Healthcare Cost and Utilization Project 2002*)

Type of procedure	Mean charges per procedure ($)	National bill ($ billions)	Mean length of stay (days)	% of in-hospital deaths
PTCA*	34,075	23.6	2.8	0.8
CABG**	70,618	22.4	8.8	2.3
Endarterectomy***	19,348	2.7	2.8	0.5

*PTCA is the abbreviation for percutaneous coronary artery
**CABG is the abbreviation for coronary artery bypass graft
***Performed on vessels of the head and neck

USF LIBRARY

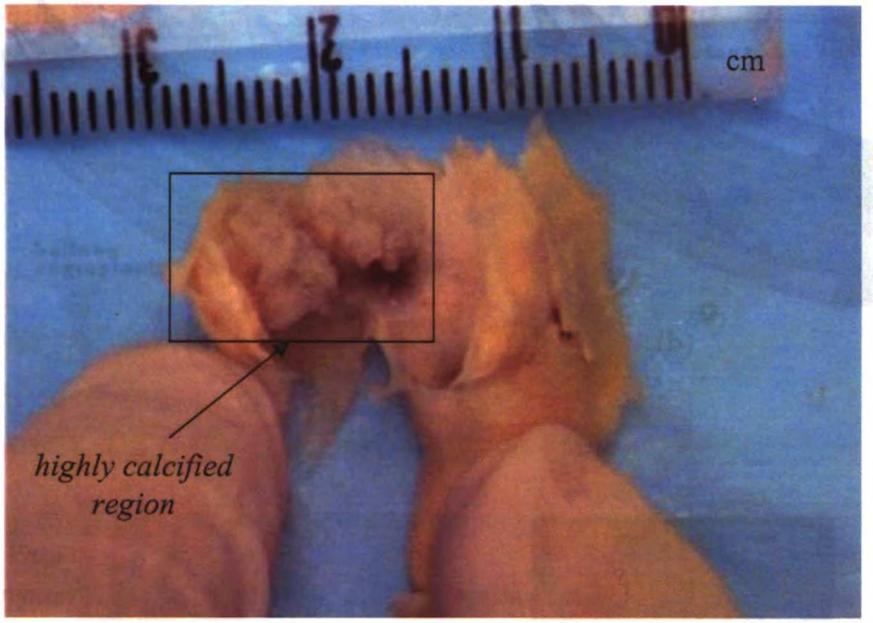

Figure 1.1: Example of a highly calcified plaque

USF LIBRARY

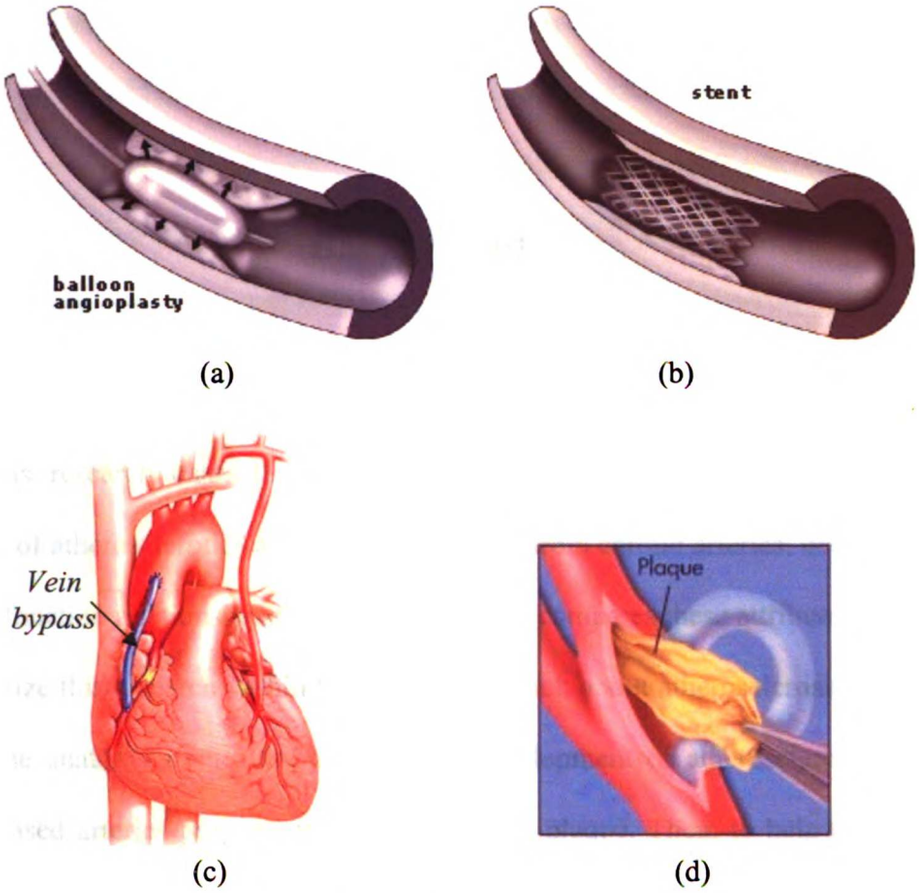

Figure 1.2: Procedures to treat atherosclerosis
Illustration depicting four procedures to treat atherosclerosis: (a) balloon angioplasty* (b) Stenting* (c) coronary artery bypass^ (d) endarterectomy†
Adapted from:
* *Cleveland Clinic*
(www.cchs.net/health/health-info/docs/0200/0234.asp?index=4810)
^ *Mayo Clinic*
(www.mayoclinic.org/coronaryartery-jax/)
† *CorVasc*
(www.corvascmds.com/vascular_surgery_procedures_endarterectomy.htm)

USF LIBRARY

Chapter 2

Background

2.0. Introduction

This research characterizes the nanomechanical, compositional, and physical properties of atherosclerotic calcifications obtained from carotid arteries; determines their structure-function relationships; and, in some cases, compares these attributes to bone. To contextualize this research within the broader research about atherosclerosis, this section reviews the anatomy of healthy arteries, the development of atherosclerosis, and how these diseased arteries progress to form vulnerable plaque. Then, to help to delimit the scope of this research, it reviews the current knowledge about the composition, structure, development, and growth of atherosclerotic calcifications and bone.

UCSF LIBRARY

2.1. Anatomy of Normal Arteries

The anatomy of normal arteries mainly comprises arteries, arterioles, capillaries, venules, and veins. Arteries and arterioles carry blood away from the heart; the capillaries exchange nutrients, gases, and waste in tissues; and the veins and venules return the blood to the heart. The arterioles and venules are thinner and have smaller diameters than arteries and veins.

In this research, atherosclerotic calcifications were obtained from human carotid arteries, the two main arteries in the neck that supply blood to the brain (Figure 2.1). Like

other arteries, the carotid arteries have three main concentric layers: the innermost layer, in contact with the blood, is the *intima;* the middle layer is the *media;* and the outer layer, the *adventitia* (Figure 2.2). The intima mainly consists of a single layer of flat, elongated endothelial cells and some proteoglycans,[1] all of which lie on a basal elastic lamina; the media comprises smooth muscle cells (SMCs), elastin,[2] collagen,[3] and proteoglycans; and the adventitia comprises mainly collagen fibers but also has fibroblasts and associated proteoglycans (Bader 1963).

2.2. Atherosclerosis

2.2.1. Development of Atherosclerosis

Atherosclerosis is the leading cause of deaths in the United States, effecting over 50 million individuals and resulting in more than half a million deaths each year (American Heart Association 2002). Although the pathogenesis of this disease is unknown, scientists recognize that it begins in the intimal layer of an artery. The most accepted hypothesis, which began as early as 1856 and has continuously been modified as more evidence emerged, assumes that atherosclerosis begins as a response to injury (Virchow 1856). The intimal endothelial cells are injured either physically (e.g., by the shear force of blood, especially at branches and bifurcations) or chemically (e.g., by toxins released by cigarettes while smoking or because of hypercholesterolemia) (Ip et al.

[1] Proteoglycans comprise a core protein molecule with attached glycoaminoglycans (i.e., acidic mucopolysaccharides).

[2] An elastin fiber has two components: (1) elastic microfibrils comprising mainly glycoprotein and (2) an amorphous elastin component that surrounds the micofibrils (Burke et al. 1979).

[3] Collagen is another type of fiber made of a triple helix of three polypeptide chains, called alpha chains (Burke et al. 1979). The main collagens found in arteries are types I and III. These two differ in the type of alpha chains (i.e., each has a unique sequence of amino acids). Type I lesions are also common in bone, tendon, skin and the uterus, while type III is common in the uterus and fetal skin (Burke et al. 1979).

UCSF LIBRARY

1990; Ross 1999). Since the source of injury is usually chronic, the continuous damage does not allow healing and, therefore, the disease progresses.

The injury triggers an inflammatory response in which monocytes, T-lymphocytes, and glycoproteins are beckoned to the injured site. The glycoproteins adhere to the injured surface. The monocytes and T-lymphocytes attach to the glycoproteins and migrate between the intimal endothelial cells into the subintimal surface (Nilsson 1986; Rosenfeld et al. 1987). The injured intima also allows low-density lipoproteins into the subenthothelial layer, where the low-density lipoproteins become oxidized (Mora et al. 1987). The T-lymphocytes and monocytes in the intima are then triggered to differentiate into macrophages and ingest the oxidized low-density lipoproteins (Masuda et al. 1990; Munro et al. 1988).

The preceding events are only the initial stages of atherosclerosis. Among several schemes used to categorize the progression of atherosclerosis, the Stary histological classification system is the most widely used, having been endorsed by the American Heart Associated (Stary et al. 1995). According to Stary's atherosclerosis classifications, there are six main types of lesions (Figure 2.3) (Stary et al. 1995; Stary et al. 1994). The clustering of macrophages, low-density lipoproteins, and macrophages-containing lipids (foam cells) constitute a type I lesion and has been observed even in eight-month-old babies (Stary 1998). Type II lesions form as more foam cells accumulate in the intima in stratified layers. Type I and II lesions are also known as fatty streaks (Ross 1995). In an intermediate lesion (type III), the preatheroma, small pools of extracellular lipid droplets begin to form. In these three types of lesions, there is little to no increase in wall thickness and minimal to no reduction in lumen diameter.

IUPUI LIBRARY

In advanced stages of the disease, type IV though VI lesions form. An atheroma, a type IV lesion, forms by the growth and fusion of small lipid pools into a lipid core. This lesion starts the wall thickening process and may reduce the lumen diameter, depending on whether there is compensatory enlargement of the circumference of the artery wall.[4] This type of lesion may progress directly into any of the other advanced lesions, types V through VI.

In a type Va lesion, the phenotype of medial smooth muscle cells is transformed from a contractile to a proliferative state (Campbell et al. 1985; Mosse et al. 1985). This has been observed by the increase in synthetic organelles in the smooth muscle cells of human plaque from carotid arteries, and, in primary cultures from adult rats, by the loss of myofilaments and contractility and an increase in organelles (Mosse et al. 1985; Sjolund et al. 1986; Thyberg et al. 1983). These transformed, smooth muscle cells are then triggered to migrate into the intima, proliferate, and produce and secrete extracellular matrix such as collagen (collagen I, III, and V) and elastin (Campbell et al. 1985; Mosse et al. 1985; Sjolund et al. 1986). This extracellular matrix forms into a fibrous tissue, hence the lesion's name: fibroatheroma. The fibrous tissue may encapsulate the lesion, forming a fibrous cap that separates the lesion from the blood flow. The accrual of fibrous tissue in this type of lesion may reduce further the lumen diameter.

A type Va lesion may progress directly into any of the more advanced lesions (types Vb, Vc, VI). Type Vb and Vc lesions occur in individuals of about 50 years or

UCSF LIBRARY

[4] Compensatory enlargement is the increase in the circumference of the artery as a response to intimal thickening (Clarkson et al. 1994).

older (Stary 1998). Type Vb lesions comprise mainly lipid and necrotic regions that have been mostly or fully calcified. These lesions are, therefore, almost entirely calcified and are classified as calcified plaque. Small-calcified particulates have been found as early as the second decade of life (Stary 1998).

The other type V class of advanced plaque is a type Vc, fibrotic lesion. This lesion predominately comprises collagen and little to no lipid. It may result from the reabsorption of lipids, aggregation of more fibrous tissue, or a thrombosis that became fibrous tissue (Stary 1998).

The last class of lesions (Type VI) appears as early as the fourth decade of life. In the sub-surface, they may appear as either type IV or any of the type V lesions; however, on the surface, they may have an ulcerated fibrous cap with or without thrombotic and/or hematoma deposits (Stary 1998). Thrombotic layers may build upon each other or may become fibrous tissue, further decreasing the lumen and potentially leading to complete arterial occlusion (Stary et al. 1995).

USF LIBRARY

2.2.2. Plaque Vulnerability

Although Stary's classification scheme provides a means of categorizing plaques by their composition, it does not help clinicians predict which plaques are most vulnerable to rupture or erosion. The danger of rupture or erosion of a fibrous cap is that such an event exposes the underlying lipids within the plaque to blood, inducing a thrombus to form (Davies et al. 1985; Falk 1991). Erosion of the fibrous cap of predominately proteoglycan- or smooth muscle-cell-rich plaques (without lipid cores) has also been found to cause the formation of a thrombus (Farb et al. 1996). Thrombosis, in

turn, may decrease or even occlude the lumen, obstructing blood flow and causing a clinical event (e.g., unstable angina, acute myocardial infarction, or sudden death) (Davies et al. 1985; Forrester et al. 1987).

Research has revealed that four main factors that affect a plaque's vulnerability to rupture: (i) size and composition of the lipid core, (ii) regions of higher circumferential tensile stress, (iii) fibrous cap thinning, and (iv) collagen degradation caused by inflammation of the fibrous cap. Aortic plaques with large lipid pools (i.e., greater than or equal to 40% of the cross-section of the plaque by area) and those containing liquid cholesterol esters rather than crystalline cholesterol are especially prone to plaque rupture (Davies et al. 1993; Loree et al. 1994b; Small 1988). A finite element study was conducted on the geometry of 12 ruptured and 12 stable atherosclerotic plaques to calculate the regions of high stresses and correlate these regions with histological cross-sections (Cheng et al. 1993). The result of that study suggests that the areas experiencing high circumferential tensile stresses are more susceptible to rupture (Cheng et al. 1993). Another finite element study also showed that soft lipid pools cannot bear the circumferential stress imposed by the blood flow and, hence, high stresses concentrate in the fibrous cap, making the fibrous cap of plaques dominated by lipid pools more prone to rupture (Loree et al. 1994a; Richardson et al. 1989). Another finite element study found that the thinning of the fibrous caps also increases peak circumferential stress at the fibrous cap again making the cap vulnerable to rupture (Loree et al. 1992). Moreover, finite element models found that areas of high circumferential tensile stress are associated with areas of collagen degradation (Lee et al. 1996). Fibrous plaque with higher levels of macrophages than smooth muscle cells also seem prone to rupture and thrombosis

UCSF LIBRARY

purportedly because macrophages produce collagen-degrading enzymes that weaken collagen and mechanically weaken fibrous caps (Davies et al. 1993; Lendon et al. 1991).

2.3. Arterial Calcifications and Bone

The following sections review arterial calcifications' function, composition, structure, and biomineralization process and compare them to those in other calcified tissues, such as bone, that have been studied more comprehensively and, for that reason, will be used as a comparative baseline.

2.3.1. Function of Arterial Calcifications and Bone

The function of atherosclerotic calcifications is unclear. Some believe calcifications stabilize a plaque since large calcifications can bear most of the circumferential stresses and, thus, reduce the stresses within the fibrous cap (Lee 2000; Richardson et al. 1989). In reality, this does not happen until the calcification grows large enough to bear the load. On the other hand, calcifications may make plaques more vulnerable to rupture since they also increase shear stresses that can tear adjacent tissues (Richardson et al. 1989).

In contrast to the knowledge of atherosclerotic calcifications, the functions of bone are well understood. Bones are not only the load-bearing support for the body but also provide mobility, protect some of the most important organs of the body, and act as the primary calcium reserve.

UCSF LIBRARY

2.3.2. Composition of Arterial Calcifications and Bone

Like other calcified tissues such as bone, atherosclerotic calcifications are mainly composed of mineral and matrix. A study of grades[5] III and IV of atherosclerotic thoracic and abdominal aortic calcifications revealed that the calcifications are predominantly made up of about 78% carbonate-containing analog of hydroxyapatite and 15% protein by dry weight (Schmid et al. 1980). Bone, on the other hand, mainly comprises 70% to 75% carbonate-containing analog of hydroxyapatite and 24% protein by dry weight (Gong et al. 1964; Herring 1977).

The hydroxyapatite, $Ca_{10}(PO_4)_6(OH)_2$, of both of these minerals is poorly crystallized because it contains impurities such as magnesium in place of calcium ions and substitutes such as carbonate for phosphate or hydroxyl anions (Rey et al. 1991a; Schmid et al. 1980). In addition, bone is known to have other impurities such as sodium and potassium in place of calcium ions and other substitutes such as acidic-phosphate for phosphate anions, and chloride and fluoride for hydroxyl anions (Rey et al. 1990).

The organic matrix of calcifications is made up of collagen (collagen I, III, and V) and elastin (Campbell et al. 1985; Mosse et al. 1985; Sjolund et al. 1986). Unfortunately, no studies have rigorously documented the percent of the composition. In contrast, bone is made up of 80-95% type I collagen. The remainder consists of other types of collagen and noncollagenous proteins such as osteocalcin and osteopontin (Aubin et al. 2002).

USF LIBRARY

[5] The grades were assigned according to the International Atherosclerotic Project (McGill 1968). Grade III refers to lesions in which 30% to 60% of the intimal surface is covered by fibrous plaque and grade IV refers to lesions in which 65% to 90% of the intimal surface is mainly covered by complicated fibrous plaque containing ulcerations, thrombosis, or necrosis with or without calcification.

2.3.3. Structure of Arterial Calcifications and Bone

The structure of atherosclerotic calcifications varies greatly. Moreover, unlike other calcified tissues such as bone, their growth is poorly understood. Information about the growth of atherosclerotic calcifications mainly consists of observations made at different stages of growth. Since the structure does not have a clear and consistent growth pattern, it is difficult to assess its structural development.

The growth of atherosclerotic calcifications is as follows, beginning from the ultrastructure to the macrostructure. A study, of the ultrastructure of arterial calcifications in rabbits, revealed microgranular spherular deposits as small as 110 ± 20 Å in diameter (Yu 1974). In addition, calcifications exist in the form of microcrystals that are needle-like, polyhedrals, or microspherulites (Yu 1974). At a microscale, calcified deposits occur as smooth spheres (0.05-2.5 μm diameter), spherulites (5-6 μm diameter), fibrils (0.05-0.1 μm diameter), flat plates (0.5 μm), and irregularly shaped (1-2.5 μm) (Schmid et al. 1980) (Figure 2.4). The spheres occur individually and as conglomerates (Schmid et al. 1980). The fibrils have been found in fibril "bundles, sheets, and three-dimensional networks" (Schmid et al. 1980). Irregular shaped calcifications have been found to be connected to fibrils while the flat plates do not appear to be (Schmid et al. 1980). At a macrostructural level, calcifications occur as larger granules, layered sheets, or amorphous solid deposits. These large structures sometimes take up the entire area of the lumen. The existence of multilayered arterial calcification and the incremental sizes of spherical calcifications suggests that arterial calcifications may build on top of each other, requiring the presence of a structural base or core (Bobryshev et al. 1995; Daoud et al. 1985).

UCSF LIBRARY

In contrast to the variability of the structure of atherosclerotic calcifications, bone is highly structured. Bone has two main types: cortical and trabecular (Figure 2.5). The basic building block of both of these types of bone is mineralized collagen fibrils (20-40 μm diameter) arranged into densely stacked thin sheets called lamellae (about 7 μm thick). In cortical bone, the lamallae are arranged concentrically around a Haversian canal,[6] forming what is known as an osteon (about 200 μm diameter) (Figure 2.6). Different osteons are also densely packed and run parallel to each other.

In trabecular bone, the collagen fibrils are arranged unidirectionally into lamellae 'packets' (100 μm length). Multiple lamellae 'packets' form trabeculae shaped like rods or plates (50-450 μm thick) (Gibson 1985). Since the trabeculae are organized into a highly porous cellular solid (Figure 2.5), trabecular bone is lighter than cortical bone. Curiously, bone-like structures (trabeculae and marrow-like regions) sometimes appear within atherosclerotic calcifications (Bostrom et al. 1995; Demer et al. 1994; Jeziorska et al. 1998b). This may happen because certain proteins commonly found in the bone mineralization process also occur in calcified plaque as explained in the next section (Bostrom et al. 1993; Gadeau et al. 2001; Gijsbers et al. 1990).

At a macroscale, bones may be categorized as short, long, or flat. Short bones (e.g., wrist, ankle, center of the vertebrae) have approximately the same dimension in every direction. They usually have a thin outer cortical shell filled with marrow and trabecular bone. Long bones (e.g., femur, humerous) are longer in one direction. This type of bone has a thick cortical shell, the mid-shaft is filled with marrow while each end is filled with trabecular bone and marrow. Lastly, flat bones (e.g., skull, pelvis) have one

[6] A Harversian canal is a channel that contains blood vessels, nerves, and various blood cells.

UCSF LIBRARY

dimension that is much smaller than the others. These bones have a thin cortical shell filled with marrow and trabecular bone.

2.3.4. Biomineralization of Arterial Calcifications and Bone

The formation of arterial calcifications was initially thought to be a passive process, occurring by calcium apatite precipitation onto or between degenerated-regenerated elastin or onto compounds associated with elastin (Martin et al. 1963; Urry 1974; Yu et al. 1963). The initial precipitate would attract more calcium apatite, leading to calcium apatite accumulation and growth (Yu 1974). Recent research, however, provides evidence that the development of arterial calcification is actually an active process regulated by proteins that are also found during bone mineralization (Bostrom et al. 1993; Gadeau et al. 2001). To better explain what is known about the biomineralization of atherosclerotic calcifications, one must understand the development and growth of bone since there are some similarities between the two types calcified tissue.

USF LIBRARY

Load-bearing bones (like the vertebral bone used in this study) form by endochondral ossification. In brief, bone formation occurs as follows. Mesenchymal cells are differentiated in chondrocytes, which then proliferate producing a very dense mass of cells. The chondrocytes then secrete a loose extracellular matrix (ECM). With continued secretion, the ECM becomes denser and the chondrocytes begin to grow (hypertrophy) and secrete alkaline phosphatase, an enzyme essential for mineral deposition. In addition, the matrix calcifies. The chondrocytes degrade leaving cavities that may be filled by osteoblasts (i.e., bone building cells). The osteoblasts use the calcified matrix as a

scaffold to deposit osteoid (i.e., a bone matrix), which then mineralizes, thus forming the final bone tissue. Areas where osteoblasts do *not* fill the cavity become trabecular bone while the more solid mineralized regions become cortical bone. In addition, the osteoclasts (i.e., bone reabsorptive cells) reabsorb the center of the shaft, thus forming the marrow cavity.

In long bone, this process begins in the middle of what will become the long bone and occurs in very distinct columns. Because of the columnar growth, the center solidifies and the growth is extended away from the center. Long bones have four very distinct regions from the center outward (from most to least mineralized): the central calcified region; the hypertrophied region; the proliferating region; and the resting region in which no proliferation occurs (Figure 2.7).

LIBRARY

Unlike the well-characterized biomineralization of bone, the entire biomineralization of atherosclerotic calcifications is not completely understood though studies point to two types of processes: a cellular and an acellular process. Cellular biomineralization is believed to occur within matrix vesicles (sometimes referred to as microvascular 'pericyte-like' cells), which form by (i) pinching off the cells of arterial walls or (ii) develop from the debris of dead foam cells or smooth muscle cells (Morgan 1980; Stary 1990; Tanimura et al. 1986a; Tanimura et al. 1986b). The hypothesis (i) is analogous to the development of bone in which matrix vesicles form by pinching off chondrocytes (Anderson 1989). Regardless of the mode of formation, evidence of the existence of these matrix vesicles has been confirmed by scanning electron microscopy and energy dispersive x-ray studies that found calcium deposits within such matrix

vesicles (Daoud et al. 1985; Kim 1976). Consequently, these vesicles may provide the microenvironment needed for biomineralization (Jeziorska et al. 1998a).

Evidence suggests that, as with bone matrix vesicles, arterial matrix vesicles contain phosphatase and calcium binding phospholipids (Frink et al. 1970; Tanimura et al. 1986a). Both phosphatase and phospholipids have been shown to bind to calcium phosphate (Vogel et al. 1976; Wuthier et al. 1975). In addition, proteolipids from the atherosclerotic plaque seem to induce calcium crystallization (Daoud et al. 1985). This implies that several mechanisms may exist to transport calcium into the matrix vesicles.

The acellular development of calcification seems to require a structural base for nucleation and development. This is apparent because calcifications in atherosclerotic plaque have been found to develop on degenerated or regenerated elastic fibers, unesterfied cholesterol, or collagen (Bobryshev et al. 1995; Tanimura et al. 1986b; Yu 1974).

As stated earlier, evidence suggests that the biomineralization of atherosclerotic calcification may actually be an active process regulated by proteins that also occur during bone formation. Certain proteins that usually appear during the mineralization of bones have also been found in calcified plaque such as osteopontin, osteocalcin, Gla-containing protein, and bone morphonegetic protein 2a (BMP-2a) (Bostrom et al. 1993; Gadeau et al. 2001; Gijsbers et al. 1990). The role of osteopontin is not understood since it can stimulate or inhibit the formation of calcium crystals, depending on the concentration of osteopontin and whether mineralization has begun (Fitzpatrick et al. 1994). Although osteocalcin has a strong affinity for hydroxyapatite, it can delay calcium nucleation (Hunter et al. 1996). This is further validated since osteocalcin can inhibit

UCSF LIBRARY

bone formation without affecting mineralization (Ducy et al. 1996). These findings may explain why osteopontin and osteocalcin were not found in the injured arterial walls of rabbits during the nucleation of calcifications but only after the calcifications had formed (Gadeau et al. 2001). Although these two proteins may be inhibitory, other proteins (such as Gla-containing protein and BMP-2a) that stimulate calcium formation have been found in plaque and the arterial wall (Bostrom et al. 1993; Gijsbers et al. 1990). Gla-containing protein is a calcium-binding protein and BMP-2a assists in the differentiation of cells into osteoblasts (i.e., cells that build bone) (Fitzpatrick et al. 1994).

UCSF LIBRARY

2.4. Summary

This chapter reviewed the anatomy of healthy arteries, the possible six stages in the development of atherosclerosis, and how these diseased arteries progress to form vulnerable plaque, thus enabling the reader to understand how the present study relates to atherosclerosis. Although the function, composition, structure, and biomineralization of bone is well understood, the previous sections indicate how little is known about atherosclerotic calcifications. Hence, it is important to conduct further research about atherosclerotic calcifications as this present study is intended to do. Toward that end, the present research focuses on characterizing the compositional and physical properties of arterial calcifications.

2.5. References

American Heart Association. 2002. 2002 Heart and Stroke Statistical Update. Report by the American Heart Association, Dallas.

Anderson, H. 1989. Biology of disease: Mechanism of mineral formation in bone. *Laboratory Investigation* 60(3): 320-330.

Aubin, J. and Triffitt, J. 2002. Mesenchymal stem cells and osteoblast differentiation. *In*: J. Bilezikian, L. Raisz, and G. Rodan, eds. *Principles of bone biology*. San Diego: Academic Press. pgs. 59-82.

Bader, H. 1963. The anatomy and physiology of the vascular wall. *In*: W. Hamilton and P. Dow, eds. *Handbook of physiology: Circulation*. Washington D.C.: American Physiology Society. pgs. 856-889.

Bobryshev, Y. V.; Lord, R. S.; and Warren, B. A. 1995. Calcified deposit formation in intimal thickenings of the human aorta. *Atherosclerosis* 118(1): 9-21.

Bostrom, K. et al. 1993. Bone morphogenetic protein expression in human atherosclerotic lesions. *Journal of Clinical Investigation* 91(4): 1800-1809.

Bostrom, K. et al. 1995. Atherosclerotic calcification: Relation to developmental osteogenesis. *American Journal of Cardiology* 75(6): B88-B91.

Burke, J. M. and Ross, R. 1979. Synthesis of connective tissue macromolecules by smooth muscle. *International Review of Connective Tissue Research* 8: 119-157.

Campbell, G. R. and Campbell, J. H. 1985. Recent advances in molecular pathology: Smooth muscle phenotypic changes in arterial wall homeostasis: Implications for the pathogenesis of atherosclerosis. *Experimental and Molecular Pathology* 42(2): 139-162.

Cheng, G. C. et al. 1993. Distribution of circumferential stress in ruptured and stable atherosclerotic lesions: A structural analysis with histopathological correlation. *Circulation* 87(4): 1179-1187.

Clarkson, T. B. et al. 1994. Remodeling of coronary arteries in human and nonhuman primates. *Journal of the American Medical Association* 271(4): 289-294.

Daoud, A. S. et al. 1985. Ultrastructural and elemental analysis of calcification of advanced swine aortic atherosclerosis. *Experimental and Molecular Pathology* 43(3): 337-347.

UCSF LIBRARY

Davies, M. et al. 1993. Risk of thrombosis in human atherosclerotic plaques: Role of extracellular lipid, macrophage, and smooth muscle cell content. *British Heart Journal* 69(5): 377-381.

Davies, M. and Thomas, A. 1985. Plaque fissuring: The cause of acute myocardial infarction, sudden ischemic death, and crescendo angina. *British Heart Journal* 53(4): 363-373.

Demer, L.; Watson, K.; and Bostrom, K. 1994. Mechanism of calcification in atherosclerosis. *Trends in Cardiovascular Medicine* 4(1): 45-49.

Ducy, P. et al. 1996. Increased bone formation in osteocalcin-deficient mice without bone resorption defect. *Journal of Bone and Mineral Research* 11: 43-43.

Falk, E. 1991. Coronary thrombosis: Pathogenesis and clinical manifestations. *American Journal of Cardiology* 68(7): B28-B35.

Farb, A. et al. 1996. Coronary plaque erosion without rupture into a lipid core: A frequent cause of coronary thrombosis in sudden coronary death. *Circulation* 93(7): 1354-1363.

Fitzpatrick, L. et al. 1994. Diffuse calcification in human coronary arteries: Association of osteopontin with atherosclerosis. *Journal of Clinical Investigation* 94(4): 1597-1604.

Forrester, J. S. et al. 1987. A perspective of coronary disease seen through the arteries of living man. *Circulation* 75(3): 505-513.

Frink, R. J. et al. 1970. Significance of calcification of the coronary arteries. *American Journal of Cardiology* 26(3): 241-247.

Gadeau, A. et al. 2001. Time course of osteopontin, osteocalcin, and osteonectin accumulation and calcification after acute vessel wall injury. *Journal of Histochemistry & Cytochemistry* 49(1): 79-86.

Gibson, L. 1985. The mechanical behavior of cancellous bone. *Journal of Biomechanics* 18(5): 317-328.

Gijsbers, B. et al. 1990. Characterization of a Gla-containing protein from calcified human atherosclerotic plaques. *Arteriosclerosis* 10(6): 991-995.

Gong, J. K.; Cohn, S. H.; and Arnold, J. S. 1964. The density of organic and volatile and non-volatile inorganic components of cone. *Anatomical Record* 149(3): 319-324.

Herring, G. M. 1977. Methods for study of glycoproteins and proteoglycans of bone using bacterial collagenase: Determination of bone sialoprotein and chondroitin sulfate. *Calcified Tissue Research* 24(1): 29-36.

Hunter, G. et al. 1996. Nucleation and inhibition of hydroxyapatite formation by mineralized tissue proteins. *Biochemical Journal* 317: 59-64.

Ip, J. et al. 1990. Syndromes of accelerated atherosclerosis: Role of vascular injury and smooth muscle cell proliferation. *Journal of the American College of Cardiology* 15(7): 1667-1687.

Jeziorska, M.; McCollum, C.; and Woolley, D. 1998a. Calcification in atherosclerotic plaque of human carotid arteries: Associations with mast cells and macrophages. *Journal of Pathology* 185(1): 10-17.

Jeziorska, M.; McCollum, C.; and Woolley, D. 1998b. Observations on bone formation and remodelling in advanced atherosclerotic lesions of human carotid arteries. *Virchows Archives* 433(6): 559-565.

Kim, K. 1976. Calcification of matrix vesicles in human aortic valve and aortic media. *Federation Proceedings* 35(2): 156-162.

Lee, R. 2000. Atherosclerotic lesion mechanics versus biology. *Zeitschrift Fur Kardiologie* 89: 80-84.

Lee, R. et al. 1996. Circumferential stress and matrix metalloproteinase I in human coronary atherosclerosis: Implications for plaque rupture. *Arteriosclerosis Thrombosis and Vascular Biology* 16(8): 1070-1073.

Lendon, C. et al. 1991. Atherosclerotic plaque caps are locally weakened when macrophages density is increased. *Atherosclerosis* 87(1): 87-90.

Loree, H. et al. 1992. Effects of fibrous cap thickness on peak circumferential stress in model atherosclerotic vessels. *Circulation Research* 71(4): 850-858.

Loree, H. et al. 1994a. Static circumferential tangential modulus of human atherosclerotic tissue. *Journal of Biomechanics* 27(2): 195-204.

Loree, H. et al. 1994b. Mechanical properties of model atherosclerotic lesion lipid pools. *Arteriosclerosis and Thrombosis* 14(2): 230-234.

Martin, G. R. et al. 1963. Chemical and morphological studies on in vitro calcification of aorta. *Journal of Cell Biology* 16(2): 243-251.

Masuda, J. and Ross, R. 1990. Atherogenesis during low-level hypercholesterolemia in the nonhuman primate, I: Fatty streak formation. *Arteriosclerosis* 10(2): 164-177.

UCSF LIBRARY

McGill, H. C. 1968. Introduction to geographic pathology of atherosclerosis. *Laboratory Investigation* 18(5): 465.

Mora, R.; Lupu, F.; and Simionescu, N. 1987. Prelesional events in atherogenesis: Colocalization of apolipoprotein-B, unesterified cholesterol and extracellular phospholipid liposomes in the aorta of hyperlipidemic rabbit. *Atherosclerosis* 67(2-3): 143-154.

Morgan, A. 1980. Mineralized deposits in the thoracic aorta of aged rats: Ultrastructural and electron-probe X-ray microanalysis study. *Experimental Gerontology* 15(6): 563-573.

Mosse, P. et al. 1985. Smooth muscle phenotypic expression in human carotid arteries, I: Comparison of cells from diffuse intimal thickenings adjacent to atheromatous plaques with those of the media. *Laboratory Investigation* 53(5): 556-562.

Munro, J. M. and Cotran, R. S. 1988. The pathogenesis of atherosclerosis: Atherogenesis and inflammation. *Laboratory Investigation* 58(3): 249-261.

Nilsson, J. 1986. Growth-factors and the pathogenesis of atherosclerosis. *Atherosclerosis* 62(3): 185-199.

Rey, C. et al. 1990. Resolution-enhanced Fourier transform IR spectroscopy study of the environment of phosphate ions in the early deposits of a solid phase of calcium phosphate in bone and enamel and their evolution with age, I: Investigations in the ν_4 phosphate domain. *Calcified Tissue International* 46(6): 384-394.

Rey, C. et al. 1991. Fourier transform infrared spectroscopic study of the carbonate ions in bone mineral during aging. *Calcified Tissue International* 49(4): 251-258.

Richardson, P.; Davies, M.; and Born, G. 1989. Influence of plaque configuration and stress distribution on fissuring of coronary atherosclerotic plaques. *Lancet* 2(8669): 941-944.

Rosenfeld, M. E. et al. 1987. Fatty streak initiation in Watanabe heritable hyperlipemic and comparably hypercholesterolemic fat-fed rabbits. *Arteriosclerosis* 7(1): 9-23.

Ross, R. 1995. Cell biology of atherosclerosis. *Annual Review of Physiology* 57: 791-804.

Ross, R. 1999. Mechanisms of disease - Atherosclerosis - An inflammatory disease. *New England Journal of Medicine* 340(2): 115-126.

Schmid, K. et al. 1980. Chemical and physicochemical studies on the mineral deposits of the human atherosclerotic aorta. *Atherosclerosis* 37(2): 199-210.

UCSF LIBRARY

Sjolund, M. et al. 1986. Phenotype modulation in primary cultures of smooth muscle cells from rat aorta: Synthesis of collagen and elastin. *Differentiation* 32(2): 173-180.

Small, D. M. 1988. Duff, George, Lyman Memorial Lecture - Progression and regression of atherosclerotic lesions: Insights from lipid physical biochemistry. *Arteriosclerosis* 8(2): 103-129.

Stary, H. 1990. The sequence of cell and matrix changes in atherosclerotic lesions of coronary arteries in the first 40 years of life. *European Heart Journal* 11: 3-19.

Stary, H. 1998. Natural history of atherosclerosis: The sequence of changes in lesion composition. *In*: B. Jacotot; D. Mathe; and J. Fruchart, eds. *Atlas of Atherosclerosis: Progression and Regression.* New York: Elsevier. pgs. 393-472.

Stary, H. et al. 1994. A definition of initial, fatty streak, and intermediate lesions of atherosclerosis: A report from the committee on vascular lesions of the Council on Arteriosclerosis, American Heart Association. *Arteriosclerosis and Thrombosis* 14(5): 840-856.

Stary, H. et al. 1995. A definition of advanced types of atherosclerotic lesions and a histological classification of atherosclerosis: A report from the committee on vascular lesions of the council on arteriosclerosis, American Heart Association. *Circulation* 92(5): 1355-1374.

Tanimura, A.; McGregor, D.; and Anderson, C. 1986a. Calcification in atherosclerosis, I: Human studies. *Journal of Experimental Pathology* 2(4): 261-273.

Tanimura, A.; McGregor, D.; and Anderson, C. 1986b. Calcification in atherosclerosis, II: Animal studies. *Journal of Experimental Pathology* 2(4): 275-297.

Thyberg, J. et al. 1983. Phenotype modulation in primary cultures of arterial smooth muscle cells on the role of platelet-derived growth factor. *Differentiation* 25(2): 156-167.

Urry, D. W. 1974. Molecular basis for vascular calcification. *Perspectives in Biology and Medicine* 18(1): 68-84.

Virchow, R. 1856. *Gesammelte Abhandlungen zur wissenschaftlichen Medizin.* Berlin: Meidinger Sohn.

Vogel, J. J. and Boyansaylers, B. D. 1976. Acidic lipids associated with local mechanism of calcification: Review. *Clinical Orthopaedics and Related Research* (118): 230-241.

UIST LIBRARY

Wuthier, R. E. and Eanes, E. D. 1975. Effect of phospholipids on transformation of amorphous calcium-phosphate to hydroxyapatite in vitro. *Calcified Tissue Research* 19(3): 197-210.

Yu, S. Y. 1974. Calcification processes in atherosclerosis. *In*: T. Clarkson, ed. *Arterial mesenchyme and atherosclerosis*. New York: Plenum Press. pgs. 403-425.

Yu, S. Y. and Blumenthal, H. T. 1963. The calcification of elastic fibers, I: Biochemical studies. *Journal of Gerontology* 18: 119-126.

UCSF LIBRARY

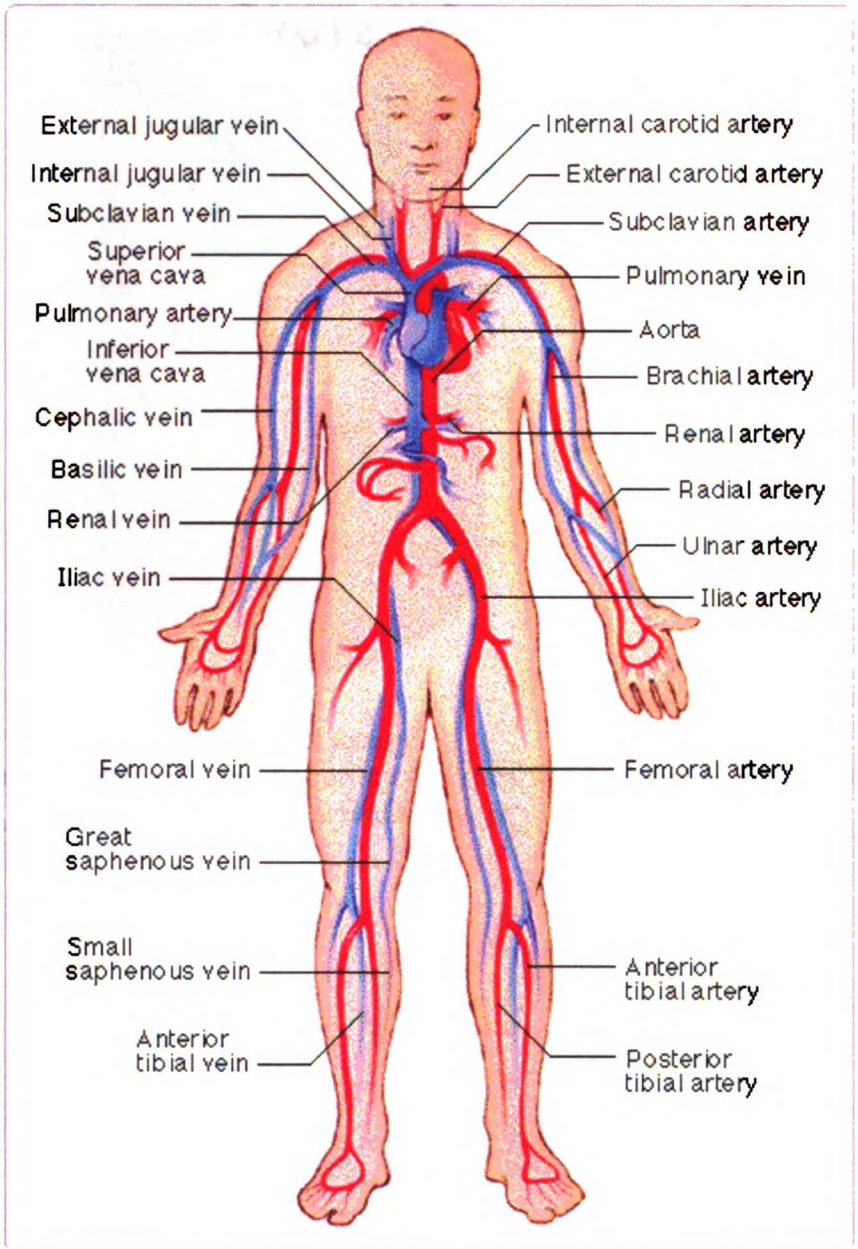

Figure 2.1: Human cardiovascular system

(*Source: www.ama-assn.org/ama1/pub/upload/images/446/circulationgeneral.gif*)

UCSF LIBRARY

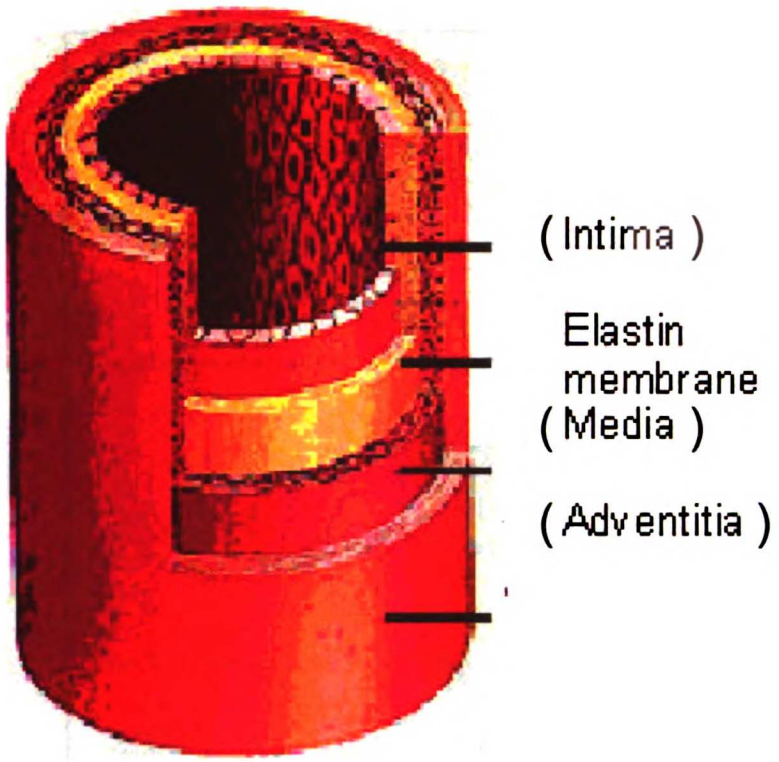

Figure 2.2: Anatomy of a normal artery
The three main layers of a normal artery are specified within the parentheses (*Adapted from: www.fatsoflife.com/images/Carotidartery.jpg*)

LIBRARY

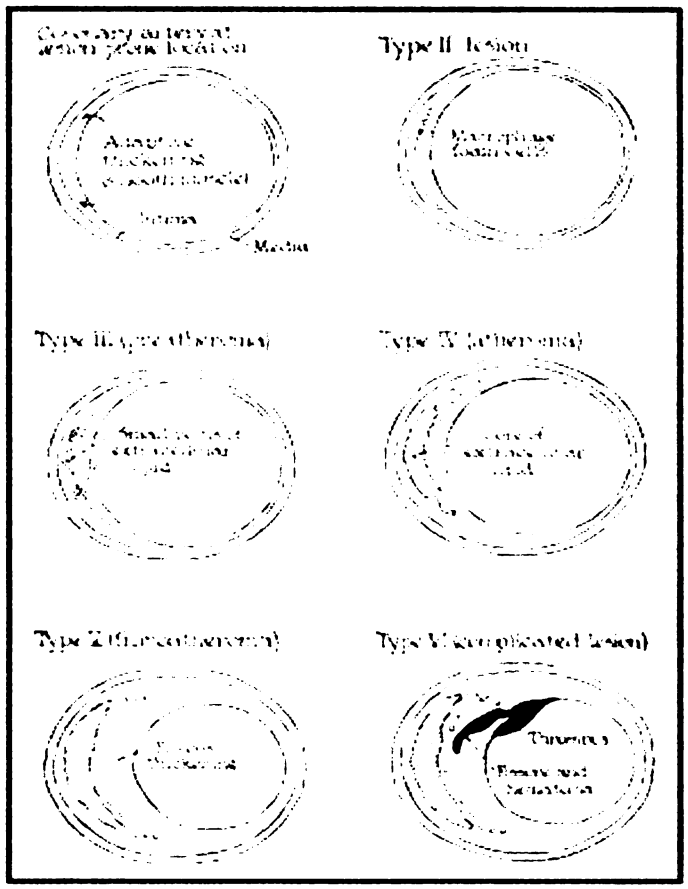

Figure 2.3: Atherosclerotic disease progression
Schematic of Stary's classification system for atherosclerotic disease progression (*Source: Stary 1995*)

ULST LIBRARY

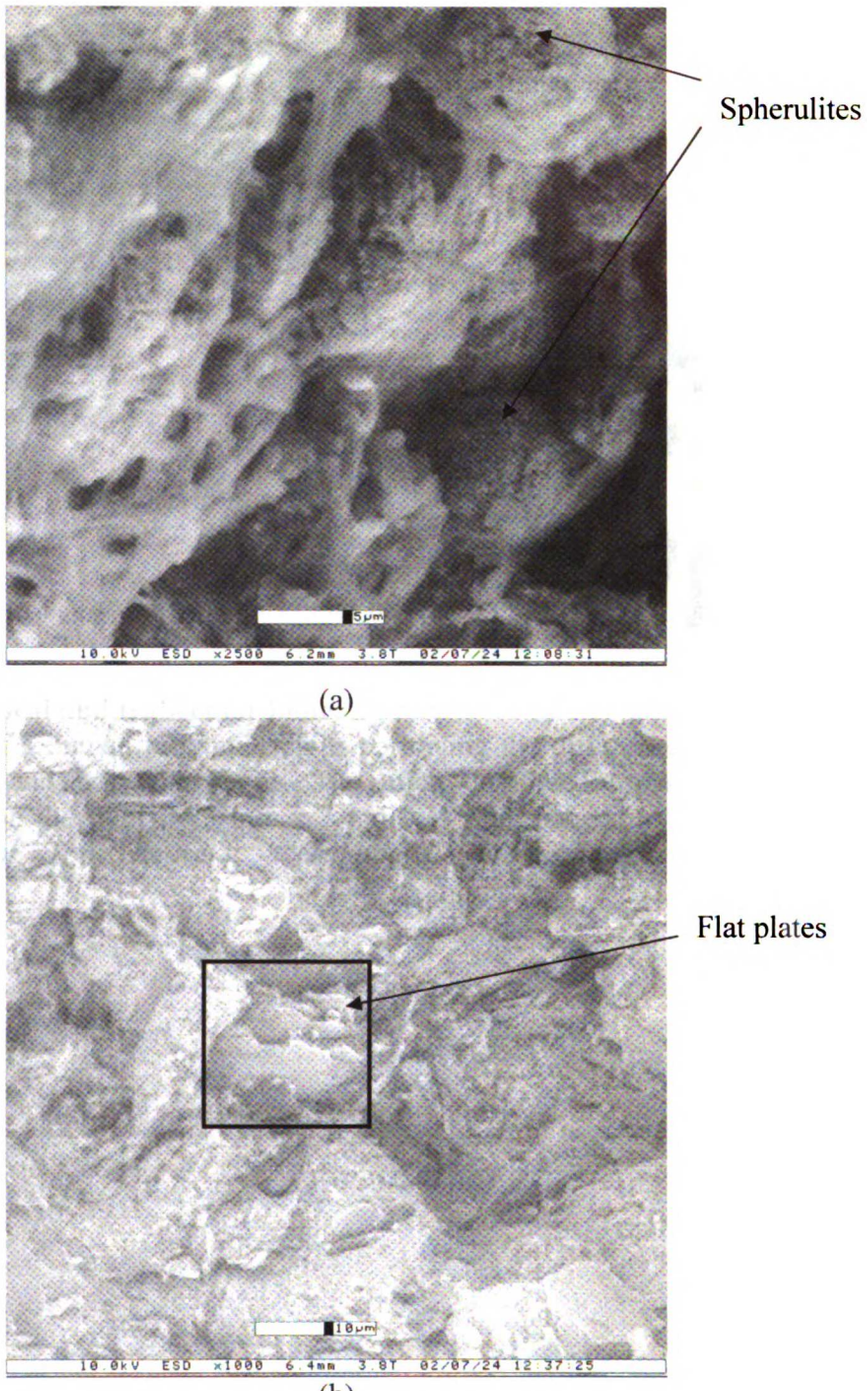

Figure 2.4: Atherosclerotic calcification microstructure
Environmental scanning electron images of two types of atherosclerotic calcification microstructure: (a) spherulites (magnification of 2500x) and (b) flat plates (1000x). The calcifications were scanned at 10kV.

ULST LIBRARY

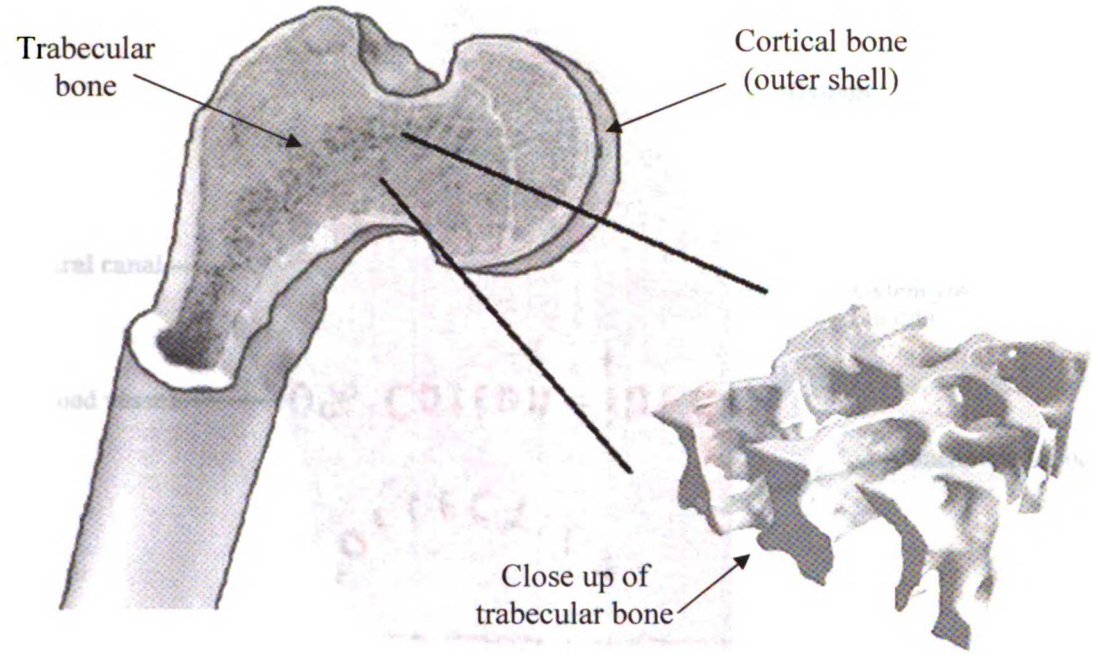

Figure 2.5: Cortical and trabecular bone
A cross section of a human proximal femur portraying the differences of bone density between cortical and trabecular bone. The micro-computed tomography image of trabecular bone (on the right) is 3 mm x 3 mm x 1 mm, imaged at 22 μm resolution. (*Courtesy of Prof. Tony Keaveny – Orthopaedic Biomechanics Laboratory, U.C. Berkeley*)

UCSF LIBRARY

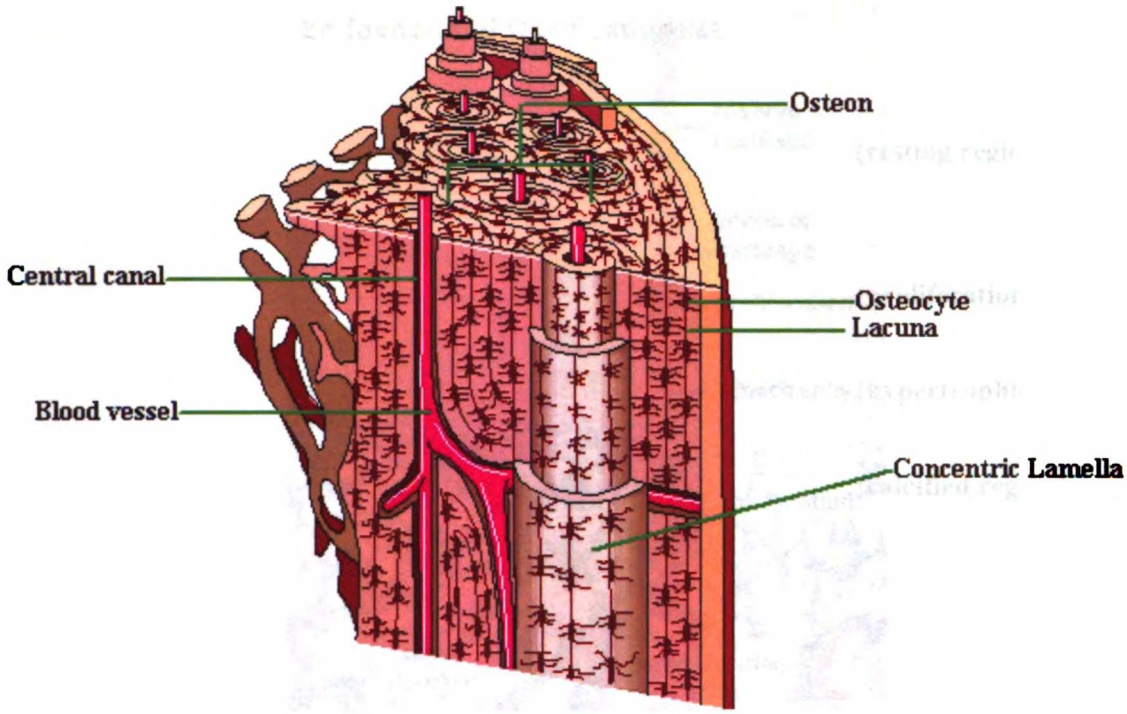

Figure 2.6: Bone microstructure
Illustration of a cross-section of bone showing the concentric lamella that form an osteon (*Source: www.dmacc.edu/instructors/rbwollaston/Cells_and_Tissues/ bone_microscopic_structure.gif*)

UCSF LIBRARY

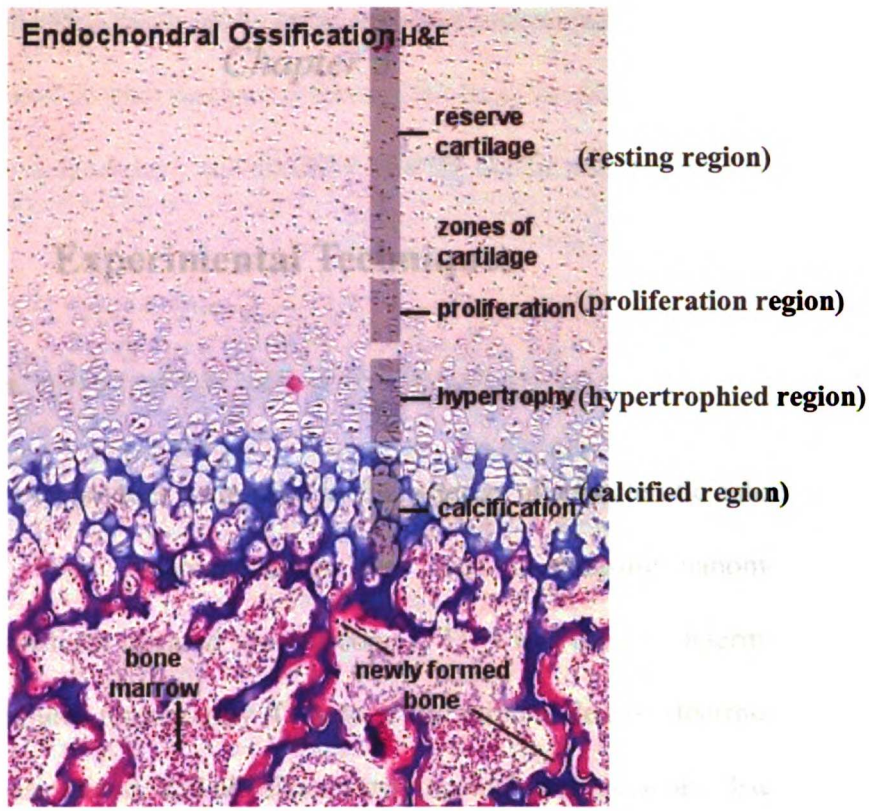

Figure 2.7: Endochondral ossification
Haematoxylin and eosin staining of a cross-section of cartilage, ossification center, and bone depicting the four distinct region of endochondral ossification: the calcified region, the hypertrophied region, the proliferation region, and the resting region (reserve cartilage)
Adapted from:
www.lab.anhb.uwa.edu.au/mb140/CorePages/Bone/Images/enos04he.jpg

UWF LIBRARY

Chapter 3

Experimental Techniques

3.0. Introduction

Three different techniques were used to characterize atherosclerotic calcifications and, in some cases, bone. Nanoindentation was used to measure nanomechanical properties; Fourier transform infrared spectroscopy (FTIR) was used to determine tissue composition; and computed tomography (CT), to reveal mineral density distribution. This chapter reviews the basic theory and physics underlying each technique and discusses the function of the main component(s) of each testing apparatus.

UCSF LIBRARY

3.1. Nanoindentation

Nanoindentation was originally developed to study micro- and nano-mechanical properties, especially micro- and nano-hardness. For this, a depth-sensing testing device indents a sample while continuously calculating the applied force and depth of indentation. This information is then used to calculate the sample's hardness.

Nanoindentation was later altered to measure the elastic modulus. This led to the widespread testing of thin films, especially in the silicon industry (Bhushan 1999). Since then the technique has been extended to test biological tissues including bone, teeth, cartilage, and some constituents of plaque (Jae-Young, Tsui et al. 1997; Marshall, Balooch et al. 2001; Ebenstein 2002; Ebenstein, Kuo et al. 2004). To better understand

this technique, the following sections describe the main component of the nanoindenter used in this study, review contact mechanics theory (the basis for determining mechanical properties such as elastic modulus), and describe how the elastic modulus is measured.

3.1.1. Triboindenter

All roughness measurements and nanoindentations were conducted using a Triboindenter (Hysitron, Inc. Minneapolis, MN) (Figure 3.1). Since the nanomechanical study used bone as a control, a three-sided pyramid diamond indenter tip known as the Berkovich tip was chosen since that shape is most commonly used to measure the nanomechanical properties of bone (Figure 3.2). This allows the validation of bone properties obtained in this study by comparing them against those in literature.

The most important component of the Triboindenter is the transducer. This component is used to produce a force and to measure the depth of penetration into the tissue of interest. It has a three-plate capacitor: the outer plates are fixed in position and the center plate is mounted to the housing by springs (Figure 3.3) (Asif et al. 1999; Hysitron 2001). The indenter tip is screwed into a holder in the center plate. To apply a force onto a sample, a voltage is produced between the bottom and center plates, creating an electrostatic force that pulls down the center plate and, hence, the indenter tip (Asif et al. 1999; Hysitron 2001).[7] The force applied to the indenter can therefore be correlated to the magnitude of the voltage. As the center plate moves in relation to the fixed plates, a capacitance is generated, which can be correlated to the displacement of the indenter tip

UCSF LIBRARY

(Asif et al. 1999).[7] Because of the high sensitivity of the transducer, it has a very high load resolution of ~ 100 nN and a displacement resolution of ~ 1 nm (Hysitron 2001).

3.1.2. Contact Mechanics Theory

In the late 19th century, Boussinesq and Hertz founded the theory of contact mechanics by modeling the contact between surfaces (Boussinesq 1885; Hertz 1896). Boussinesq modeled the stress distribution in an elastic material that is indented by a rigid, axisymmetric indenter (primarily a flat punch). Hertz, on the other hand, modeled the contact deformation of two spheres of different elastic moduli. Later, in the 1960s, (Sneddon 1965) extended these earlier studies by investigating the contact mechanics of a rigid indenter on an elastic half space. The importance of Sneddon's work was that he derived a relationship between the applied load, P, and indenter penetration depth, h:

$$P = \frac{4\mu a h}{1-\nu} \tag{3.1}$$

where μ is the shear modulus and ν is the Poisson's ratio of the substrate material. Taking the derivative with respect to depth of penetration yields:

$$\frac{dP}{dh} = \frac{4\mu a}{1-\nu} \tag{3.2}$$

Pharr et al. showed that this relationship is true for any indenter whose geometry can be described as a solid of revolution of a smooth function (Pharr et al. 1992). The indenter tip would thus have a projected area, A, equal to πa^2. For an elastic and isotropic substrate material, $\mu = (E/2)(1+\nu)$, where E is the Young's modulus. Substituting these two conditions into equation (3.2) gives:

[7] For more information on determining the force and displacement, see Ebenstein (2002).

UCT LIBRARY

$$\frac{dP}{dh} = \frac{2\sqrt{A}E}{\sqrt{\pi}(1-\nu^2)} \tag{3.3}$$

Theoretically, equation (3.3) can be used on the loading or unloading curve of a load vs. displacement plot (Figures 3.4 and 3.5). However, empirical data shows that the loading curve contains both elastic and plastic deformation, while the unloading curve (especially the initial part of the unloading curve) is dominated by the elastic deformation of the substrate material (Nix 1997). So *dP/dh* can be defined as the unloading stiffness, *S*. Moreover, equation (3.3) assumes that indenter tip does not deform. If instead the indenter is assumed to be elastic and have an elastic modulus, E_i, and a Poisson's ratio, ν_i, then the following relationship applies:

$$\frac{1}{E_r} = \frac{(1-\nu^2)}{E} + \frac{(1-\nu_i^2)}{E_i} \tag{3.4}$$

where E_r is the reduced modulus (Stilwell et al. 1961). This changes equation (3.3) to:

$$S = \frac{dP}{dh} = \frac{2\sqrt{A}E_r}{\sqrt{\pi}} \tag{3.5}$$

Solving for *Er* yields:

$$E_r = \frac{S\sqrt{\pi}}{2\sqrt{A}} \tag{3.6}$$

Finite element analysis studies show that equation (3.6) needs to be slightly altered for indenter tips that cannot be described by a solid of revolution of a smooth function (i.e., a Berkovich tip [three-sided pyramid producing a triangular projected area] or a Vickers tip [four-sided pyramid producing a square projected area]):

$$E_r = \beta\frac{S\sqrt{\pi}}{2\sqrt{A}} \tag{3.7}$$

where β = 1.034 is for a triangular projected area; β = 1.012 is for a square projection area; and β = 1, for a circular projection area (Oliver et al. 1992). Comparing equations (3.6) and (3.7), the maximum error in E_r for a Berkovich tip is 3.4% or, for a Vickers tip, 1.2%. Since, for these tips, the error is small, the correction factor is usually neglected (i.e., $\beta = 1$).

3.1.3. Applying the Theory of Contact Mechanics

For many materials, Oliver et al. (1992) later observed that the unloading curve can be modeled with the following power function:

$$P = \alpha(h - h_f)^m \tag{3.8}$$

where α and m are constants and h_f is the final depth. These three variables can be determined by a least squares fit of the unloading curve. Taking the second derivative, the function becomes:

$$S = \frac{dP}{dh} = \alpha m(h - h_f)^{m-1} \tag{3.9}$$

Since the initial portion of the unloading curve in a load versus displacement plot is considered elastic, the stiffness is measured at the maximum displacement (h_{max}). Thus,

$$S^* = \left(\frac{dP}{dh}\right)_{(h_{max}, P_{max})} = \alpha m(h_{max} - h_f)^{m-1} = \frac{2\sqrt{A}E_r}{\sqrt{\pi}} \tag{3.10}$$

where S^* is the stiffness at maximum displacement (Figure 3.5). Equation (3.10) is an important relationship for experimentalists because it allows for the calculation of the reduced modulus from a load versus displacement curve if there is an independent way to determine the projected area.

UMIST LIBRARY

Oliver et al. (1992) developed a method to calculate independently the projected area as a function of displacement by conducting separate indents on a calibrating material. The main prerequisite in their method is that the Young's modulus of the calibrating material be constant with depth.[8] In addition, the calibrating material's Young's modulus and Poisson's ratio should be calculated by other means, e.g., conventional tests. If these two properties are known for the calibrating material and the indenter tip, the reduced modulus of the calibrating material can be calculated using equation (3.6). Then, by taking indents at several depths, the stiffness can be calculated by using the left side of equation (3.10) for each indent and the area can be calculated by rearranging the right side of equation (3.10) to:

$$A_c = \frac{\pi}{4}\left(\frac{S^*}{E_r}\right)^2 \tag{3.9}$$

where A_c is the projected area at contact height, h_c (Figure 3.4a). The data can then be plotted as contact area vs. contact depth. In this study, since a Berkovich tip was used, the ideal area function is:

$$A = 24.5h_c^2 \tag{3.10}$$

However, a more accurate area function for a Berkovich tip is:

$$A_c = C_0h_c^2 + C_1h_c + C_2h_c^{1/2} + C_3h_c^{1/4} + C_4h_c^{1/8} + C_5h_c^{1/16} \tag{3.11}$$

where $C_0 = 24.5$. A least square fit is applied to the data to determine the other constants.

Once the area function for the tip is obtained using the calibrating material, equation (3.6) can be used to calculate the reduced elastic modulus for the tissue as long

[8] Since Klapperich et al. found that polycarbonate can be used as a standard material; it was used for the present study (Klapperich et al. 2001).

MIT LIBRARIES

as it is indented within the calibrated depth. Therefore, many indents can be performed along the tissue surface to obtain an average elastic modulus for the tissue.

3.2. Fourier Transform Infrared Spectroscopy

Fourier transform infrared spectroscopy (FTIR) is a method that uses infrared radiation to determine the chemical composition of materials by determining the functional groups that make up the material. A functional group is a portion of molecule characterized by its elements and connectivity (e.g., hydroxyl group is an oxygen, O, bonded to a hydrogen, H, forming -OH and a methyl group is a carbon, C, bonded to three hydrogen forming $-CH_3$). When radiation is transmitted through a material, each functional group within the material will absorb a unique frequency of energy that causes the bonds between the functional group to vibrate (e.g., stretch and compress or bend) at that frequency. Since materials are made up of a unique combination of chemical functional groups, the different frequencies of absorbed energy provide a "fingerprint" for determining the type of material present.

UMIST LIBRARY

Having many advantages, this technique is widely used in the study of biological tissues (Boskey et al. 1992; Gadaleta et al. 1996a; Hallsworth et al. 1973; Hsu et al. 2000). It does not require much material; the material can be analyzed nondestructively; it can provide quantitative histochemical information; and it is fast since it does not require time-consuming processes like staining. To gain a better understanding of this technique, the following sections describe the main components of a Fourier transform infrared spectrometer and review the physics behind such technique.

3.2.1. Spectrometer

The core components and principles of both FTIR systems used in this study are based on the Michelson interferometer. The purpose of an interferometer is to split the infrared beam into two, by making one beam travel a different distance than the other, and then to collect the two beams. To do this, the Michelson interferometer has five main components in a form of a cross: the source is placed opposite to a fixed mirror and, perpendicular to this, the detector is placed opposite a moving mirror (Figure 3.6). A beam splitter is then placed in the intersection of all these components. The beam splitter transmits half of the signal to the fixed mirror and reflects the other half to the moving mirror. The beam splitter also recombines the two signals after they have reflected off their respective mirrors and then transmits the new signal through the sample. The sample absorbs a portion of the signal while the transmitted signal is collected by a detector.

When the mirrors are an equal distance from the beam splitter, the two split signals travel the same distance. To create a difference in distance traveled (i.e., an optical path difference), the movable mirror is translated at a constant velocity. This causes a constant change in the light intensity transmitted through the sample and to the detector. The detector collects the signal and, in turn, produces an electrical signal proportional to the intensity of the infrared radiation. This electrical signal is used to calculate and plot light intensity versus optical path difference, more correctly known as in interferogram, the importance of which is explained in the next section.

Two types of spectrometers were used in this study: a regular spectrometer whose main components are described above and a FTIR in attenuated total reflectance (ATR)

UMIST LIBRARY

mode. The main addition in the FTIR-ATR system is an infrared transparent crystal (this study used a germanium crystal) with a high refractive index. The sample is clamped to the crystal. The recombined signal is focused with the proper angle through the crystal such that the signal does not leave the crystal immediately because of its high refractive index but, instead, is reflected a few times within the crystal. This creates a standing wave (i.e., an evanescent wave) that is a little larger than the crystal (Figure 3.7). This causes the wave to slightly penetrate the surface of the crystal and be transmitted through, typically, 0.1 to 5 μm of the sample (Smith 1996). The sample attenuates the signal, which is sent back into the crystal until eventually it leaves and is collected by the detector. Since the signal only penetrates the surface of the sample, FTIR-ATR is more of a surface characterization technique.

UCSF LIBRARY

3.2.2. Fourier Transform Infrared Spectroscopy Physics

Infrared spectroscopy is able to determine the unique combination of chemical functional groups within a material by irradiating infrared energy (i.e., energy in the $3 \cdot 10^{12}$ - $3 \cdot 10^{14}$ Hz region of the electromagnetic spectrum) through a material and detecting the amount of vibrational energy absorbed by the chemical functional groups at the different frequencies. These chemical functional groups always vibrate at the same frequency no matter what material they are in (Smith 1999). However, not all functional groups absorb infrared light.

Chemical functional groups can absorb infrared light *only if* the change in the dipole moment of the chemical functional group with respect to bond distance is nonzero;

otherwise, it is infrared inactive (Smith 1999).[9] For example, the anti-symmetric vibrational stretching and compressing or bending of the CO_2 molecule produces a change in dipole moment with respect to bond distance, which can be detected by infrared spectroscopy. On the other hand, the symmetric stretch of the oxygen bonds in CO_2 with respect to the carbon results in a net dipole moment equal to zero and, therefore, the change in dipole moment with respect to bond distance is zero. So, this chemical functional group's symmetric vibration is deemed infrared *inactive* though the anti-symmetric vibration is not.

Another important concept in FTIR is how the absorption of energy is related to quantum energy levels. At room temperature, many molecules are most stable at the minimal potential energy where the bond length is considered to be at equilibrium. This energy level is described as the zero vibrational quantum number (v). There are increasing levels of discrete vibrational energy known as vibrational quantum levels, e.g., $v = 1, 2, 3$, etc. A material will only absorb radiation equal to the difference in vibrational energy levels, e.g., difference between $v = 0$ and $v = 1$ (Smith 1999). These differences are known as transitions. The fundamental transition occurs between $v = 0$ and $v = 1$. Overtone transitions occur between other levels such as $v = 0$ to $v = 2, 3$, etc. Increasing amounts of absorbed energy causes increasing bond length.

The amount of energy absorbed in each transition is usually expressed in absorbance units, A_λ. This unit is defined by the Beer-Lambert law that relates the absorbance unit to the concentration of the sample (c), the path length (l), and molar absorption coefficient (ε). The molar absorption coefficient is a material property that is

[9] A dipole moment is a measure of asymmetric distribution of charge in a molecule (Smith 1999).

UMSL LIBRARY

constant for a given wavelength and is proportional to the square of the change in dipole moment with respect to bond distance. The absorbance unit may also be related to the incident intensity, I_o, and transmitted intensity, I:

$$A_\lambda = \varepsilon_\lambda cl = \log(\frac{I_0}{I}) \tag{3.12}$$

The detector measures the intensity of light of the recombined signal that has been transmitted through the sample. This intensity of light changes depending on the optical path difference. For a monochromatic signal (i.e., a signal of a single energy level), the two signals recombine constructively (i.e., are in phase) and have a high intensity if the two mirrors are the same distance from the beamsplitter or if the moving mirror is at a distance where the optical path difference is a multiple of the wavenumber of the signal, λ. By contrast, they combine destructively and have no intensity if the signals are out of phase (i.e., at optical path differences of $\lambda(n+1)$, where n = 0, 1, 2 . . .). At other optical path differences, the signal has both constructive and destructive interference.

By displacing the moving mirror at a constant velocity, the light intensity measured by the detector changes. For a monochromatic signal, the interferogram (light intensity vs. optical path difference) is a cosine wave function. A complete interferogram is obtained by translating the moving mirror through one cycle, i.e., one scan. In general, the signal-to-noise ratio can be improved by increasing the number of scans since some fluctuations in noise will cancel each other out of the signal.

In FTIR, the infrared signal is not monochromatic, but is composed of radiation of a continuous range of wavelengths (2.5 μm - 25 μm), each wavelength having its unique optical path difference and frequency. The interferogram of a polychromatic signal is the

UMSL LIBRARY

addition of all the interferograms at each wavenumber (Figure 3.8). Such an interferogram contains a high intensity spike, i.e., centerburst, at the zero optical path difference where all the signals of each wavenumber are constructively interfering. As the optical path difference increases in either direction, the interference is increasingly destructive and, hence, the signal intensity decreases away from the centerburst.

This interferogram is then Fourier transformed to obtain an infrared spectrum (a plot of light intensity versus wavenumber), which is converted to absorption units versus wavenumber using equation (3.12) (Figure 3.9). A wavenumber is the reciprocal of wavelength and thus has units of cm^{-1}. In the mid-infrared region used in this study, the wavenumber range is between 4000 cm^{-1} and 400 cm^{-1}.

The infrared spectrum of a molecule with many atoms can be quite complex because the number of vibrational modes depends on the number of atoms (N) in a molecule and whether the molecule is linear ($3N$-5) or nonlinear ($3N$-6) (Smith 1999). Each vibrational mode results from the absorption of energy at a given frequency if the vibrational mode causes a change in dipole moment with respect to bond distance.

To determine the absorption peaks of a sample, several points should be considered. Since different functional groups may absorb nearly the same frequency, overlapping bands may create one broad, complex band shape in the spectrum (Figure 3.9). In addition, slight shifts can occur in the wavenumber at which a functional group absorbs energy since the frequency of absorption depends on the force of the chemical bond and the mass of the atoms. Electronic effects are caused by interactions of near-by functional groups that may affect the electron distribution and, hence, the force of the chemical bonds. Changes in the mass of a molecule (e.g., an isotope) may also cause a

UMSL LIBRARY

wavenumber shift. Since an excited bond may partially excite another bond, vibrational interactions may also cause a shift in the wavenumber at which a functional group absorbs energy. Aside from these shifts, the band's width may also be affected by the type of intermolecular interactions. Stronger intermolecular interactions produce more electronic effects. Thus, within a sample, a type of functional group may absorb energy at slightly different wavenumbers, which, in turn, broaden the absorption band.

3.2.3. Fourier Transform Infrared Spectroscopy Spectrum

To obtain the infrared spectrum (i.e., absorption vs. wavenumber) of a sample, the data must undergo two main processes: *(i)* taking the Fourier transform of the interferogram and *(ii)* subtracting out the incident radiation. Ideally, a Fourier transform of an interferogram would involve performing an integral between the positive and negative infinite optical path differences. Since it is not possible to get infinite optical path differences, the integral must be taken at finite amounts of optical path differences. This affects the spectrum by producing sinusoidal undulations (lobes) in the baseline (Figure 3.10) (Smith 1996). These effects can be reduced by multiplying the interferogram by an apodization function (Smith 1996).

The present study used a Happ-Genzel apodization function before the interferometer was Fourier transformed. For the data collected in this study, this apodization function offered the best balance of reducing the side lobes without substantially degrading the resolution.

One way to measure the incident radiation is by taking a background spectrum. This spectrum depends on the type of sample. For a *non-embedded sample,* a background

UVSF LIBRARY

spectrum is a measure of the incident radiation through an empty sample compartment. For an *embedded sample,* the background spectrum would measure the incident radiation through the embedding medium. The advantage of taking the background spectrum in both methods is that the spectrum includes the instrument's contributions to the signal (e.g., "sensitivity of the detector, transmission and reflection properties of the beamsplitter, emissive properties of the source, and reflective properties of the mirrors") and the environment (e.g., water vapor and carbon dioxide) (Smith 1996). Since this background signal provides information about the incident intensity, I_o, equation (3.12) can be used to calculate the absorbance units.

As previously mentioned, functional groups may absorb energy at wavenumbers close to each other and thus form a broad, complex band comprising many overlapping bands. One way to determine the underlying bands of a broad band is to take the second derivative of the infrared spectra. In the second derivative plot, the position of a negative peak indicates the underlying peak's position. Some overlapping peaks may be discerned since this process generates negative bands of smaller widths, i.e., their width measured at half the band's height is approximately three times smaller than the broad band (Maddams et al. 1982c). The technique, however, has disadvantages. Usually two positive peaks appear on each side of the central negative peak and may interfere with a negative peak and thus obscure its presence (Leung et al. 1990). The technique may also underestimate the number of underlying peaks within the broad peak since, for example, with absorption peaks of equal amplitude, the ratio of the second derivative's band amplitudes varies inversely to the square of the ratio of their widths at half the band height (Maddams et al. 1982b). So bands of large widths may not be discernable.

UMIST LIBRARY

3.3. Micro-Computed Tomography

Computed tomography (CT) is a noninvasive medical imaging technique. It utilizes x-ray radiation to obtain three-dimensional cross-sectional images of the anatomy and composition within a body or tissue. X-rays are transmitted through an object of interest, which then attenuates the signal by absorbing and/or scattering part of the x-ray beam. The amount of attenuation uniquely characterizes tissues since it is dependent on the density and composition of the tissue and thus, it can be used to distinguish tissue types.

Micro-computed tomography's (μCT) advantage over conventional CT instruments is that its imaging spatial resolution is higher (10 - 36 μm compared to, at most, about 50 μm in conventional in vivo CT instruments for humans); therefore, it allows detailed studies of much smaller tissues. For instance, μCT has been successfully used to study tissue architecture such as that of trabecular bone (Bikle et al. 2001; Hara et al. 2002). An additional feature in μCT is that the grayscale levels of a μCT image have been correlated to mineral density measurements, allowing for the construction of three-dimensional images of the mineral density distribution (Mulder et al. 2004; Nuzzo et al. 2002). To better understand this technique, it is first important to review the basis of μCT instrumentation, the physics involved in μCT, and how images are obtained.

UMSL LIBRARY

3.3.1. Micro-Computed Tomography System

The main components of the μCT system (μCT-40, Scanco Medical AG, Bassersdorf, Switzerland) used in this study are the x-ray tube, filters, collimators, multiple x-ray detectors, and data processing system. A general schematic of this system

is given in Figure 3.11. The x-ray tube irradiates a continuous conically shaped x-ray beam. The x-ray beam passes through filters that remove the long wavelength x-rays since these are most likely to scatter and be absorbed, as later explained (Seeram 2001). A collimator is positioned after the filter to restrict the beam to be transmitted through a specific thickness of the subject sample. This collimated beam is then transmitted through a 30 mm diameter polymethylmethacrylate hollow cylinder (1 mm thick) containing the tissue(s) of interest.

Unlike conventional CT systems, the μCT system's x-ray tube does not rotate around the specimen to capture various projections of the sample; the importance of acquiring various projections is described in the next section. Instead, the x-ray tube is stationary and the stage containing the cylinder (and samples) rotates (Figure 3.11). Although the width of sample holder is located entirely within beam's path, the beam only goes through a specified thickness of the tissue. For this reason, the stage must be moved vertically to capture the next increment in height.

Once the x-ray is transmitted through the tissue(s), the transmitted beam goes through another collimator designed to shield the detectors from receiving scattered radiation. The collimator also ensures that the detector receives a constant width of the x-ray signal (Seeram 2001). After going through the second collimator, the x-ray signal is captured by multiple x-ray detectors. These detectors are placed side by side in an array (2048 x 256) to capture all of the transmitted radiation.

The detectors create an electrical signal proportional to the amount of transmitted x-ray radiation. This electrical signal is then sent to the data processing system. This is done for each degree of sample rotation and each incremental thickness. The data

USF LIBRARY

processing system acquires this signal and converts it into a digital signal used to create a gray-scale three-dimensional image. This process is called image reconstruction and is presented in more detail in the section below.

3.3.2. Micro-Computed Tomography Physics

In CT, x-ray attenuation is the principal phenomenon exploited to form three-dimensional images. This section explains the basic physics behind x-ray attenuation and how three-dimensional images of the composition of tissue are reconstructed.

There are three main modes of attenuation. The primary mode of attenuation is photoelectric absorption. This type of absorption occurs when x-ray energy is transmitted to an inner electron of an atom in the tissue, supplying the electron with enough energy to overcome the binding force of the atom and travel away from it. The probability of photoelectric absorption occurring depends on the x-ray energy level and the atomic composition of the tissue. The probability decreases with increasing x-ray energy (Ex) with a relationship close to $1/Ex^3$, and the probability also increases with increasing atomic number (Z) of the tissue with a relationship close to Z^3 (Hendee 1983). Since calcified tissues, such as bone and atherosclerotic calcifications, mainly consist of atoms of high atomic numbers (i.e., calcium and phosphorus), these tissues experience greater amounts of photoelectric absorption than other tissues, especially soft tissue.

Besides absorption, x-ray beams may also be attenuated by x-ray scattering. There are two primary scattering processes: Compton and coherent scattering. Compton scattering is the most common scattering process, mainly occurring at higher x-ray energy levels. In this process, some of the x-rays' energy is transferred to the outer

UMSL LIBRARY

electrons of an atom of tissue, giving the electron enough energy to free itself from the electron shell. The x-ray signal is, in turn, decreased in energy and scattered in a new direction. These scattered x-rays can interfere with the attenuated signal. For this reason, the scattered x-rays are collected and removed by a collimator placed between the tissue and the detectors (Hendee 1983). The probability that Compton scattering occurs increases with the increasing tissue density and tissue electron density (Hendee 1983).

Unlike Compton scattering, coherent scattering is dominant at low energy levels. In coherent scattering, x-rays interact only slightly with the atoms in the tissue, causing the x-ray to scatter in a different direction with little loss of energy. Since photoelectric absorption and coherent scattering occur most frequently at lower energy levels, these energy levels are filtered out of the x-ray signal (Hendee 1983).

Despite the different attenuation processes, the total attenuation may be lumped into a material parameter, μ, the linear attenuation coefficient, which has units of 1/length. The linear attenuation coefficient is related to three modes of attenuation by:

$$\mu = \rho_e(k_1 Z^{1.69} + k_2 Z^{3.58} + k_3 Z^{-0.03}) \tag{3.13}$$

where ρ_e is the volume electron density; Z is the atomic number; and k_1, k_2, and k_3 represent the fraction of each kind of attenuation (coherent scattering, photoelectric absorption, and Compton scattering, respectively) (Hendee 1983).

In μCT, polyenergetic radiation (i.e., x-rays having a range of energies) is used. In this case, the transmission radiation intensity, I, through a tissue of thickness x can be described by:

UMJT LIBRARY

$$I = \sum_{K=1}^{n} I_o(E_K) e^{-\mu(E_K)x} \tag{3.14}$$

where $I_o(E_K)$ are the intensities of the incidence x-rays for each of the n x-ray energies and $\mu(E_K)$ represents the linear attenuation coefficients for at each energy level. The incidence intensity is measured by not placing a sample in the path of the beam. In general, since each tissue has a unique combination of volume electron density and atomic number, each tissue has a unique average linear attenuation coefficient and, therefore, tissues can be theoretically distinguished from one another. In the same manner, since tissues are not homogeneous, they also have a distribution of linear attenuation coefficients within their volume.

3.3.3. Image Reconstruction

Reconstruction is considered the conversion of all the projection attenuation data into a three-dimensional image, with each voxel (i.e., three-dimensional cube in space) having its own linear attenuation coefficient. Though several methods of image reconstruction exist, the present study uses Feldkamp filtered back-projection (Feldkamp et al. 1984). The following example explains simple back-projection. The example is for a monochromatic beam whereby the main assumption is that each section of tissue contributes equally to the total absorption. To illustrate, assume a tissue in form of a cube and let the space in which it lies be imaginarily segmented into 10 x 10 x 10 voxels, where the cube occupies 4 x 4 x 4 voxels. If the intensity of an x-ray transmitted through one cross-sectional slice of tissue (i.e., 1 x 10 voxels) is measured to be 20% of the incident intensity (thus having absorbed 80% of the signal), then each voxel is assumed to attenuate the signal by 8% (Figure 3.12). Since the length through which the x-ray

UWT LIBRARY

travels is known, then the linear attenuation coefficient can be calculated by rearranging equation (3.14) for a monochromatic case:

$$\mu = \frac{1}{x} \ln \frac{I_o}{I} \tag{3.15}$$

and assigning the linear attenuation coefficient to each voxel. The disadvantage of this method is that values of the linear attenuation coefficients are assigned even to the space that has no tissue. Thus, more projections must be made at different angles and superimposed to obtain more accurate linear attenuation coefficient values for each voxel. Each level of attenuation can be assigned a grayscale value: white being the most absorbent and black the least. Therefore, superimposing the attenuation measurements at different angles creates a more accurate grayscale cross-sectional image. The higher the number of x-rays that are projected through a sample at different angles, the greater the accuracy of the image. This is repeated for different cross-sections, which are then stacked to create a three-dimensional image.

One problem with this type of reconstruction is that it causes blurring and creates "spoke-like" patterns that extend beyond the tissue since the attenuation is averaged over the entire transmission x-ray length and not just the tissue length (Hendee 1983). These errors occur especially in regions of high density. These regions absorb much of the signal and consequently any voxel in the projected x-ray length, even if it is not part of the tissue, will have a high linear attenuation coefficient. In this study, an algorithm developed by Feldkamp et al. (1984) was used to reconstruction the image that also involves convolution to filter the noise and three-dimensional back projection to

UWF LIBRARY

reconstruct the three-dimensional image. This type of reconstruction was chosen as it was specifically designed for x-ray beams that are coned shaped (as it is in the μCT 40 system), have higher computation efficiency, and may produce less image noise.

3.3.4. Beam Hardening Corrections

As a polychromatic x-ray beam is transmitted through tissue, its average energy increases since lower energy x-rays are readily absorbed. This process (known as beam hardening) can cause artifacts in an image. The amount of beam hardening depends on thickness. Thicker tissues produce a higher level of beam hardening since the x-ray must traverse more tissue, thus more tissue exists to absorb lower energy radiation.

Scanco Medical AG, the manufacturer of the μCT 40 system, corrects for thickness-dependent beam hardening by imaging a 200 mg/cm^3 hydroxyapatite-epoxy resin mixture in the shape of a step wedge phantom at each voltage source (45, 55, 70 kV). The concentration of hydroxyapatite-epoxy was chosen because it nearly equals the mineral density of whole bone of small animals (the most commonly studied sample in μCT). Although atherosclerotic calcifications have a slightly higher mineral density than that of whole bones of small animals, this method was used because it substantially corrects for beam hardening and, hence, no beam hardening artifacts appeared in the images.

For calibration, the natural log of the transmitted intensity divided by the incident intensity was plotted against the wedge thickness and a third-order polynomial was fit to this data. This equation (known as the voltage-specific beam hardening correction factor) was used to correct for beam hardening.

UVSF LIBRARY

3.3.5. Mineral Density Calibration

Since calcified tissue such as bone and atherosclerotic calcifications are mainly composed of a distribution of hydroxyapatite and some matrix, the regions of more hydroxyapatite (i.e., more dense and high atomic number material) absorb more x-ray energy and thus appear whiter in a grayscale image than the matrix. Thus, one can convert a grayscale image into an image illustrating the distribution of mineral density. To perform such calibration, five cylindrical phantoms composed of hydroxyapatite-resin mixture having mineral concentrations of 0, 100, 200, 400, 800 mg/cm^3 where imaged. The sample of zero mineral concentration represents the matrix without hydroxyapatite. Twenty-four slices (i.e., 864 μm of sample) were imaged for each phantom at each voltage source (45, 55, 70 kV) in the middle region of the phantom. Average attenuation was calculated for each sample and a curve was plotted of mineral density (*MD*) versus the mean linear attenuation (μ), at each source voltage. Since the data follows a linear trend, the following equation was used to fit the data:

$$MD = m\mu + b \tag{3.16}$$

where m is the slope of the curve and b is the intercept of the *MD* axis. This equation was then used to convert linear-attenuation-coefficient data to *MD* data. Higher concentrations of hydroxyapatite-resin mixtures were not available to account for the high concentrations of minerals within the atherosclerotic calcifications. Therefore, it was assumed that the mineral density obeys equation (3.16) even when the density is high.

UWT LIBRARY

3.4. Conclusions

This chapter reviewed the basic theory and physics underlying each of the three different techniques—nanoindentation, FTIR, and CT—used by this study to characterize atherosclerotic calcifications and, in some cases, bone. Nanoindentation was used to measure nanomechanical properties; Fourier transform infrared spectroscopy (FTIR) was used to determine tissue composition; and micro-computed tomography (μCT), to reveal the distribution of mineral density. In addition, the main components of each testing apparatus were reviewed. Together, this information provides the basis for understanding how each technique was used in the tissue analysis performed in this thesis (see Chapters 4, 5 and 6).

UWT LIBRARY

3.5. References

Asif, S.; Wahl, K.; and Colton, R. 1999. Nanoindentation and contact stiffness measurement using force modulation with a capacitive load-displacement transducer. *Review of Scientific Instruments* 70(5): 2408-2413.

Bhushan, B. 1999. *Handbook of Micro/Nano Tribology*. Boca Raton: CRC Press.

Bikle, D. et al. 2001. The skeletal structure of insulin-like growth factor I-deficient mice. *Journal of Bone and Mineral Research* 16(12): 2320-2329.

Boskey, A. L. et al. 1992. Applications of Fourier-transform infrared (FTIR) microscopy to the study of mineralization in bone and cartilage. *Cells and Materials* 2(3): 209-220.

Boussinesq, J. 1885. *Applications des Potentiels à l'étude de l'équilibre et du Mouvement des Solides Élastiques*. Paris: Gauthier-Villars.

Ebenstein, D. 2002. Biomechanical characterization of atherosclerotic plaques: A combined nanoindentation and FTIR approach. Ph. D. dissertation. UCSF/UCB Bioengineering Graduate Group, University of California, San Francisco and University of California, Berkeley.

Ebenstein, D. M. et al. 2004. A nanoindentation technique for functional evaluation of cartilage repair tissue. *Journal of Materials Research* 19(1): 273-281.

Feldkamp, L.; Davis, L.; and Kress, J. 1984. Practical cone-Beam algorithm. *Journal of the Optical Society of America A: Optics Image Science and Vision* 1(6): 612-619.

Gadaleta, S. J. et al. 1996. Fourier transform infrared microscopy of calcified turkey leg tendon. *Calcified Tissue International* 58(1): 17-23.

Hallsworth, A.; Weatherell, J.; and Robinson, C. 1973. Loss of carbonate during first stages of enamel caries. *Caries Research* 7(4): 345-348.

Hara, T. et al. 2002. The influence of microcomputed tomography threshold variations on the assessment of structural and mechanical trabecular bone properties. *Bone* 31(1): 107-109.

Hendee, W. R. 1983. *The Physical Principles of Computed Tomography*. Boston: Little, Brown, and Company.

UMI LIBRARY

Hertz, H. 1896. On the contact of elastic solids. *Miscellaneous Papers*. New York: MacMillan & Co.

Hsu, H. et al. 2000. Isolation of calcifiable vesicles from aortas of rabbits fed with high cholesterol diets. *Atherosclerosis* 153(2): 337-348.

Hysitron. 2001. Triboindenter User Manual. Minneapolis, MN: Hysitron, Inc.

Jae-Young, R.; Tsui, T. Y.; and Pharr, G. M. 1997. Elastic properties of human cortical and trabecular lamellar bone measured by nanoindentation. *Biomaterials* 18(20): 1325-1330.

Klapperich, C.; Komvopoulos, K.; and Pruitt, L. 2001. Nanomechanical properties of polymers determined from nanoindentation experiments. *Journal of Tribology* 123(3): 624-631.

Leung, Y.; Walters, M.; and Legeros, R. 1990. Second derivative infrared spectra of hydroxyapatite. *Spectrochimica Acta Part A: Molecular and Biomolecular Spectroscopy* 46(10): 1453-1459.

Maddams, W. and Southon, M. 1982a. The measurement of derivative IR spectra , 3: The effect of bandwidth and band shape on resolution enhancement by derivative spectroscopy. *Spectrochimica Acta Part A: Molecular and Biomolecular Spectroscopy* 38(4): 459-466.

Maddams, W. and Tooke, P. 1982b. Quantitative conformational studies on polyvinyl-chloride. *Journal of Macromolecular Science: Chemistry* A17(6): 951-968.

Marshall, G. et al. 2001. Mechanical properties of the dentin-enamel junction: AFM studies of nanohardness, elastic modulus, and fracture. *Journal of Biomedical Materials Research* 54(1): 87-95.

Mulder, L.; Koolstra, J.; and Van Euden, T. 2004. Accuracy of microCT in the quantitative determination of the degree and distribution of mineralization in developing bone. *Acta Radiologica* 45(7): 769-777.

Nix, W. 1997. Elastic and plastic properties of thin films on substrates: nanoindentation techniques. *Materials Science & Engineering A: Structural Materials Properties Microstructure & Processing* 234-236: 37-44.

Nuzzo, S. et al. 2002. Quantification of the degree of mineralization of bone in three dimensions using synchrotron radiation microtomography. *Medical Physics* 29(11): 2672-2681.

UWF LIBRARY

Oliver, W. and Pharr, G. 1992. Improved technique for determining hardness and elastic modulus using load and displacement sensing indentation experiments. *Journal of Materials Research* 7(6): 1564-1580.

Pharr, G.; Oliver, W.; and Brotzen, F. 1992. On the generality of the relationship among contact stiffness, contact area, and elastic modulus during indentation. *Journal of Materials Research* 7(3): 613-617.

Ruegsegger, P.; Koller, B.; and Muller, R. 1996. A microtomographic system for the nondestructive evaluation of bone architecture. *Calcified Tissue International* 58(1): 24-29.

Seeram, E. 2001. *Computed Tomography: Physical Principles, Clinical Applications, and Quality Control.* Philadelphia: W.B. Sauders Company.

Smith, B. 1996. *Fundamentals of Fourier Transform Infrared Spectroscopy.* Boca Raton: CRC Press.

Smith, B. 1999. *Infrared Spectral Interpretation: A Systematic Approach.* Boca Raton: CRC Press.

Sneddon, I. N. 1965. The relation between load and penetration in the axisymmetric Boussinesq problem for a punch of arbitrary profile. *International Journal of Engineering Science* 3(1): 47-57.

Stilwell, N. A. and Tabor, D. 1961. Elastic recovery of conical indentations. *Proceedings of the Physical Society* 78(Part 2, 500): 169-179.

UWT LIBRARY

(a)

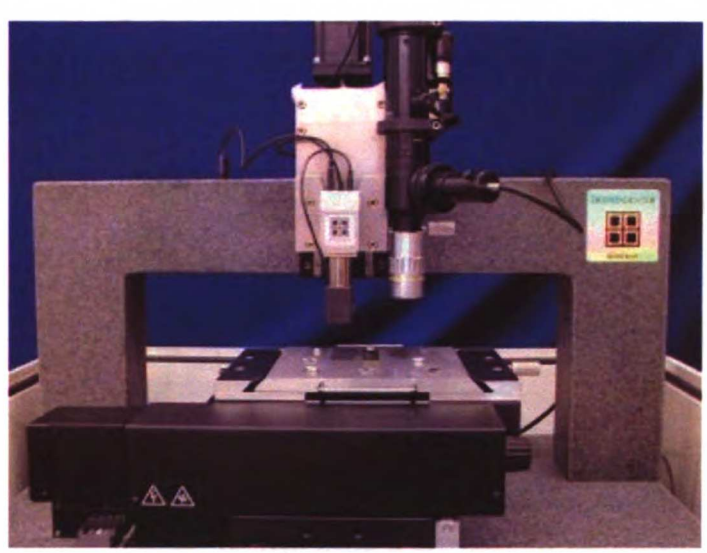

(b)

Figure 3.1: Nanoindenter instrumentation
(a) Triboindenter (Hysitron, Inc., Minneapolis, MN) used to performed roughness measurements and nanoindentations (b) Close-up of the main components of the Triboindenter (*Images courtesy of Hysitron, Inc.*)

UWJT LIBRARY

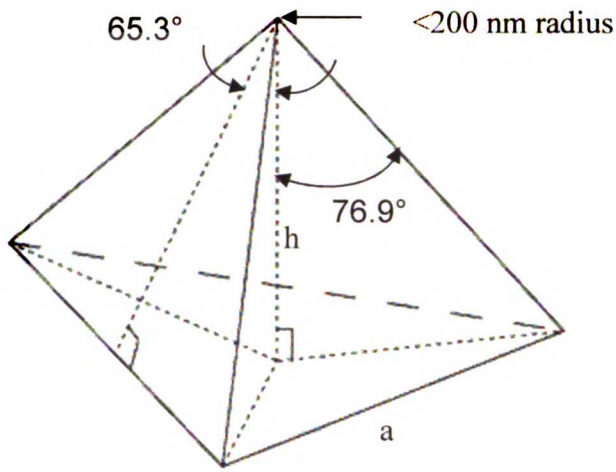

(a)

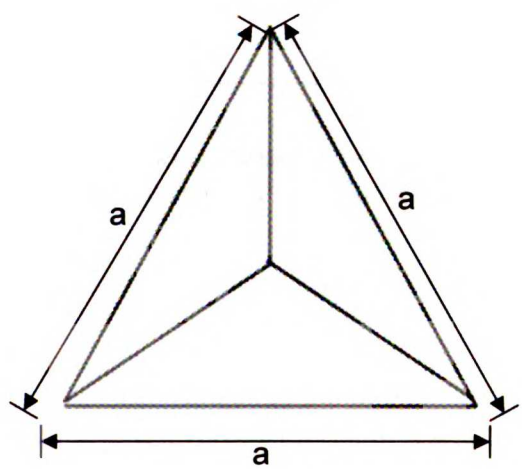

(b)

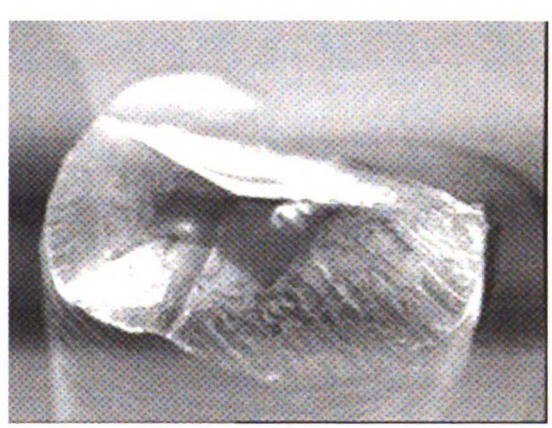

(c)

Figure 3.2: Berkovich tip
Information of the berkovich tip illustrating its (a) geometry and (b) shape of contact at depth *h* and a (c) photograph of intender tip (*Photograph courtesy of Hysitron, Inc.*)

UWI LIBRARY

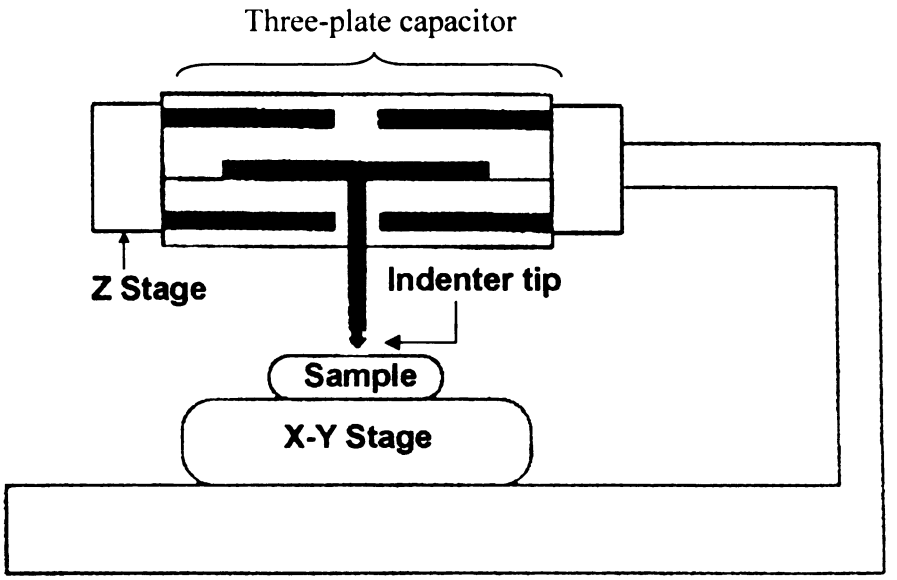

Figure 3.3: Hysitron's Triboindenter transducer
Three-plate capacitor force and displacement transducer (*Illustration courtesy of Hysitron, Inc.*)

UVJT LIBRARY

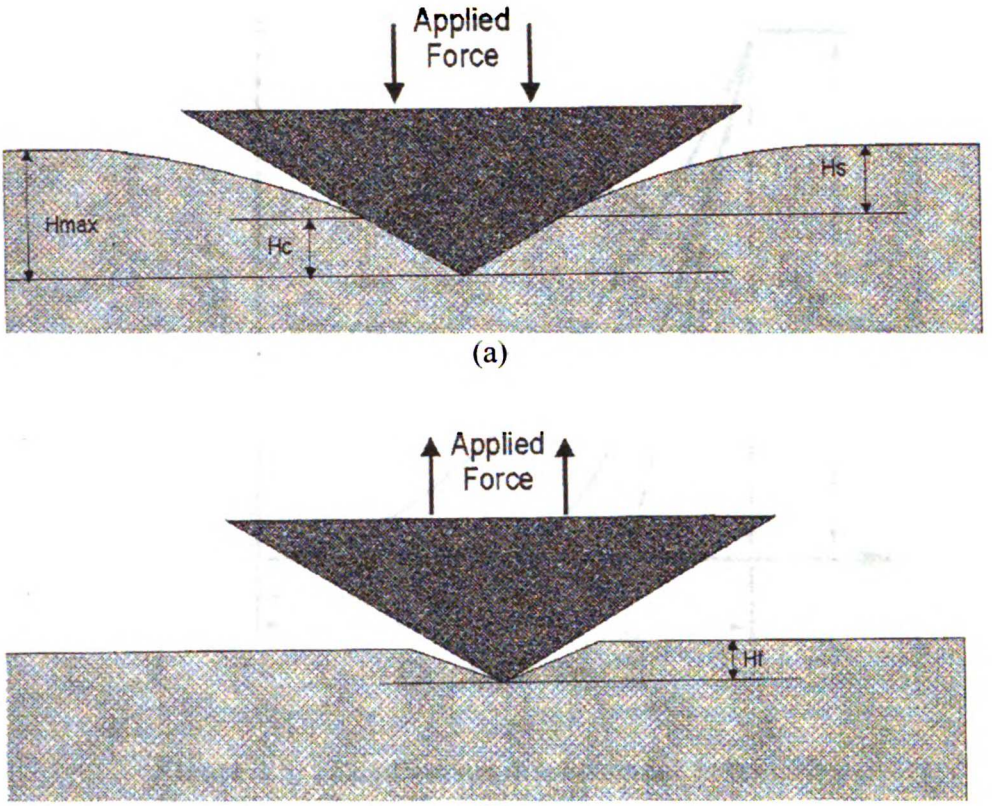

Figure 3.4: Schematic of the indentation process
Indentation (a) loading and (b) unloading where h_{max} is the maximum depth, h_c is the contact depth, and h_f is the final depth (*Images courtesy of Hysitron, Inc.*)

UMI Library

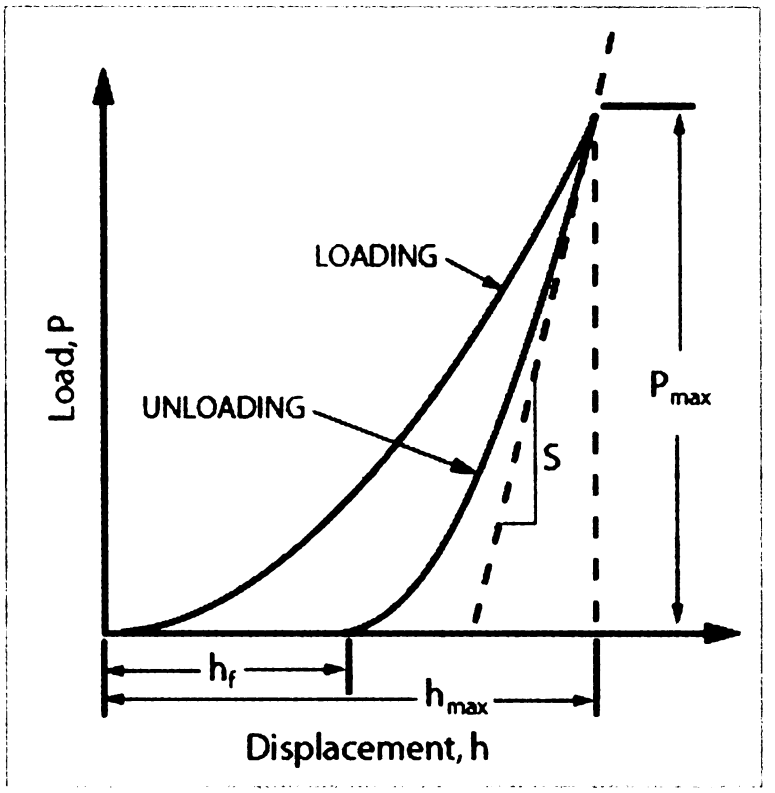

Figure 3.5: Load versus displacement indentation curve
(*Image courtesy of Hysitron, Inc.*)

UMI

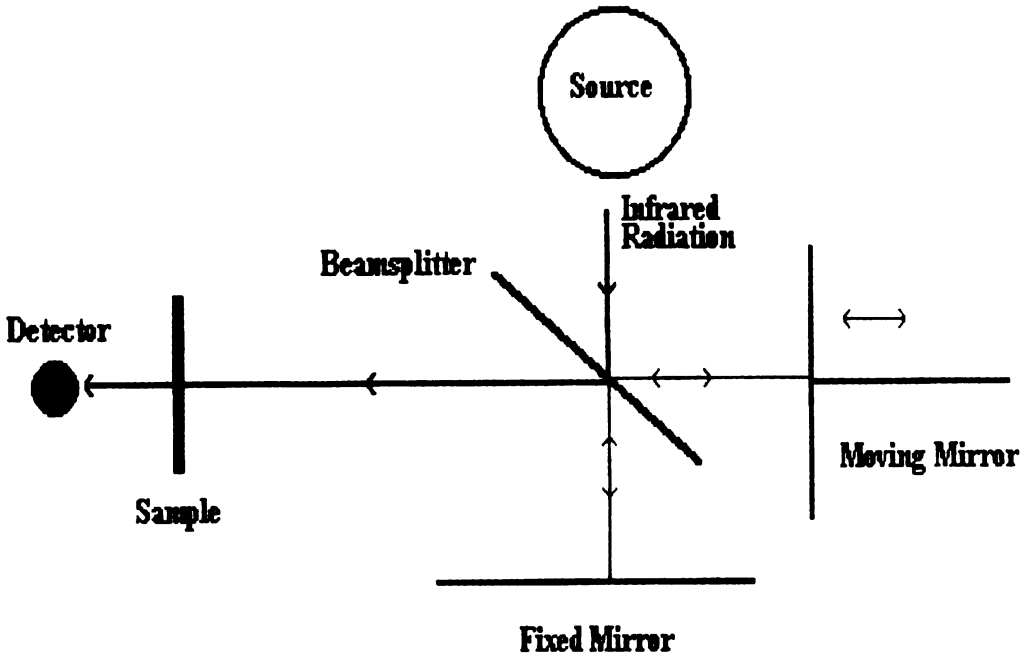

Figure 3.6: Schematic of the Michelson interferometer
(*Source: Smith 1996*)

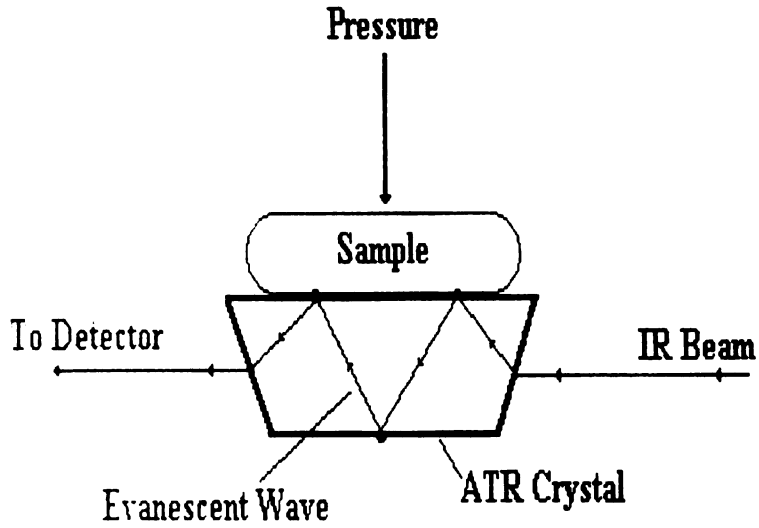

Figure 3.7: High refractive index crystal used in FTIR-ATR
Illustration of the high refractive index crystal of a FTIR-ATR system that causes an evanescent wave (*Source: Smith 1996*)

UWI LIBRARY

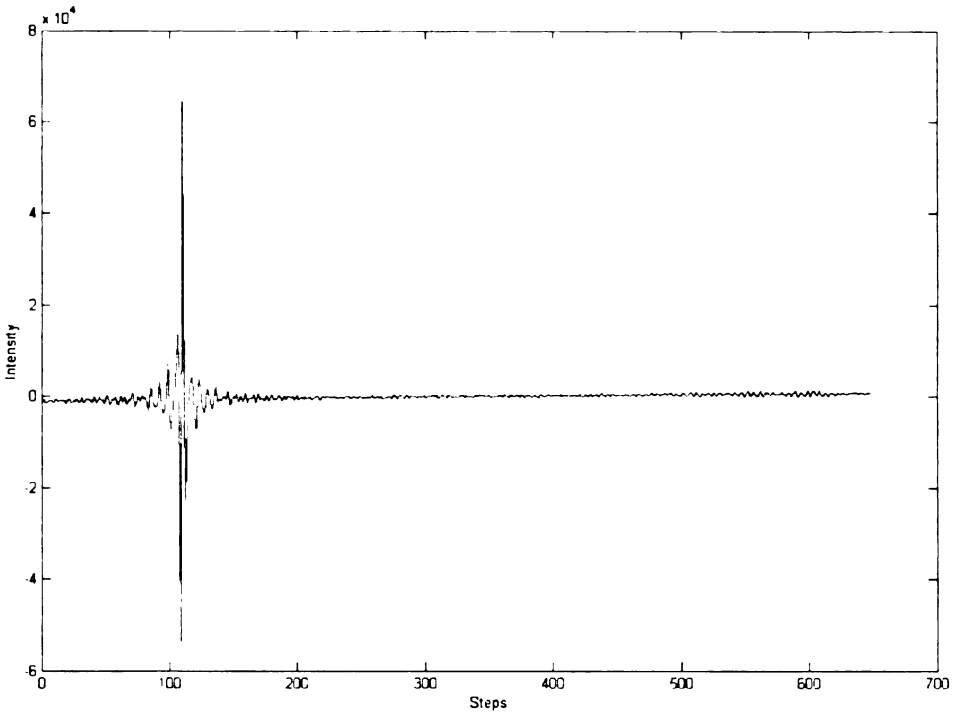

Figure 3.8: FTIR interferogram
Interferogram of an atherosclerotic calcification highlighting the centerburst

UWO LIBRARY

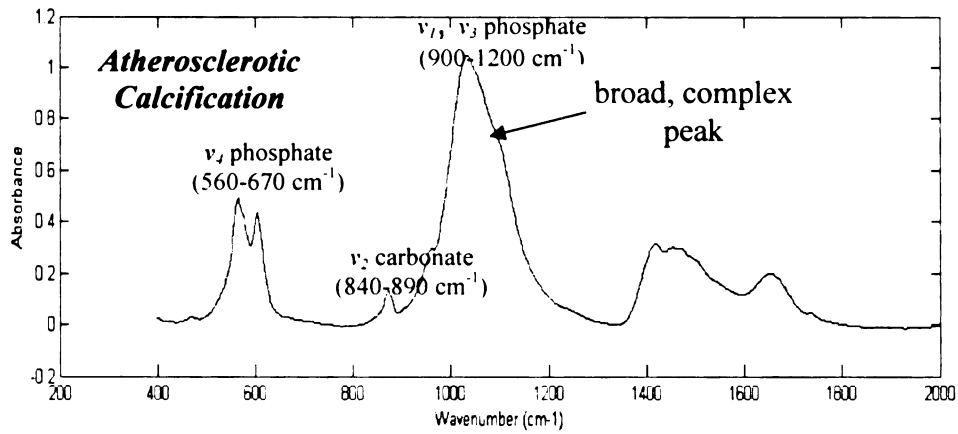

Figure 3.9: FTIR spectrum of an atherosclerotic calcification
FTIR spectrum of an atherosclerotic calcification with its respective compositional peaks

UWL LIBRARY

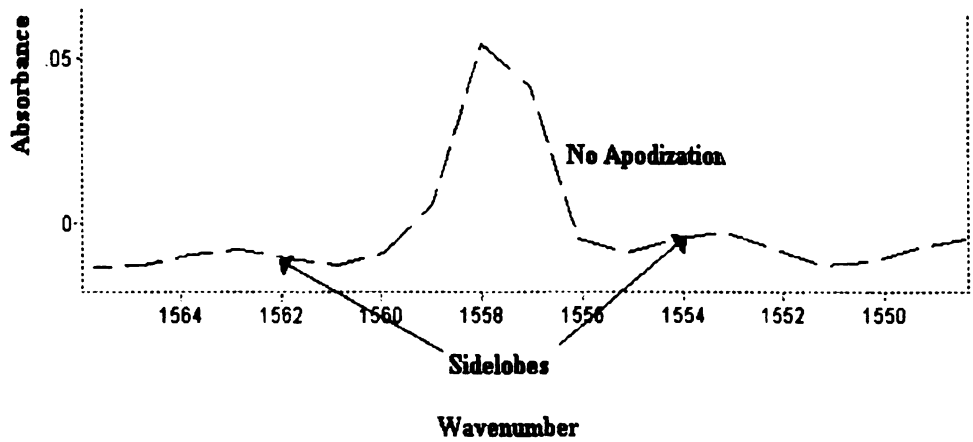

Figure 3.10: FTIR spectrum with side lobes
(*Adapted from Smith 1996*)

UWI LIBRARY

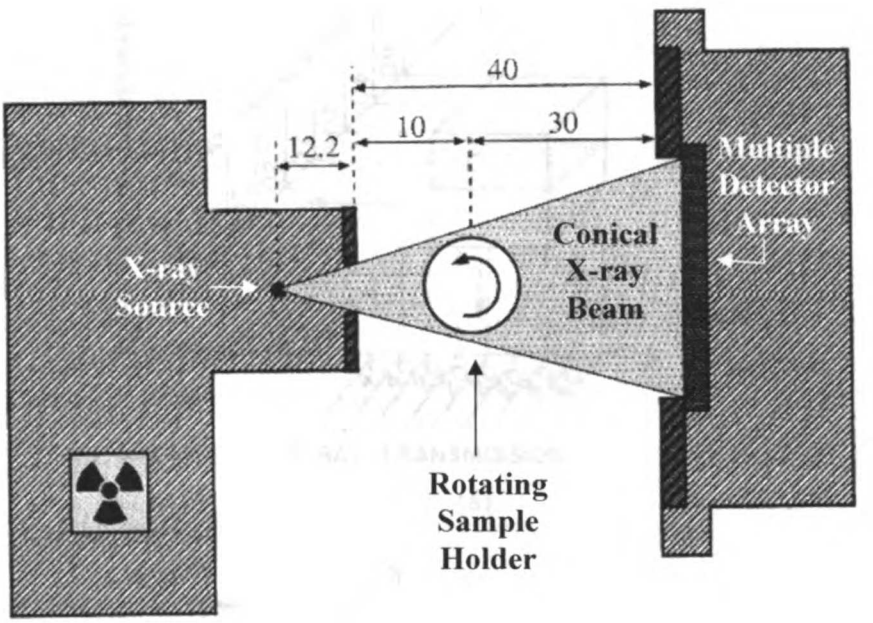

Figure 3.11: Schematic of the micro-computed tomography system
(*Adapted from Ruegsegger et al. 1996*)

UWI Library

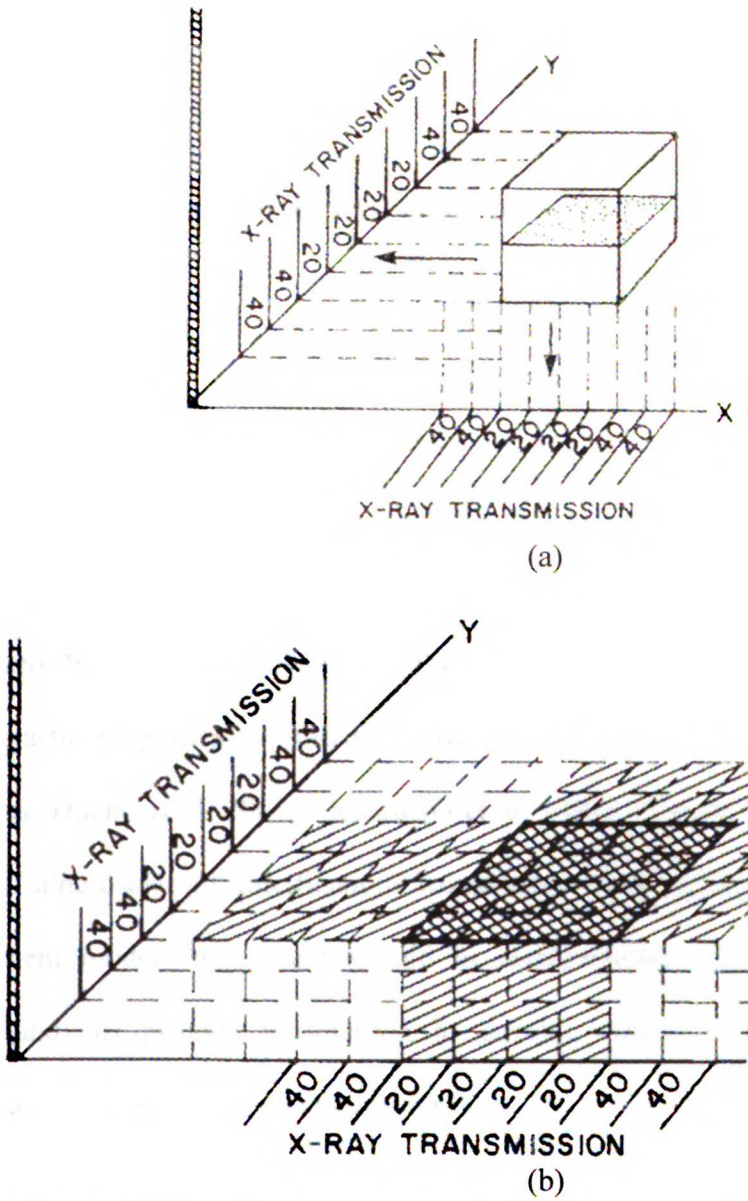

Figure 3.12: Computed tomography simple back-projection reconstruction
(a) Linear attenuation coefficients of x-rays transmitted through a section of a cube at two angles (b) Reconstructed image of the slice of the cube using simple back-projection of the two angles (*Source: Seeram 2001*)

Chapter 4

Nanomechanical Properties of Mineralized Tissue

4.0. Introduction

Despite the prevalence of atherosclerotic calcifications and their effects on the function (Fuessl et al. 2001; Park et al. 1993; Salunke et al. 2001) and treatments of diseased arteries (Fitzgerald et al. 1992; Nobuyoshi et al. 1991), few studies have characterized their mechanical behavior. Previous finite element models have arbitrarily assigned elastic properties to atherosclerotic calcifications or simply considered them rigid bodies (Huang et al. 2001; Richardson et al. 1989). Characterizing the mechanical behavior of atherosclerotic calcifications would allow the development of more realistic finite element models that could *(i)* aid in understanding why calcifications cause problems and *(ii)* provide information to develop better devices, operations, and pharmaceutical therapies to treat atherosclerosis.

Performing mechanical tests on atherosclerotic calcifications is challenging, primarily because these lesions are so small. Samples obtained in this study were typically about 2 mm wide, which is substantially smaller than the typical geometries needed for conventional mechanical tests. A novel technique for the testing of small-scale samples is nanoindentation. This technique was first developed for the mechanical characterization of thin films for the semiconductor industry (Doerner et al. 1986). Recently the use of nanoindentation has been extended to many other areas including

biomaterials and polymeric materials (Briscoe et al. 1998; Klapperich et al. 2001; Zhou et al. 2004). Additionally, nanoindentation has been successfully implemented in the mechanical characterization of biological tissues, including teeth, bone, cartilage, and even the constituents of plaque (Ebenstein 2002, Ebenstein et al. 2004, Jae-Young et al. 1997, Marshall et al. 2001).[10]

At this time, however, the information on atherosclerotic calcifications is quite limited and only one other study (from our lab) has reported nanoindentation results for these lesions. In this study, the atherosclerotic calcifications exhibited a broad range of reduced elastic moduli (0.18-21300 MPa) (Ebenstein 2002). This unpredictability may be attributed to surface roughness and/or the insufficient isolation of the calcifications. Atherosclerotic calcifications are usually partially or totally surrounded by fibrous tissue and if that surrounding tissue is not removed then the results may reflect the global properties of the tissue rather than the isolated properties of the calcification. This may explain the lower range of reduced elastic moduli (around 0.18 MPa), which is within the reported limits of the reduced elastic moduli for fibrous plaque tissue (0.06 MPa to 21.5 MPa) (Ebenstein 2002). Surface roughness may also have attributed to the spread in reduced elastic moduli observed by Ebenstein (2002) since the surface of the calcifications were tested in their native state and not prepared via polishing or microtoming. In general, however, nanoindentation requires testing depths be significantly greater than the surface roughness (Hoffler et al. 1997).

In addition to the issues of tissue isolation through proper dissection and minimal surface roughness through sample preparation, other parameters can play into the

[10] See Chapter 3 for more information about the theory and testing apparatus used in nanoindentation

mechanical response of these tissue constituents. For example, it is also important to minimize time-dependent effects such as creep during indentation. Creep may be identified in an indentation load versus displacement curve as the "nose" or protrusion occurring in the initial part of the unloading curve when a triangular load function is used (Figure 4.1) (Briscoe et al. 1998). This phenomenon occurs because, during initial unloading, the creep rate of the material is higher than the unloading rate of the indenter tip and, therefore, a slight increase in depth occurs during the initial unloading. Since nanoindentation theory assumes that the initial portion of the unloading curve is elastic, it is important to minimize the effects of creep. This can be achieved by inserting a hold segment into the load function (at constant maximum load) between the loading and unloading segments (Figure 4.2) (Briscoe et al. 1998). It is therefore important to know how long a hold time is necessary to eliminate the "nose" in the unloading curve.

Loading/unloading rates may also affect time-dependent mechanical behavior (Klapperich et al. 2001). Evidence suggests that, in bone, this behavior may be attributed to the viscoelasticity of its matrix (Fois et al. 2001) and/or the accumulation of damage within the material (Fondrk et al. 1988). Since both bone and atherosclerotic calcifications are mainly hydroxyapatite-matrix composites with high mineral content, atherosclerotic calcifications may experience similar time-dependent mechanical behavior to bone. Considering this possibility, it is important to determine if loading/unloading rates affect the measurement of the elastic properties of atherosclerotic calcifications.

The goal of this study was to determine the reduced elastic moduli of atherosclerotic calcifications while accounting for surface roughness, tissue isolation, and

time-dependent mechanical behavior. To ensure adequate isolation, careful microdissection of atherosclerotic calcifications was performed under a microscope. The calcifications were also microtomed to obtain a smooth surface. Indents were performed at different loads to determine the effects of roughness on the apparent reduced elastic moduli measured at different indentation depths. In addition, several hold times and loading/unloading rates were tested to determine their effects on reduced elastic moduli. These systematic studies assisted in determining appropriate testing parameters to measure the reduced elastic moduli of atherosclerotic calcifications.

By decreasing potential variations caused by roughness, insufficient isolation, and time-dependent mechanical behavior, this research also aims to identify compositional factors that correlate with the variations in the elastic properties of atherosclerotic calcifications. The hypothesis is that, as with other mineralized tissues like bone and teeth, the elastic properties of the calcifications increase with increasing mineral content (Currey 1988; Gupta et al. 2005; Tesch et al. 2001). Previous work in dentin, bone, and plaque has shown that Fourier transform infrared spectroscopy (FTIR) can be used to qualitatively determine mineral content by calculating the mineral-to-matrix content ratio (Li et al. 2003; Paschalis et al. 1997; Tesch et al. 2001).[11] In this study, nanoindentation is used to measure the elastic properties of the atherosclerotic calcifications and trabecular bone and Fourier transform infrared spectroscopy in attenuated total reflectance mode (FTIR-ATR) is used to characterize their composition. Trabecular bone was used as a control material since it is also a hydroxyapatite-dominated mineralized

[11] See Chapter 3 for more information about FTIR theory and testing apparatus

tissue and has been extensively studied by both nanoindentation and FTIR (Paschalis et al. 1997; Roy et al. 1999).

4.1. Materials and Methods

To more accurately measure the reduced elastic moduli in atherosclerotic calcifications, three experiments were conducted first to determine the appropriate nanoindentation testing parameters. Since nanoindentation requires that testing depths be significantly greater than the surface topography, the first experiment was designed to determine what depths of penetration were appropriate for the roughness achieved by microtoming (Hoffler et al. 1997). For this, different regions of the microtomed surface were randomly measured for roughness and then indented to different depths. The coefficient of variance (COV) was used to determine the extent of variability of the measured reduced elastic modulus and the ratio of maximum depth (h_{max}) to root-mean-square (rms) roughness (i.e., h_{max}/(rms roughness)) was calculated to ascertain at what ratios would roughness not affect the measurement of reduced elastic modulus.

The subsequent two experiments were intended to aid in selecting an appropriate trapezoidal load function for measuring the reduced elastic moduli of atherosclerotic calcifications and bone. Different hold times were tested to determine the time required to eliminate the effect of creep that manifests itself as the "nose" in the unloading load versus displacement curve. In addition, different hold times and loading/unloading rates were tested to determine if they cause time-dependent behavior that may effects the measurements of the reduced elastic modulus. This data aided in selecting the appropriate load function that would minimize time-dependent effects.

Once the appropriate trapezoidal load function was selected, nanoindentation was used to measure the reduced elastic moduli of atherosclerotic calcifications and bone. FTIR was then used to determine qualitative measurements of mineral content by determining the mineral-to-matrix ratios of those same specimens. The mineral-to-matrix ratios and reduced elastic moduli were analyzed to check for a correlation between the two.

4.1.1. Sample Preparation

Three human carotid plaques from three patients over 50 years old were provided by vascular surgeons from the San Francisco Veteran Affairs Medical Center. The plaques were obtained from routine endarterectomy procedures in which they were excised *en bloc* and imaged *ex vivo* using magnetic resonance imaging (MRI) by staff from the Veteran Affairs Medical Center. MRI was used to screen for the presence of calcifications and aid in the dissection of the plaque specimens. In this imaging modality, calcifications and thrombosis appear black while other tissues are different shades of gray (Figure 4.3). Heavily calcified plaques are also very stiff. Plaques that felt stiff and had MR images containing black regions were classified as "calcified plaques".

Once imaged, the samples were fixed in 10% buffered formalin at room temperature. They were then stored at 5°C until the calcified regions were microdissected from the rest of the plaque. Microdissection was done under a dissecting microscope and all visible fibrous or fatty tissue was removed with tweezers. The three plaques were labeled A, B, and C and the calcifications from these plaques were labeled numerically. For example, calcification A6 would be a calcification from plaque A.

For comparison, four pieces of trabecular bone samples were cored out of the lumbar bones of four human cadavers, all of which were over 50 years old. They were formalin-fixed and stored under the same conditions as the calcifications. The bones were labeled A through D. To remove the marrow, the trabecular bone cores were cleaned with a water jet, placed in an ultrasonicator (30 minutes, 1% Tergazyme detergent[12]), and rinsed again with a water jet. The calcifications and bones were then dehydrated and embedded in polymethylmethacrylate (PMMA) (Appendix A). This embedding process was chosen mainly because it causes minimal infiltration (less than 70 μm) into the tissue as seen by Fourier transform infrared spectroscopy image (Figure 4.4). Infiltration was characterized by the appearance of the ~ 1729 cm^{-1} peak in the calcifications spectrum; this peak does not exist in the atherosclerotic calcifications and is characteristic of PMMA. Minimal infiltration is critical since the study intended to measure the material properties of only the calcification and not the calcification-PMMA composite. Once the PMMA had polymerized, the samples were microtomed using a Leica RM2255 microtome (Leica Microsystems, Germany) with a carbide tungsten blade to produce a smooth surface for nanoindentation.

UMI

4.1.2. Roughness

At least 16 measurements of roughness were taken randomly on each microtomed region of three calcifications (each obtained from a different plaque specimen) and one bone sample using a TriboIndenter (Hysitron, Inc. Minneapolis, MN) with a Berkovich tip. Roughness measurements (rms roughness) were taken within a square area of 5 μm x

[12] An enzymatic cleaner made by Alconox Inc. (White Plains, New York)

5 μm at a scan rate of 0.8 Hz and a load of 1 μN. One-way analysis of variance was performed on the average roughness of the samples.

After measuring the roughness, indents were done on the *same* area using the *same* equipment, a TriboIndenter. The indents were done using a trapezoidal load function with a 400 μN/s loading and unloading rate to a maximum load of 700, 2800, and 4400 μN with a 10 s hold in between. The range of loads was chosen to ensure depths between 100 nm and 600 nm. All indents were spaced at least 100 μm from each other and at least 100 μm from the edge for the calcifications. This spacing is considered appropriate since the surrounding material affected by the load is expected to lie within a 6 μm diameter circle from the indenter tip (i.e., diameter about 10 times the indent depth) (Hoffler et al. 1997). Ten indents were performed for each load in each sample. The reduced elastic modulus for each indent was determined from the unloading curve using the method of Oliver and Pharr (1992). For each indent, the ratio of maximum depth-to-rms roughness was also calculated by dividing the maximum depth of each indent by the rms roughness in the region indented. The reduced elastic moduli and maximum depths were grouped by their ratio within each calcification. There were at least five data points for each set of ratios; the others had to be discarded because of thermal drift or other artifacts that did not allow for the proper calculation of the reduced elastic modulus. One-way analysis of variance with Tukey post test (for comparison) were performed on the reduced elastic moduli of those calcifications that had more than two groups and a two-tailed unpaired t-tests was performed on the reduced elastic moduli of the two groups of calcification A2. Comparisons of the reduced elastic moduli were not made between calcifications because, due to the natural heterogeneity between samples, the elastic

UNLV THESIS

properties can vary from sample to sample. The COV for each group of ratios was also calculated and analyzed to determine if there were any trends.

4.1.3. Hold Time Segments and Loading/Unloading Rates

For the experiments that varied the length of the hold time and the loading/unloading rates, indents were again made with a TriboIndenter and Berkovich tip. The indents were spaced at least 20 μm apart and at least 70 μm for the edge. All specimens were loaded with a trapezoidal loading curve with equal loading and unloading rates and a hold in between. The hold times tested were 5, 10, 25, 50, 75, 100, and 125s at 550 μN/s loading and unloading rate (the median loading rate tested). The loading rates tested were 100, 250, 400, 550, 700, 850, and 1000 μN/s with a 50 s hold (closest to the average hold time tested). The sets of loading rates and hold times were conducted randomly on three calcifications, each taken from a different plaque. The indents were kept close to each other to minimize the variability that exists because of the heterogeneity of the specimens (Figure 4.5). Twelve indents were performed for each load function. The reduced elastic modulus for each indent was determined from the unloading curve using the method of Oliver and Pharr (1992). There were at least five data points for each load function; the others had to be discarded because of thermal drift or other artifacts that did not allow for the proper calculation of the reduced elastic modulus. ANOVA analysis with Tukey-Kramer multiple comparison post tests were conducted amongst the reduced elastic moduli measured using the different hold times and loading/unloading rates; each load function tested had at least five data points.

UMI

4.1.4. Nanoindentation of Atherosclerotic Calcifications and Bone

A TriboIndenter with a Berkovich tip was also used for the experiments comparing the nanomechanical properties of atherosclerotic calcifications and trabecular bone samples. Five calcifications were tested (three calcifications from one plaque [A1, A6, and A7] and one calcification from each of the two other plaques [B5 and C3]) and four bone samples from different cadavers (bones A, B, C, and D). Indents were spaced at least 50 μm apart and at least 70 μm from the edge in the calcifications and 35 μm from the edge in trabecular bone. The indentations in trabecular bone had to be closer to the edge since the width of the trabecular bone ranges from 50 to 450 μm (Gibson 1985). The bone samples were microtomed and indents were made on exposed trabeculae in the bone specimens. Each sample had at least 35 indents that allowed for the proper calculation of the reduced elastic modulus. Specimens were loaded with the trapezoidal loading curve shown in Figure 4.2 (400 μN/s loading and unloading rate, 10 s hold time). These parameters were chosen after analyzing the results of the previous test (Section 4.1.3). A more detailed explanation of the parameter selection follows in the discussion below (Section 4.2.1-4.2.3). The reduced elastic moduli of the calcifications and bone were determined from the indentation unloading curves using the method of Oliver and Pharr (1992). Nonparametric (Kruskal-Wallis) ANOVA tests with Dunn's multiple comparison tests were used since calcification A1 did not pass the normality test using the Kolmogorv and Smirnov method and the others had standard deviations that were not considered significantly the same as found by the Bartlett test.

UMI

4.1.5. FTIR-ATR of Atherosclerotic Calcifications and Bone

Five FTIR-ATR spectra were taken for each calcification and bone sample with a mid-infrared interferometer: 256 scans, 4 cm^{-1} spectral resolution. The interferogram were apodized with a Happ-Genzel function and Fourier transformed. To remove the PMMA signal from the spectrum of each sample, a spectrum was taken of the pure PMMA from each sample. This spectrum was then subtracted from the spectrum of the embedded calcification.

The subtracted spectrum was used to measure the mineral-to-matrix ratio. The mineral content was calculated by baselining the phosphate region (approximately 900 cm^{-1} to 1200 cm^{-1}) and then integrating the area under this region. Similarly, the matrix was calculated using the amide I region (approximately 1600 cm^{-1} to 1690 cm^{-1}). Then the area under the phosphate peak was divided by the area under the amide I peak to obtain the mineral-to-matrix ratio. One-way analyses of variance with Tukey post tests (for comparison) were conducted between the mineral-to-matrix ratios of the samples. In addition, statistical analysis was performed to determine if the reduced elastic moduli correlated with the mineral-to-matrix ratios.

4.2. Results and Discussion

4.2.1. Roughness

The average roughness of all three calcifications is 81 ± 45 nm and the average roughness of the bone sample is 96 ± 36 nm (Figure 4.6). The difference between the roughness of the samples, including the bone, is not statistically significant ($p<0.05$)

except that calcification B3 is significantly less rough than the bone and calcification C2. This suggests that the microtoming process is fairly consistent in attaining average rms roughnesses at or less than 100 nm.

Donnelly et al. (2004) found that the coefficient of variability of the reduced elastic modulus of bone was substantially decreased when contact depths-to-rms roughness ratios were greater than three. Since the average bone roughness is 96 nm and the minimum contact depths for all bone studies is 425 nm then, according to that study, the penetration depths in the present study should minimize the variability in the reduced elastic moduli. Similarly, the average calcification roughness is 81 nm and the minimum contact depth for all the calcifications was 221 nm, which gives a minimum contact depth-to-rms roughness ratio of 2.7. Assuming that the roughness of atherosclerotic calcifications affect the reduced elastic modulus in the same way, the indent depths used in the present study should be sufficient to minimize errors due to roughness.

The average, standard deviations, and coefficients of variance (COV) of reduced elastic moduli for the different ranges of h_{max}-to-rms roughness ratios are shown in Table 4.1.[13] Only those ratios that have at least five data points for each range are included in Table 4.1 and the statistical analysis. Since the roughness should have less affect on the reduced elastic modulus the further the indenter penetrates the sample, the variance should decrease with increasing h_{max}-to-rms roughness. However, calcifications A2 and B3 have increasing COV (~ + 0.18 and ~ + 0.03, respectively) with increasing ratio, whereas C2 shows a decrease in COV (~ -0.05). Comparing the COV of the grouped

[13] Maximum depths were used instead of contact depths because contact depth is dependent of stiffness, which is used to calculate reduced elastic modulus, while h_{max} is independent of both. This does not affect the comparisons analyzed in this section.

reduced elastic moduli in ratios 3 to 4 of all the calcifications reveals that calcification B3, which has the smoothest surface (average of 55.6 nm), has the smallest COV, i.e., 0.21. However, calcification A2 is on average smoother than calcification C2 (average difference of 21 nm) and yet, at ratios 3 to 4, its reduced elastic modulus has a higher variance. Donnelly et al.'s study compared the effects of roughness on the reduced elastic modulus of two samples with a difference in average roughness of 20 nm and this revealed an improved variability with the smoother sample.

In addition, statistical analysis revealed that the ratio of h_{max}-to-rms roughness has no apparent effect on the reduced elastic moduli of calcification A2 or C2, even though C2 is the roughest. There are significant differences between the grouped reduced elastic moduli of calcification B3, with the reduced elastic modulus decreasing for higher h_{max}-to-rms roughness ratios. However, the two groups that are compared in specimen B3 have very different maximum depth-to-roughness ratios (3 to 4 and 8 to 9). Further statistical analysis reveals that the group of ratios 3 to 4 consists of much lower maximum depths (195 ± 87 nm) than the group of ratios 8 to 9 (505 ± 109 nm) ($p < 0.001$) (Table 4.2). The observed decrease in reduced elastic modulus with increase in penetration depth in calcification B3 may therefore be attributed to a trend of decreasing reduced elastic moduli with increasing penetration depth, which was observed in all the samples (Figure 4.7).[14] Though the maximum depths of groups 1 to 2 and 5 to 6 of calcification A2 are significantly different ($p < 0.01$), their difference is much less than the two groups of calcification B3 (145 nm vs. 310 nm) (Table 4.2). This may explain

[14] Hypotheses for this trend are explained later in Section 4.2.1.

why calcification A2 does not have significant differences in the reduced elastic moduli of the three groups.

In general, it is not clear whether further smoothening would decrease the effects of roughness on the reduced elastic modulus. It also appears from this study that the difference in h_{max}-to-rms roughness ratios does not have a consistent effect on reduced elastic modulus. However, further studies should be done to obtain more data at different ratios to verify this. In conclusion, to avoid shallow depth penetrations and effects of roughness, a maximum load of 4000 μN was used to calculate the reduced elastic moduli of atherosclerotic calcifications and bone.

Indenter tip cannot measure roughness less than its radius of curvature. Since the tip used in the present study is a Berkovich tip which has a radius of curvature around 100 nm to 200 nm, then the surface of the samples may, in reality, be rougher since the tips would not be able to image smaller asperities. This would mean that the ratios might be lower than what was calculated in this study. This may affect the results obtained in this section; therefore more precise roughness measurements should be taken (e.g., using atomic force microscopy (AFM)) to more accurately determine roughness effects on nanomechanical properties.

4.2.2. Hold Times and Loading/Unloading Rates

Table 4.3 presents the average values and standard deviations of the reduced elastic moduli for three calcifications at hold times ranging from 5 seconds to 125 seconds. Maximum depths are in the range of 450 nm to 650 nm. Only those datasets that have at least five indents for each hold time are included in the figures and the statistical

analysis. Since the different lengths of the hold time do not statistically alter the measured reduced elastic moduli, a hold segment of 10 seconds was chosen for subsequent testing, as is common practice for indentation testing of bone (Rho et al. 1999; Roy et al. 1999). It was found to be sufficient to allow creep to dissipate prior to unloading as observed by the elimination of the "nose" in the unloading curve (Figure 4.1).

Table 4.4 summarizes the average reduced elastic moduli and the standard deviations for three calcifications at different loading/unloading rates tested (100 μN/s to 1000 μN/s). Maximum depths fell in the range of 350 nm to 550 nm. The reduced elastic moduli of calcification B3 and C2 do not show significant differences in the modulus as a function of loading/unloading rates (Table 4.4). Calcification A5, on the other hand, displays significant differences in reduced elastic moduli between the two loading/unloading rate extremes. The reduced elastic modulus at 100 μN/s (32.1 ± 5.1 GPa) is less than that at 850 μN/s (41.1 ± 4.2 GPa) and 1000 μN/s (42.7 ± 6.5 GPa). Moreover, the reduced elastic modulus at 250 μN/s (35.6 ± 3.2 GPa) is less than that at 1000 μN/s (Table 4.4). These significant differences between the extreme loading/unloading rates may be partially attributed to thermal drift experienced during testing because of the long duration of the tests at low loading/unloading rates. This thermal drift is sometimes observed in the load versus displacement curve as the crossover in the loading and unloading curves in some of the tests, especially at 100 μN/s. Since this study resulted in no clear dependence of indentation modulus on loading rate, except at low rates, a midrange loading/unloading rate of 400 μN/s was used for subsequent tests.

UMI

4.2.3. Atherosclerotic Calcifications and Bone

The plot of reduced elastic modulus versus maximum depth reveals that the nanomechanical properties of atherosclerotic calcifications and bone follow similar trends when tested with the same load function: the reduced elastic moduli versus maximum depth data overlap in the depth range of 550 nm to 650 nm, with both sets of data showing a decrease in reduced elastic modulus with an increase in maximum depth (Figure 4.7). The main difference occurs in the distribution of elastic moduli with respect to maximum depth. As seen in Figure 4.7, bone has more data points at maximum depths greater than 550 nm. This would explain why the average reduced elastic moduli of the bone samples (9.6 GPa to 11.2 GPa) are all less than those of the atherosclerotic calcifications (14.8 GPa to 25.7 GPa) (Table 4.5). This relationship is significantly different in all cases. In addition, the reduced elastic modulus of calcification A6 is the lowest (14.8 ± 3.4 GPa) and is statistically different from the four other calcifications. Though calcifications A1, A6, and A7 are from the same plaque, the reduced elastic modulus of A6 differs statistically from the other two. Calcification C3 has the highest reduced elastic modulus (25.7 ± 8.1 GPa) and is also statistically different from samples B4 and A7.

Since the bone samples were provided by another lab, it was not clear in what direction the samples were cored. This is important because bone has been shown to exhibit anisotropic behavior even at the microstructural level and this can be detected by nanoindentation (Rho et al. 1999; Roy et al. 1999; Swadener et al. 2001). The reduced elastic modulus of dehydrated, embedded trabecular lumbar bone measured by nanoindentation has ranged from 14.5 ± 2.2 GPa to 24.4 ± 3.4 GPa (Rho et al. 1997; Roy

et al. 1999). Assuming, as in both of these studies, that the bone in this study is also homogeneous, isotropic and has a Poisson's ratio of 0.3, the elastic modulus, E, of these bones were converted back to reduced elastic modulus, Er, with the following formula (Stilwell et al. 1961):

$$\frac{1}{E_r} = \frac{1-\nu^2}{E} + \frac{1-\nu_i^2}{E_i} \tag{4.1}$$

where ν is the Poisson's ratio of bone, ν_i is the Poisson's ratio of the indenter (equal to 0.07), and E_i is the reduced elastic modulus of the indenter (equal to 1140 GPa). The calculations reveal that the reduced elastic moduli of bone A through D fall within one standard deviation of the lower end of the reported data. That our data for the bone samples is in agreement with that of other studies suggests the measurements of reduced elastic modulus of atherosclerotic calcifications may also be compared to bone data in the literature.

On average, trabecular bone is composed of about 70% mineral by dry weight; cortical bone, about 75%; and atherosclerotic calcification, about 78% (Gong et al. 1964; Herring 1977; Schmid et al. 1980). From literature, it is apparent that the atherosclerotic calcifications in this study have nanomechanical properties similar to both trabecular and cortical bone (Rho et al. 1999; Rho et al. 1997; Roy et al. 1999). The reduced elastic properties of the atherosclerotic calcifications range from 14.8 GPa to 25.6 GPa; those of dehydrated and PMMA embedded trabecular bone (in literature), from 14.5 GPa to 24.4 GPa; and those of dehydrated and PMMA embedded cortical bone (in literature), from 18.0 GPa to 27.7 GPa (Rho et al. 1999; Rho et al. 1997; Roy et al. 1999).[15] Bone's

[15] The reduced elastic moduli of bone were calculated from elastic moduli using equation (4.1) and making the same assumptions about Poisson's ratio and elastic moduli as above.

elastic modulus has been found to be anisotropic and also vary by tissue type, anatomical location, and age (Hoffler et al. 2000; Roy et al. 1999; Zysset et al. 1999). Since the range of the reduced elastic moduli of atherosclerotic calcifications is within those of cortical and trabecular bone, this suggests that calcifications may also exhibit some level of anisotropy perhaps due to local differences in mineral content. The most striking difference is the variation in the properties of the three calcifications in plaque A. This suggests that variations may also exist due to anatomical location within the plaque.

In general, the trend of decreasing reduced elastic modulus with increasing depth may occur because, under the same maximum load, stiffer materials will not allow as much tip penetration as materials that are more compliant. Since, in bone, mineral has been attributed to causing stiffer bone (Currey 1988; Gupta et al. 2005) and trabecular bone has less mineral than that reported for atherosclerotic calcifications, then the trabecular bone may be more compliant. This hypothesis explains why, in general, bone experiences deeper indents than atherosclerotic calcifications while under the same maximum load, thus explaining the trend.

The mineral-to-matrix ratios of the calcifications from this study are given with the corresponding reduced elastic moduli in Table 4.5. Calcification A1 and Bone B were omitted because their spectra were too noisy. Unlike what is recommended, their signal was not three times stronger than the noise (Smith 1996). Using FTIR-ATR, Ebenstein (2002) also measured the mineral-to-matrix ratios of three formalin-fixed calcifications; they ranged from 7.1 to 14.1. Although the mineral-to-matrix ratio of calcification A6 is the only sample falling within the range of ratios determined by Ebenstein (2002), our experimental process is still validated because Ebenstein only measured three samples,

which is not a representative sampling. The mineral-to-matrix ratios of the atherosclerotic calcification, on average, are higher than the ratios of the bone samples. The exception is calcification A6, having a mineral-to-matrix ratio of 9.3, which is in the same range as the trabecular bone samples (averages 8.2 – 12.8). And, Bone D is statistically higher than Bone A. As with the reduced elastic moduli, the mineral-to-matrix ratios of A6 and A7 are different even though they are from two calcified regions in the *same* plaque. In addition, calcification C3 has the highest average mineral-to-matrix ratio of all the calcifications and bone samples for which spectroscopic data was obtained although it is not statistically different from B4 or A7.

From the graphs in Paschalis et al.'s studies, mineral-to-matrix average ratios for bone appear to range from about 3.4 ± 1.3 to 6.5 ± 1.4 for trabecular bone and 2.8 ± 1.3 to 5.0 ± 1.2 for cortical bone (Paschalis et al. 1997; Paschalis et al. 1996). The slightly higher bone mineral-to-matrix ratios in our study (8.2 – 12.8) may be attributed to differences in the experimental process as compared to Paschalis et al. Both of their studies were conducted under transmission mode in barium fluoride windows while the present study used FTIR in attenuated total reflectance mode. The main difference, however, may be because Paschalis et al. also decalcified their samples and subtracted contributions of the collagen signal that occurs in the phosphate 900 cm^{-1} to 1200 cm^{-1} region (Paschalis et al. 1997). This would decrease the phosphate peak and cause lower mineral-to-matrix ratios.

Using the Pearson r correlation test on the average reduced elastic moduli and mineral-to-matrix ratios of bone and atherosclerotic calcifications in the present study suggests that there is a linear correlation between the two ($R^2 = 0.88$ and two-tailed $p <$

0.005); the average reduced elastic modulus increases with increasing mineral-to-matrix ratios. However, the standard deviation for the atherosclerotic calcifications is very large so the correlation cannot be stated with absolute certainty. The large standard deviation is attributed to the increased effect of noise on atherosclerotic calcifications. Since the amide I peaks in atherosclerotic calcifications are so small, noise affects the signal a lot more. In general, as observed in this study, the signal in attenuated total reflectance (ATR) mode is noisier than in transmission. This may be because the interface between the specimen and the crystal has to be in direct contact in ATR mode while, in transmission mode, the signal is simply transmitted through the sample. Although the specimens were microtomed and clamped onto the crystal's face, this did not guarantee uniform direct contact because the sample might not lay uniformly flat on the crystal thus leaving air gaps between the two. In addition, errors may have occurred while subtracting the PMMA because it is difficult to completely subtract out the PMMA from the embedded calcification. All these effects may cause an increase in noise.

Considering these issues, what can be said with certainty is that the bone samples and calcification A6 have both mineral-to-matrix and reduced elastic moduli less than the other calcifications, thus suggesting a trend of a lower reduced elastic modulus with lower mineral-to-matrix ratio. Since the mineral-to-matrix ratio is correlated to ash weight divided by dry tissue weight and thus, to mineral content (Boskey et al. 1992), then the existence of the trend supports other studies that found increasing elastic moduli with increasing mineral content (Currey 1988; Gupta et al. 2005).

The study's limitations should be considered. The nanoindentation and FTIR data both were averaged data taken from only one plane of each calcification. Therefore, it is

not certain whether the whole calcification A6 is less mineralized than the other calcifications (even those from within the same plaque) or whether only the tested region within the calcification is less mineralized. If there are indeed differences in degree of mineralization then it is possible that, although atherosclerotic calcifications may be within the same plaque, the percent of mineral deposition may vary within and/or between calcifications due to aging or environmental differences (Grynpas et al. 1993). This merits further investigation. On the other hand, some research has sometimes found bone-like structures within calcifications containing trabeculae, lacunae, and marrow-like regions (Bostrom et al. 1995; Demer et al. 1994; Jeziorska et al. 1998b). The similarity of the reduced elastic properties and mineral-to-matrix ratio of calcification A6 to trabecular bone makes it plausible that a piece of bone-like structure was tested.

Other limitations to this study are that samples were formalin-fixed, dehydrated, and embedded. So caution must be taken when using the values obtained in this study although the qualitative differences should be real. Since the composition of atherosclerotic calcifications and bone are similar, it is possible that they will experience similar behavioral trends. Compared to hydrated bone samples, studies have shown that ethanol dehydration increases the nanoindentation elastic modulus of cortical bone by about 28% and ethanol dehydration with subsequent embedding in PMMA increases the elastic modulus by about 66% compared to wet bone (Bushby et al. 2004). The difference between Bushby et al.'s embedding study and the present work is that they allowed for PMMA infiltration into the sample, whereas, as seen by FTIR images, our protocol allows minimal infiltration (Figure 4.4). Infiltration is thought to be less than 70 μm from the edge. Sine trabeculae were indented at least 35 μm from the edge, its modulus may

have been affected by embedding. There is no data on the effects of alcohol dehydration and subsequent PMMA embedding on the reduced elastic moduli of trabecular bone. Formalin fixation has slight increase or no apparent effect on the Young's modulus of bone under bending (Currey et al. 1995; Sedlin et al. 1966) but causes a slight decrease under compression and tension (McElhaney et al. 1964). In general, more research should be conducted on how these factors affect the properties of atherosclerotic calcifications. Despite these issues, the elastic properties obtained from the present study provide a basis for properties that can be used in finite element models. If calcifications are assumed to be homogeneous and isotropic with a Poisson's ratio of 0.3, then their range of elastic moduli is 13.7 GPa to 23.9 GPa.[16] If calcifications were affected by alcohol dehydration in a similar manner as bone, the elastic modulus of hydrated calcifications would range from 11.6 GPa to 20.1 GPa.

In general, FTIR research has shown that formalin-fixation and embedding in PMMA has minimal effects on the mineral of older calcified tissue (such as the ones used in this study) or on the protein structure as was observed by analyzing the phosphate and amide I peaks, respectively (Boskey et al. 1982; Pleshko et al. 1992). More research should be conducted on how these factors affect the properties of atherosclerotic calcifications.

4.3. Conclusions

Three parameters were tested to determine their effects on the reduced elastic modulus of atherosclerotic calcifications: surface roughness and the load function's hold time and loading/unloading rates. There were no clear effects of roughness of the

[16] The reduced elastic moduli of calcification were calculated by rearranging equation 4.1.

microtomed surface on the reduced elastic modulus. In addition, the hold times in the load function had no apparent affect on reduced elastic modulus. The low loading/unloading rates, however, did affect the reduced elastic modulus mainly because they were long and the instrument experienced considerable thermal drift. By considering these effects, the present research was able to decrease the reported range of reduced elastic moduli for formalin-fixed calcifications from 0.18 MPa to 21,300 MPa to 14.8 GPa to 25.7 GPa. More accurate values can be attained by measuring a larger sample size of fresh calcifications. In addition, compression testing of calcifications should be done to fully validate its nanomechanical properties.

In general, atherosclerotic calcifications varied in mineralization and reduced elastic modulus from comparable to bone to much higher than bone. This difference can be detected by both FTIR-ATR and nanoindentation, respectively. In addition, the present study indicates that, as with other calcified materials, the mineral content of the atherosclerotic calcification affects its elastic properties: the higher the mineral content, the higher the elastic modulus. Since the number of samples is small, more studies should be done using a larger number of samples to verify these results. In addition, it is important to note that each indent samples at most an area of about 4 μm^2 whereas the FTIR-ATR scans an area of at most 6.3 mm^2. The FTIR scan area was big enough to scan the whole calcifications used in this study. At least 35 indents were taken per sample so the reduced elastic moduli could only be averaged over the number of indents taken; therefore, the moduli may not have been accurately sampled. The correlations between reduced elastic moduli and mineral-to-matrix ratios may be more accurately studied by using micro-FTIR and a larger indenter tip. Micro-FTIR can measure a range of areas, as

small as 10 μm by 10 μm (100 μm^2), and a 20 μm spherical tip would indent an area as large as 120 μm^2 at the maximum depths attained in this study, thus more accurate one-to-one correlations can be made between the reduced elastic moduli and mineral-to-matrix ratios.

Regardless of differences in tested area, the presence of a calcification whose reduced elastic modulus and mineral-to-matrix ratio were similar to that of bone indicates that calcifications may have anisotropic mechanical properties due to differences in local mineral content or the biomineralization process may not be the same between atherosclerotic calcifications, even from within the same plaque. Further research should be done to study these possibilities.

The nanomechanical properties obtained from the present research will allow for the development of more realistic finite element models that could aid in understanding how calcifications affect the atherosclerotic disease process and interact with current and new treatments. Although the coupling of nanoindentation and FTIR spectroscopy has provided some insight into the structure-property relationships of atherosclerotic calcifications, further development in both fields may allow further insights into the pathogenesis of the disease and how these may affect local mechanical properties.

Texas Library

4.4. References

Boskey, A. L.; Cohen, M. L.; and Bullough, P. G. 1982. Hard tissue biochemistry: A comparison of fresh-frozen and formalin-fixed tissue samples. *Calcified Tissue International* 34(4): 328-331.

Boskey, A. L. et al. 1992. Applications of Fourier-transform infrared (FTIR) microscopy to the study of mineralization in bone and cartilage. *Cells and Materials* 2(3): 209-220.

Bostrom, K. et al. 1995. Atherosclerotic calcification: Relation to developmental osteogenesis. *American Journal of Cardiology* 75(6): B88-B91.

Briscoe, B. J.; Fiori, L.; and Pelillo, E. 1998. Nano-indentation of polymeric surfaces. *Journal of Physics D - Applied Physics* 31(19): 2395-2405.

Bushby, A. J.; Ferguson, V. L.; and Boyde, A. 2004. Nanoindentation of bone: comparison of specimens tested in liquid and embedded in polymethylmethacrylate. *Journal of Materials Research* 19(1): 249-259.

Currey, J. D. 1988. The effect of porosity and mineral content on the Young's modulus of elasticity of compact bone. *Journal of Biomechanics* 21(2): 131-139.

Currey, J. D. et al. 1995. Effect of formaldehyde fixation on some mechanical properties of bovine bone. *Biomaterials* 16(16): 1267-1271.

Demer, L. L.; Watson, K. E.; and Bostrom, K. 1994. Mechanism of calcification in atherosclerosis. *Trends in Cardiovascular Medicine* 4(1): 45-49.

Doerner, M. F. and Nix, W. D. 1986. A method for interpreting the data from depth-sensing indentation instruments. *Journal of Materials Research* 1(4): 601-609.

Donnelly, E. et al. 2004. Effects of surface roughness and maximum load on the mechanical properties of cancellous bone measured by nanoindentation. *Biological and Bioinspired Materials and Devicies: Materials Research Society Symposium Proceedings* 823: 103-108.

Ebenstein, D. 2002. Biomechanical characterization of atherosclerotic plaques: A combined nanoindentation and FTIR approach. Ph. D. dissertation. UCSF/UCB Bioengineering Graduate Group, University of California, San Francisco and University of California, Berkeley.

Ebenstein, D. et al. 2004. A nanoindentation technique for functional evaluation of cartilage repair tissue. *Journal of Materials Research* 19(1): 273-281.

Fitzgerald, P. J.; Ports, T. A.; and Yock, P. G. 1992. Contribution of localized calcium deposits to dissection after angioplasty an observational study using intravascular ultrasound. *Circulation* 86(1): 64-70.

Fois, M. et al. 2001. Study of human cortical bone and demineralized human cortical bone viscoelasticity. *Journal of Applied Polymer Science* 79(14): 2527-2533.

Fondrk, M. et al. 1988. Some viscoplastic characteristics of bovine and human cortical bone. *Journal of Biomechanics* 21(8): 623-630.

Fuessl, R. T. et al. 2001. Vascular remodeling in atherosclerotic coronary arteries is affected by plaque composition. *Coronary Artery Disease* 12(2): 91-97.

Gibson, L. J. 1985. The mechanical behavior of cancellous bone. *Journal of Biomechanics* 18(5): 317-328.

Gong, J. K.; Cohn, S. H.; and Arnold, J. S. 1964. The density of organic and volatile and non-volatile inorganic components of cone. *Anatomical Record* 149(3): 319-324.

Grynpas, M. et al. 1993. Age and disease-related changes in the mineral of bone. *Calcified Tissue International* 53: S57-S64.

Gupta, H. S. et al. 2005. Two different correlations between nanoindentation modulus and mineral content in the bone-cartilage interface. *Journal of Structural Biology* 149(2): 138-140.

Herring, G. M. 1977. Methods for study of glycoproteins and proteoglycans of bone using bacterial collagenase: Determination of bone sialoprotein and chondroitin sulfate. *Calcified Tissue Research* 24(1): 29-36.

Hoffler, C. E. et al. 1997. Evaluation of bone microstructural properties: Effect of testing conditions, depth, repetition, time delay, and displacement rate. *Proceedings of the 1997 Bioengineering Conference* Sunriver, Oregon, USA. pgs. 567-568.

Hoffler, C. E. et al. 2000. Heterogeneity of bone lamellar-level elastic moduli. *Bone* 26(6): 603-609.

Huang, H. et al. 2001. The impact of calcification on the biomechanical stability of atherosclerotic plaques. *Circulation* 103(8): 1051-1056.

Jae-Young, R.; Tsui, T. Y.; and Pharr, G. M. 1997. Elastic properties of human cortical and trabecular lamellar bone measured by nanoindentation. *Biomaterials* 18(20): 1325-1330.

Jeziorska, M.; McCollum, C.; and Woolley, D. 1998. Observations on bone formation and remodelling in advanced atherosclerotic lesions of human carotid arteries. *Virchows Archives* 433(6): 559-565.

Klapperich, C.; Komvopoulos, K.; and Pruitt, L. 2001. Nanomechanical properties of polymers determined from nanoindentation experiments. *Journal of Tribology* 123(3): 624-631.

Li, C. et al. 2003. Biochemical characterization of atherosclerotic plaque constituents using FTIR spectroscopy and histology. *Journal of Biomedical Materials Research* 64A(2): 197-206.

Marshall, G. et al. 2001. Mechanical properties of the dentinoenamel junction: AFM studies of nanohardness, elastic modulus, and fracture. *Journal of Biomedical Materials Research* 54(1): 87-95.

McElhaney, J. et al. 1964. Effect of embalming on mechanical properties of beef bone. *Journal of Applied Physiology* 19(6): 1234-1236.

Nobuyoshi, M. et al. 1991. Restenosis after percutaneous transluminal coronary angioplasty: Pathological observations in 20 patients. *Journal of the American College of Cardiology* 17(2): 433-439.

Oliver, W. C. and Pharr, G. M. 1992. Improved technique for determining hardness and elastic modulus using load and displacement sensing indentation experiments. *Journal of Materials Research* 7(6): 1564-1580.

Park, J. C.; Siegel, R. J.; and Demer, L. L. 1993. Effect of calcification and formalin fixation on in vitro distensibility of human femoral arteries. *American Heart Journal* 125(2 part 1): 344-349.

Paschalis, E. et al. 1996. FTIR microspectroscopic analysis of human osteonal bone. *Calcified Tissue International* 59(6): 480-487.

Paschalis, E. et al. 1997. FTIR microspectroscopic analysis of normal human cortical and trabecular bone. *Calcified Tissue International* 61(6): 480-486.

Pleshko, N. L.; Boskey, A. L.; and Mendelsohn, R. 1992. An FT-IR Microscopic investigation of the effects of tissue preservation on bone. *Calcified Tissue International* 51(1): 72-77.

Rho, J. Y.; Tsui, T. Y.; and Pharr, G. M. 1997. Elastic properties of human cortical and trabecular lamellar bone measured by nanoindentation. *Biomaterials* 18(20): 1325-1330.

Rho, J. Y. et al. 1999. Elastic properties of microstructural components of human bone tissue as measured by nanoindentation. *Journal of Biomedical Materials Research* 45(1): 48-54.

Richardson, P.; Davies, M.; and Born, G. 1989. Influence of plaque configuration and stress distribution on fissuring of coronary atherosclerotic plaques. *Lancet* 2(8669): 941-944.

Roy, M. E. et al. 1999. Mechanical and morphological variation of the human lumbar vertebral cortical and trabecular bone. *Journal of Biomedical Materials Research* 44(2): 191-197.

Salunke, N. V. et al. 2001. Compressive stress-relaxation of human atherosclerotic plaque. *Journal of Biomedical Materials Research* 55(2): 236-241.

Schmid, K. et al. 1980. Chemical and physicochemical studies on the mineral deposits of the human atherosclerotic aorta. *Atherosclerosis* 37(2): 199-210.

Sedlin, E. D. and Hirsch, C. 1966. Factors affecting determination of physical properties of femoral cortical bone. *Acta Orthopaedica Scandinavica* 37(1): 29.

Smith, B. C. 1996. *Fundamentals of Fourier Transform Infrared Spectroscopy*. Boca Raton: CRC Press.

Stilwell, N. A. and Tabor, D. 1961. Elastic recovery of conical indentations. *Proceedings of the Physical Society* 78(Part 2, 500): 169-179.

Swadener, J. G.; Rho, J. Y.; and Pharr, G. M. 2001. Effects of anisotropy on elastic moduli measured by nanoindentation in human tibial cortical bone. *Journal of Biomedical Materials Research* 57(1): 108-112.

Tesch, W. et al. 2001. Graded microstructure and mechanical properties of human crown dentin. *Calcified Tissue International* 69(3): 147-157.

Zhou, J. et al. 2004. Tribological and nanomechanical properties of unmodified and crosslinked ultra-high molecular weight polyethylene for total joint replacements. *Journal of Tribology: Transactions of the ASME* 126(2): 386-394.

Zysset, P. K. et al. 1999. Elastic modulus and hardness of cortical and trabecular bone lamellae measured by nanoindentation in the human femur. *Journal of Biomechanics* 32(10): 1005-1012.

Table 4.1: Reduced elastic moduli for various depth-to-rms roughness ratios

Average reduced elastic moduli and coefficients of variance for different ranges of maximum depth-to-rms roughness ratio of three calcifications

Maximum depth-to-rms roughness ratio	1-2			3-4			5-6			8-9		
	Er*	Std Dev**	COV***	Er	Std Dev	COV	Er	Std Dev	COV	Er	Std Dev	COV
Calcification A2	29.9	3.2	0.11	27.9	8.6	0.31	24.9	7.0	0.28	-	-	-
Calcification B3	-	-	-	35.2^	7.3	0.21	-	-	-	19.8^	4.7	0.24
Calcification C2	29.1	7.9	0.27	23.9	5.3	0.22	-	-	-	-	-	-

* Er is an abbreviation for reduced elastic modulus
** Std Dev is an abbreviation for standard deviation
*** COV is an abbreviation for coefficient of variance
^ Significant difference between the two numbers ($p < 0.05$)
- Group contains less than five data points

Table 4.2: Maximum depth data at various depth-to-rms roughness ratios
Average maximum depth data of for four different ranges of maximum depth-to-rms ratios for three calcifications

	Maximum depth (nm) (Standard Deviation)			
Maximum depth-to-rms roughness ratio	1-2	3-4	5-6	8-9
Calcification A2	204.5† (67.1)	309.48 (78.6)	349.66† (77.0)	-
Calcification B3	-	195.4* (87.3)	-	504.5* (109.1)
Calcification C2	241.1 (151.6)	287.5 (80.5)	-	-

* or † Significant difference between the two numbers ($p < 0.05$)
- Group contains less than five data points

Table 4.3: Reduced elastic moduli for various holding times
Reduced elastic moduli of three calcifications at seven different holding times

	Reduced Elastic Modulus (Standard Deviation)						
Hold Time (seconds)	5	10	25	50	75	100	125
Calcification A5	-	-	29.3 (2.5)	30.3 (4.7)	33.3 (4.9)	33.8 (5.0)	32.4 (6.5)
Calcification B3	-	18.5 (0.9)	19.5 (3.6)	19.5 (3.5)	19.0 (2.5)	-	-
Calcification C2	17.9 (1.8)	17.5 (1.9)	16.7 (1.9)	16.2 (1.2)	18.2 (1.7)	16.9 (1.2)	18.1 (2.5)

- Group contains less than five data points

Table 4.4: Reduced elastic moduli for various loading rates

Reduced elastic moduli of three calcifications at seven different loading and unloading rates

	Reduced Elastic Modulus (Standard Deviation)						
Loading and Unloading Rates (μN/s)	100	250	400	550	700	850	1000
Calcification A5	32.1*^ (5.1)	35.6† (3.2)	38.7 (3.8)	38.3 (5.4)	38.3 (4.1)	41.1* (4.2)	42.7^† (6.5)
Calcification B3	-	20.7 (2.9)	23.3 (4.9)	-	25.2 (4.3)	-	24.0 (4.5)
Calcification C2	19.1 (2.8)	20.6 (3.6)	20.8 (3.1)	21.3 (4.6)	25.1 (4.4)	26.6 (6.4)	22.2 (4.8)

* ^ † Significant difference between the two numbers ($p < 0.05$)

- Group contains less than five data points

Table 4.5: Properties of atherosclerotic calcifications and bone
Average reduced elastic moduli and mineral-to-matrix ratios of atherosclerotic calcifications and bone

Sample		Reduced Elastic Modulus		Mineral-to-Matrix Ratio	
		Average (GPa)	Standard Deviation (GPa)	Average	Standard Deviation
Plaque A	Calcification A1	23.9	7.5	-	-
	Calcification A6	14.8	3.4	9.2	0.8
	Calcification A7	20.9	4.8	64.5	12.5
Plaque B	Calcification B4	19.3	5.0	87.3	30.6
Plaque C	Calcification C3	25.7	8.1	141.5	60.7
Bone	Bone A	9.6	2.7	8.2	0.4
	Bone B	10.6	3.6	-	-
	Bone C	10.6	3.1	10.3	2.9
	Bone D	11.2	4.4	12.8	1.7

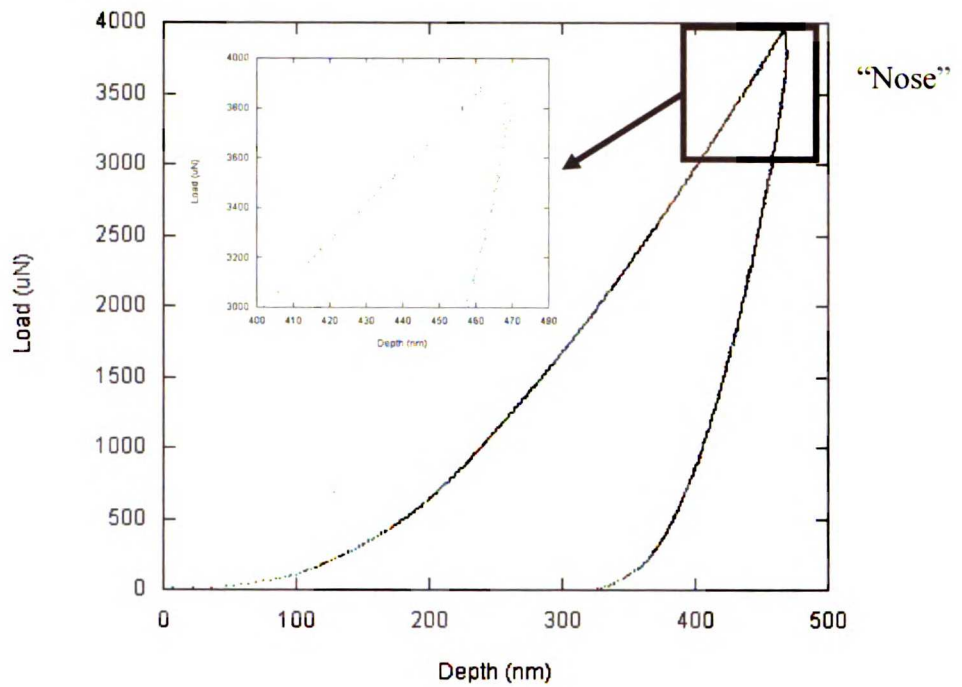

(a)

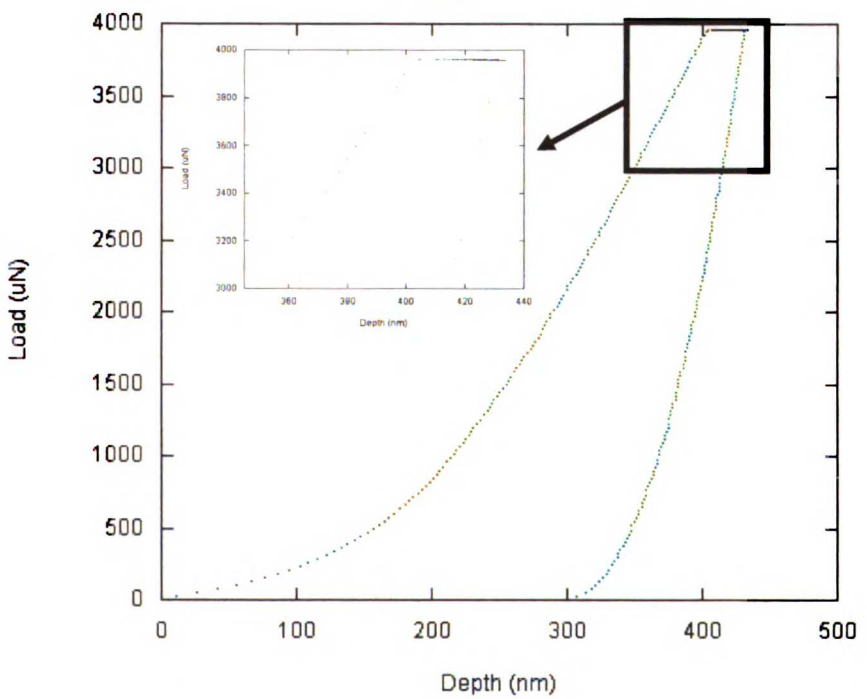

(b)

Figure 4.1: Viscoelastic behavior captured during nanoindentation
Load versus displacement curve of an indent using (a) a triangular loading function (constant loading and unloading rate) demonstrating the "nose" phenomenon caused by creep (b) a trapezoidal loading function demonstrating how a hold time between the loading and unloading curve reduces the "nose"

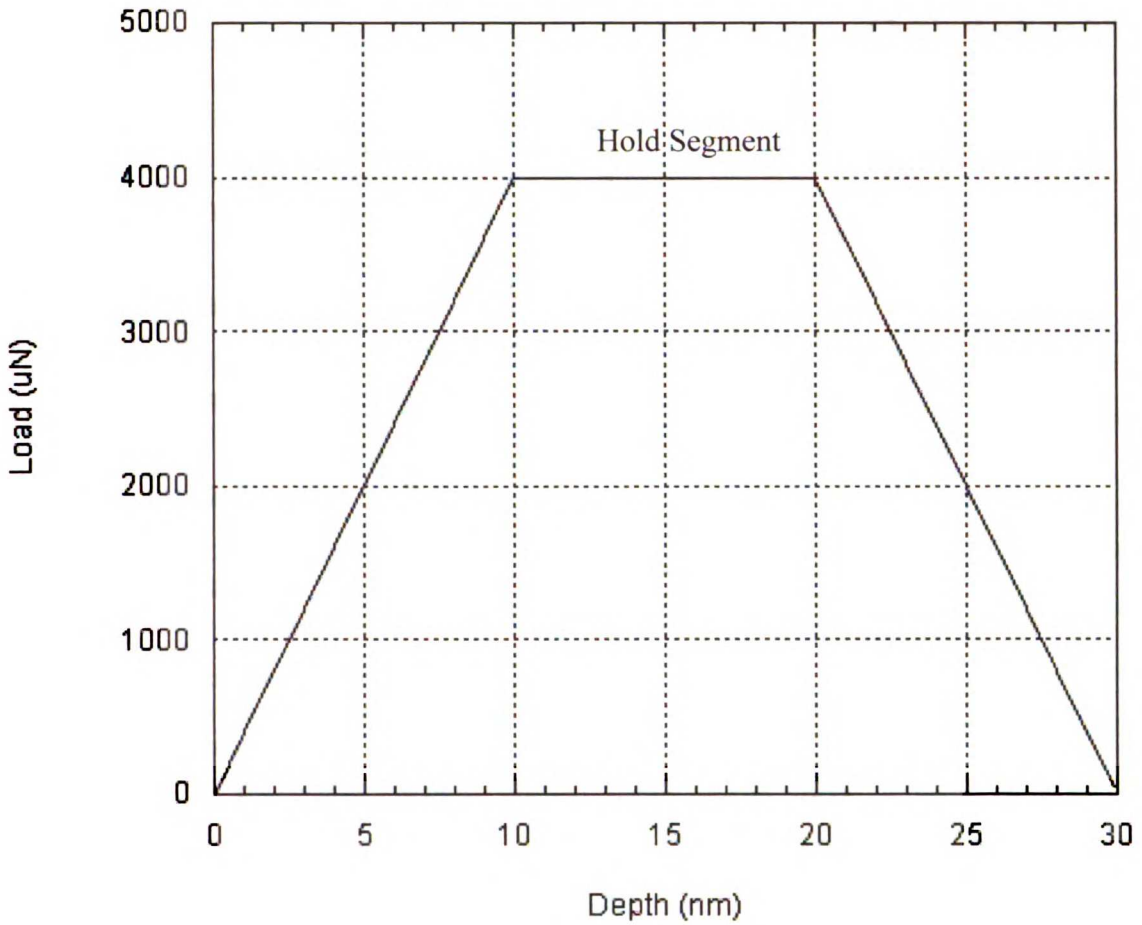

Figure 4.2: Nanoindentation load function
Trapezoidal loading curve used to determine the reduced elastic moduli of atherosclerotic calcifications and bone

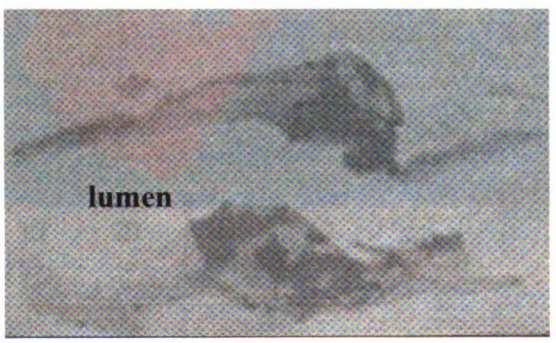

Figure 4.3: Magnetic resonance image of a highly calcified carotid plaque
The darkest regions are the calcified regions while the rest of the tissue appears in different shades of grey.

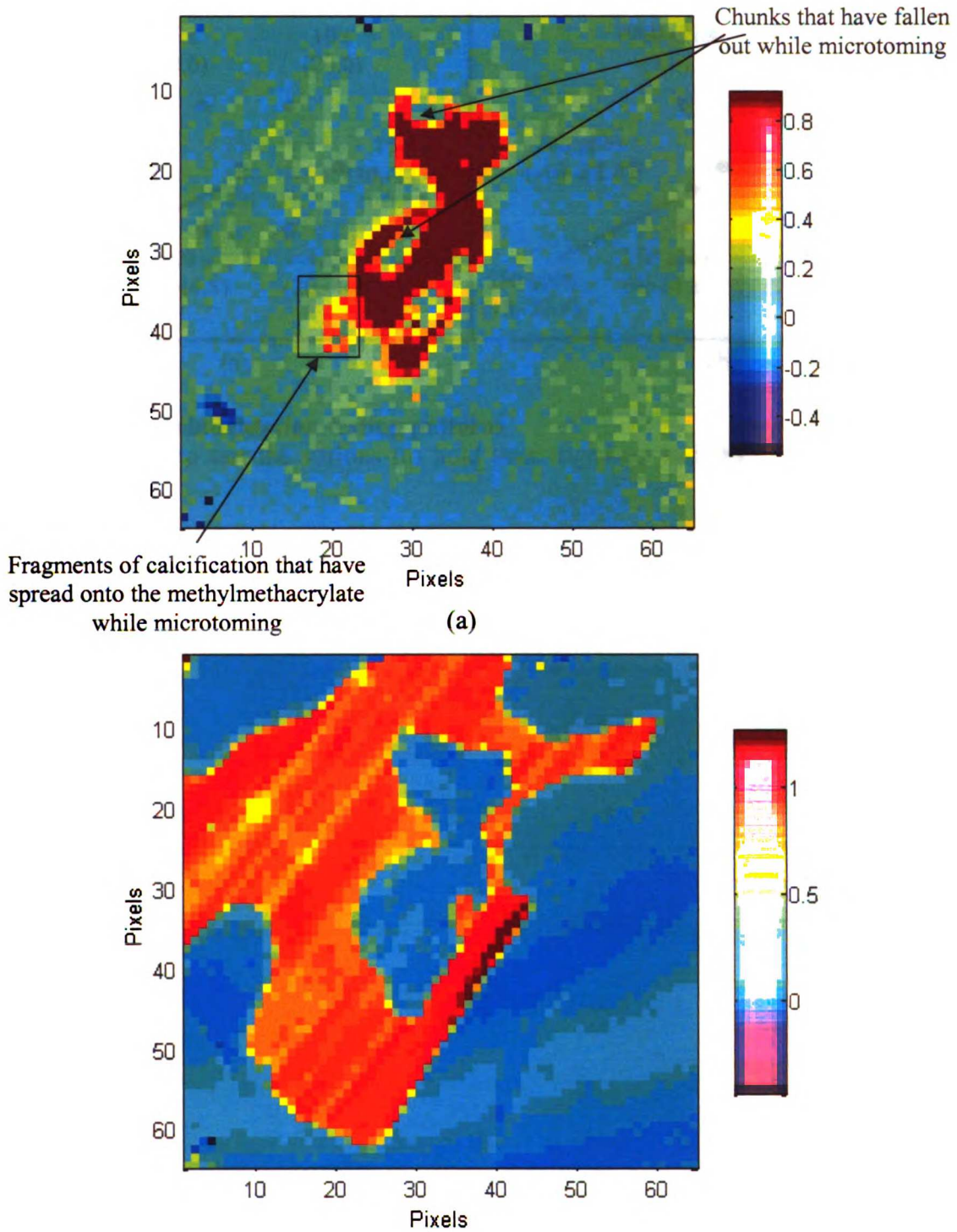

Figure 4.4: Micro-FTIR two-dimensional image of calcification
Micro-FTIR images of a slice of atherosclerotic calcification embedded in polymethyl-methacrylate (PMMA) demonstrating the minimal infiltration of PMMA. (a) Regions containing mineral phosphate appear bright yellow and hues of red. (b) Regions containing PMMA appear bright yellow and hues of red.

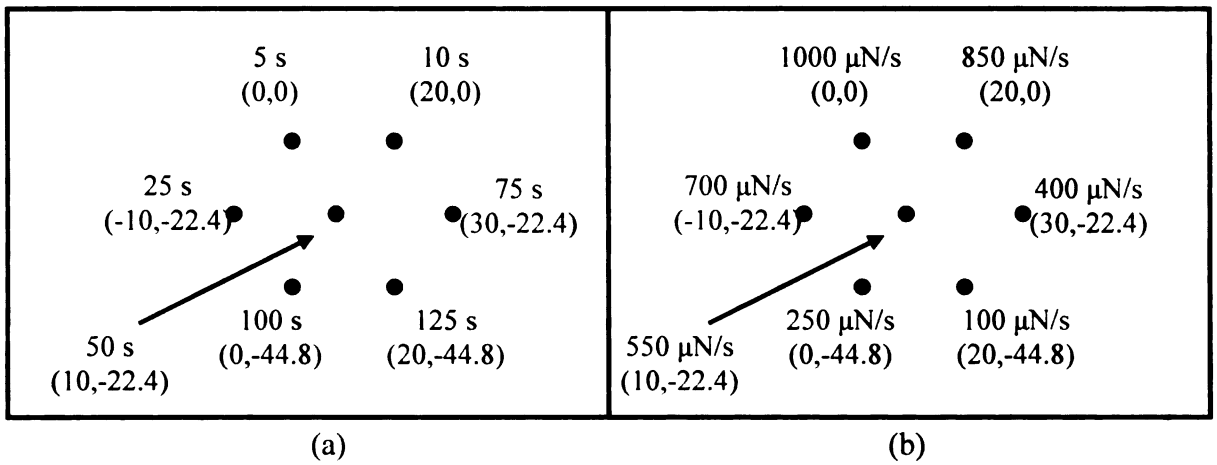

Figure 4.5: Nanoindentation testing patterns
The pattern used to test the various (a) hold time segments and (b) loading/unloading rates

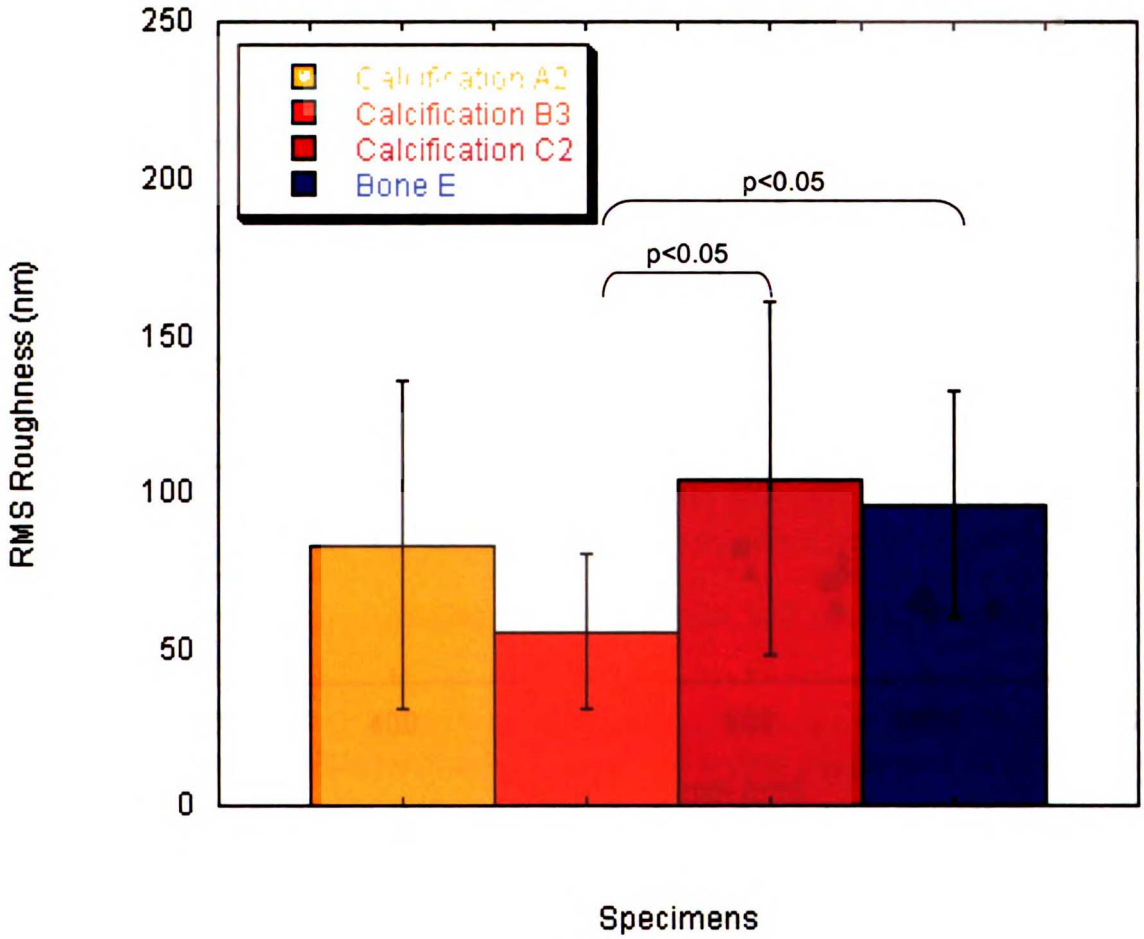

Figure 4.6: RMS roughness of three microtomed calcifications and one bone

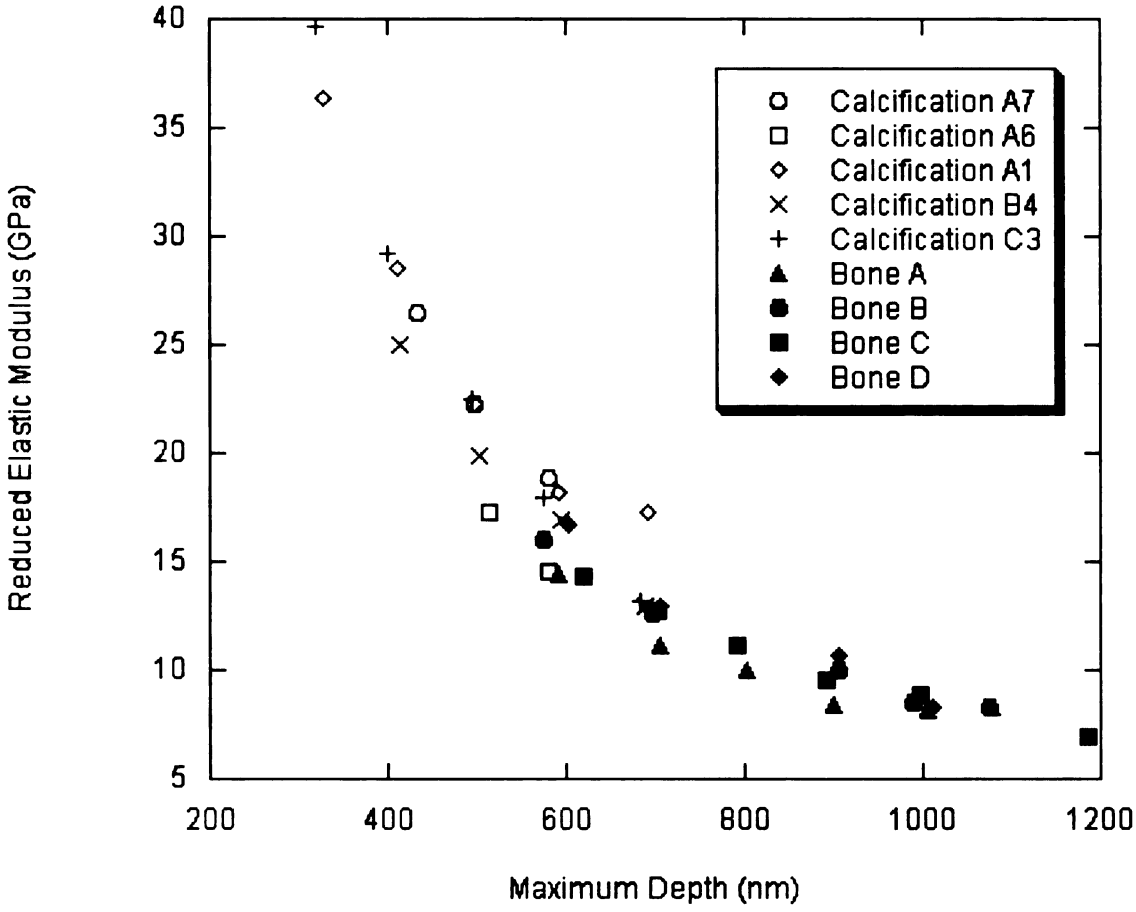

Figure 4.7: Elastic properties of atherosclerosis calcification and bone
The reduced elastic moduli of atherosclerotic calcification and trabecular bone as a function of maximum depth.

Chapter 5

Characterization of Mineralized Tissue using Fourier Transform Infrared Spectroscopy

5.0. Introduction

There is still not a complete understanding as to how atherosclerotic calcifications initiate and develop or whether there are variations in their composition with anatomical location, growth, or age. Characterizing their composition and determining whether variations exist are important to understanding the biomineralization of atherosclerotic calcifications. Insights into this process could aid in the development of pharmaceutical therapies or devices for controlling the development and growth of atherosclerotic calcifications.

As discussed in Chapter 2, evidence exists of several mechanisms of initiation of atherosclerotic calcifications. As with bone, the growth of atherosclerotic calcification is an active process that begins in matrix vesicles (among other sites of initiation) and is controlled by regulating factors similar to those in bone samples: osteopontin, osteocalcin, and bone morphogenetic protein-2a (Bostrom et al. 1993; Gadeau et al. 2001; Gijsbers et al. 1990). Atherosclerotic calcifications and bones also have similar compositions. In general, atherosclerotic calcifications are made up of about 78% carbonate-containing hydroxyapatite and 15% protein by dry weight (Schmid et al. 1980). Bone mainly comprises 70% to 75% hydroxyapatite and 24% protein by dry weight (Gong et al. 1964; Herring 1977). The composition of bone during growth and aging has been more widely studied (Ott 2002; Paschalis et al. 1997; Paschalis et al. 2001; Rey et al. 1991a), and thus, the mechanism of its formation and development is

better understood. Atherosclerotic calcifications also need more profound studies. Given the scope of this task, the present research only focuses on late-stage atherosclerotic calcifications,[17] exploring their general composition, especially their mineral phase, and making comparisons with trabecular bone.

Fourier transform infrared spectroscopy (FTIR) is an invaluable tool for studying the biochemical composition of samples since it provides information about the tissue components in the sample. FTIR has been successfully used to study the composition of normal and diseased tissues such as cartilage, bone, teeth, vascular matrix vesicles, and even isolated calcifications (Boskey et al. 2000; Boskey et al. 1992; Hsu et al. 1999; Rey et al. 1991b; Tomazic et al. 1988). The studies of vascular matrix vesicles and isolated calcifications provide evidence that calcifications may begin as an amorphous mineral or octacalcium phosphate, both of which are also suggested precursors of bone (Brown 1966; Hsu et al. 2000; Termine et al. 1967; Tomazic et al. 1988). Although the origin of atherosclerotic calcifications is unclear, FTIR studies of more developed calcifications have demonstrated that, like bone samples, they contain protein and a carbonate-containing analog of hydroxyapaptite (Manoharan et al. 1993; Tomazic et al. 1988). This corroborates the initial physiochemical analysis of Schmid et al. (1980) mentioned above. Other research has used FTIR spectra of atherosclerotic calcifications or calcified plaque to determine the qualitative amount of mineral content by measuring the amount of mineral in the spectra and dividing it by the amount of matrix (Ebenstein 2002;

[17] Type Vb plaques (according to Stary's classification) described in detail in Chapter 2

Manoharan et al. 1993).[18] However, no further qualitative FTIR analysis has been done on isolated atherosclerotic calcifications.

FTIR provides additional qualitative information about the mineral phase of bone revealing that it is a poorly crystalline analog of hydroxyapatite containing carbonate and acidic-phosphate that experiences changes with age (Pleshko et al. 1991; Rey et al. 1991a; Rey et al. 1990). The carbonate and mineral content increases in bone mineral with the individual's and tissue age while the acid phosphate groups decrease (Legros et al. 1986; Paschalis et al. 1997; Rey et al. 1991a). Carbonate is known to substitute for the phosphate or hydroxyl anions or in unstable locations in the crystal lattice of biological apatites (Rey et al. 1991a). Acid phosphate substitutes for phosphate anions in the biological crystal apatites (Rey et al. 1990). That the hydroxyapatites of both bone and atherosclerotic calcifications have lattice defects such as carbonate substitutions is evident because they do not have the stoichiometric calcium-to-phosphate ratio of 1.66 (Grynpas et al. 1993; Yu 1974). In bone, this ratio is affected by the presence of lattice changes such as the inclusion or absorption of extraneous ions as carbonate, magnesium, and sodium (Grynpas et al. 1993). Since atherosclerotic calcifications have shown to contain carbonate and magnesium (Schmid et al. 1980), they may also cause similar crystal lattice defects. In addition, atherosclerotic calcifications may also experience changes in their mineral phase with age or maturation. This is supported by the increasing calcium-to-phosphate ratio of atherosclerotic calcification with patient age, approaching that of stoichiometric apatite of 1.66 (Yu 1974).

[18] Boskey et al. found correlations between the mineral content and these mineral-to-matrix ratio measurements (Boskey et al. 1992).

Given the similarities in the initiation sites of biomineralization, in the type of regulatory factors, and in the general composition between atherosclerotic calcifications and bone, some researchers suggest their biomineralization processes may also be similar (Doherty et al. 1994; Tanimura et al. 1986a). By using FTIR, this project aims to determine whether there are further similarities in composition between these two tissues and thus, provide more information about the biomineralization process of atherosclerotic calcifications.

FTIR spectra provide several means of measuring the quantity and composition of the mineral phase. A qualitative mineral content measurement can be done by calculating the area under the v_1, v_3 phosphate peak and dividing it by the area under the amide I peak[19] (Boskey et al. 1992). The relative amount of carbonate in the hydroxyapatite may be measured from the FTIR spectrum by measuring the amount of v_2 carbonate in the spectra and dividing it by the amount of v_1, v_3 phosphate (Figure 5.1) (LeGeros et al. 1983; Paschalis et al. 1996). The type of carbonate substitution can be found by studying the underlying bands that make up the v_2 carbonate peak (Rey et al. 1991a). The relative mineral crystalline size or maturity may be measured by analyzing the shape of the v_4 phosphate peak[20] in the FTIR spectrum (Figure 5.1) (Termine et al. 1966). Studies using this technique have found that the bone's crystals increase in size and perfection with bone age (Rey et al. 1991a). Furthermore, the presence of hydroxyapatite inclusions such as acidic-phosphate may be measured by finding the underlying bands that make up the v_1, v_3 phosphate peak (Gadaleta et al. 1996b; Leung et al. 1990). Given the amount of

[19] The amide I peak is a measure of energy absorbed by the sample that causes the stretching of the carbon–oxygen double bond in the peptide bond of the protein's secondary structure.
[20] The v_4 phosphate peak is a measure of the energy absorbed by the sample that causes phosphorus–oxygen bond asymmetric stretching.

information that can be extracted from just one FTIR spectrum, FTIR has the potential to be an invaluable tool for studying the composition of atherosclerotic calcifications. Assuming that these techniques may be extended to the study of atherosclerotic calcifications, this study uses these techniques to characterize its mineral phase.

5.1. Materials and Methods

The experiment consists of taking the FTIR spectra of atherosclerotic calcifications and bone samples. First, the FTIR spectra are used to determine general composition of both. From the spectra, three measurements are taken of *(i)* the qualitative mineral content, *(ii)* the qualitative carbonate content, and *(iii)* crystalline size or maturity. The second derivative[21] of the v_2 carbonate peak is used to determine the type of carbonate substitution. Finally, the second derivative of the v_1, v_3 phosphate peak is used to determine its underlying bands and thus obtain more specific information about the mineral phase. All statistical analyses are done using nonparametric Mann-Whitney tests.

5.1.1. Sample Preparation

The explanation of how the samples were obtained and prepared is given in Section 4.1.1. In this study, five calcifications were taken from plaque A; five, from plaque B; and three, from plaque C. Four trabecular bone samples (A through D) were also taken. All samples taken were from humans older than 50 years old. In this study, the samples were not embedded in PMMA, but were formalin-fixed. Formalin-fixation is

[21] The technique of taking the second derivative of the spectrum to determine underlying bands is explained in Chapter 3.

a suitable technique to prepare the samples since the cross-linking of the amino acid in the protein may preserve the secondary structure (i.e., amide I) instead of denaturing it (Mason et al. 1991).

After dehydration in increasing concentrations of ethanol, each sample was ground in a mortar with a pestle. Approximately 1 mg of sample was weighed out and mixed with 80 mg of potassium bromide powder. This mixture was compressed into pellets using a high-pressure hand press, Spectra-Tech Qwik Handi-Press (Thermo Electron Corporation, Waltham, MA).

One FTIR spectrum was obtained for each calcification and bone sample with a mid-infrared interferometer, Nicolet 8700 Research FT-IR Spectrometer (Thermo Electron Corporation, Waltham, MA): 256 scans, 4 cm^{-1} spectral resolution. The interferograms were apodized with a Happ-Genzel function and Fourier transformed. The resulting spectrum was used to measure the mineral-to-matrix ratio. The mineral content was calculated by baselining the v_1, v_3 phosphate peak (~ 900 cm^{-1} to 1200 cm^{-1}) and then integrating the area under this region. Similarly, the matrix was calculated using the amide I peak (~ 1600 cm^{-1} to 1725 cm^{-1}). Then the area under the phosphate peak was divided by the area under the amide I peak to obtain the mineral-to-matrix ratio. The carbonate-to-mineral ratios were also calculated in a similar manner; the v_2 carbonate peak is approximately between 840 cm^{-1} to 890 cm^{-1}.

The v_4 phosphate peak (~ 500 cm^{-1} to 670 cm^{-1}) is split mainly into two peaks (Figure 5.2). Stoichiometric apatite would have three peaks in this region but carbonate substitution of phosphate decreases the number of peaks to two (Francis et al. 1971). Using Win-IR Software (Bio-Rad Laboratories, Randolph, PA), the depth of splitting of

the v_4 phosphate peak was calculated relative to its two peaks. Past research has correlated this measurement to degree of crystallinity (Termine et al. 1966). The spectrum was first baseline subtracted between approximately 500 cm^{-1} to 670 cm^{-1}. Then the maximum of each peak (at about 563 cm^{-1} and 602 cm^{-1}) and the minima between the peaks (at about 590 cm^{-1}) were found visually. A line was drawn between the maxima of both peaks to obtain the tangent line of both peaks. The height, *a*, (height between the local minima at about 590 cm^{-1} and the tangent line) was measured. Then the height, *b*, (height between the local minima and the baseline) was measured. Finally, the relative degree of crystallinity was measured by calculating:

$$\frac{a}{a+b} \tag{5.1}$$

The three bands that make up the v_2 carbonate peak were found mainly by baselining the carbonate peak and taking the second derivative of the spectrum using Isys software (Spectral Dimensions, Inc., Olney, MD) (Figure 5.3). In the second derivative spectrum, a local minimum between two local maxima indicates the location of a local maximum in the spectrum (Leung et al. 1990). The same method was used to determine the underlying bands of the v_1, v_3 phosphate peak.

5.2. Results and Discussion

5.2.1. General Composition

Both bone and atherosclerotic calcifications have been characterized primarily as carbonate-substituted hydroxyapatite containing some matrix (e.g., collagen for bone and collagen and elastin for atherosclerotic calcifications (Manoharan et al. 1993; Rey et al.

1991a; Rey et al. 1991b; Tomazic et al. 1988). FTIR spectra of atherosclerotic calcifications from the present study corroborate past work, illustrating similarities between the two mineralized tissues (Figure 5.1) (Manoharan et al. 1993; Tomazic et al. 1988). Spectra from both types of mineral contain two phosphate peaks of the hydroxyapatite: the sharp v_4 (~ 500 cm^{-1} to 670 cm^{-1}) phosphate peak and the more complex, broader v_1, v_3 (~ 900 cm^{-1} to 1200 cm^{-1}) phosphate peak. As in bone, the v_1, v_3 phosphate peak of atherosclerotic calcifications is intense and its broadness is attributed to the poorly crystalline nature of the hydroxyapatite since the broad peak indicates that the hydroxyapatite contains nonstoichiometric mineral, which can be revealed by determining the underlying bands (Leung et al. 1990; Rey et al. 1991b). In addition, both atherosclerotic calcifications and bone have the amide I (~ 1600 cm^{-1} to 1725 cm^{-1}), which is the secondary structure of protein (e.g., collagen and/or elastin) (Figure 5.1). Although carbonate, magnesium, and sodium ions have been found in atherosclerotic calcifications, the presence of carbonate in this study is most noticeable, as it is observed in the FTIR spectra between 840 cm^{-1} to 890 cm^{-1} (Figure 5.1) (Schmid et al. 1980). It is interesting to note that in previous FTIR studies of vascular matrix vesicles of human, this carbonate peak also seems to exist, suggesting that carbonate substitution into the apatite lattice occurs very early in mineralization development (Hsu et al. 1999). Carbonate (~ 1412 cm^{-1} to 1545 cm^{-1}) and amide II (~ 1520 cm^{-1} to 1570 cm^{-1}) [22] are also known to occur in bone (Figure 5.1) (Boskey et al. 1992; Termine et al. 1973). These peaks also seem to be present in atherosclerotic calcifications but they are not completely distinguishable since they partially overlap with other peaks.

[22] The amide II peak is a measure of energy absorbed by the sample that causes a mixed carbon-nitrogen stretch and nitrogen-hydrogen in-plane bending of the protein's secondary structure.

5.2.2. Mineral Content

The most significant difference in the composition between atherosclerotic calcifications and bone is that bone has more protein as revealed by its higher amide I peak (Figure 5.1). The mineral-to-matrix ratio has been correlated to ash density, which is a measure of mineral content (Boskey et al. 1992). Since the average value of mineral-to-matrix ratio for arterial calcifications (14.9) is significantly higher ($p < 0.001$) than that of bone (5.0), they are, on average, more mineralized. This corroborates the physiochemical analysis done by Schmid et al. (1980), which found that atherosclerotic calcifications have higher hydroxyapatite by dry weight than bone. This conclusion was also attained in the previous chapter using FTIR in attenuated transmission reflection (ATR) mode. Using FTIR, the mineral-to-matrix ratios range from 9.9 to 18.2, while in the results from the last chapter, using FTIR-ATR, the average ratios range from 9.2 to 141.5. The main reason for this difference is that the spectrum is noisier in ATR mode, and this contributes to the higher values and standard deviations in ATR mode.[23] The results from the FTIR analysis in this section are in more agreement with previous work that attained calcification mineral-to-matrix ratios from between 7.1 and 14.1 though these measurements were only taken from three formalin-fixed calcifications using FTIR-ATR (Ebenstein 2002). From the graphs in Paschalis et al.'s studies, mineral-to-matrix average ratios for trabecular bone appear to range from 3.4 to 6.5 (Paschalis et al. 1997). In the present study, the range for trabecular bone is 4.6 to 5.3, which falls within the range in the literature, thus helping to validate the present work.

[23] See previous chapter for details

Another distinction found between the two types of tissues is that the difference in the mineral-to-matrix ratios for atherosclerotic calcifications is 8.3, while that of the bone is 0.7 in the present study and 3.1 in literature. This large difference occurs even with calcifications from the same plaque as seen from plaque A that has one calcification with a mineral-to-matrix ratio of 9.9 and another with a ratio of 18.2 (Table 5.1). This large difference in mineral content between calcifications, even from within the same plaque, was also observed in the experiments discussed in the previous chapter. The main difference in the experimental techniques discussed in chapter 4 and in this chapter is that, in chapter 4, averaged spectra were taken of one microtomed *surface* of the sample (using FTIR-ATR) while this chapter compares averaged spectra taken of a mixture of the *whole* sample (using FTIR). Thus, the data from the FTIR-ATR are local representations of the calcifications' composition while data from the FTIR are more global. Since the FTIR-ATR data is more localized, it is not clear whether the large mineral content differences observed in atherosclerotic calcifications exist within and/or between the calcifications. Since the FTIR data in this chapter is more of a global representation of the calcifications and similar finding were observed, then this suggests that there may indeed be differences in mineral content between calcifications even from within the same plaque. Since all the atherosclerotic calcifications are from patients greater than 50 years old, then the differences found may be due to differences in the tissue age (as occurs in bone) or in the physiochemical environment where the calcifications develop (Paschalis et al. 1997). More research is needed to discern the reason for these differences.

5.2.3. Relative Carbonate Content

Another measurement taken was the carbonate-to-mineral ratio, which is a measure of the relative amount of carbonate in the sample. In this case, there is no significant difference in the average carbonate-to-mineral ratio between the bone samples and atherosclerotic calcifications (Table 5.1). Although there are no previous measurements done on trabecular bone that can be used for comparison, the results indicate potential similarities in the substitution mechanisms of both types of tissue. However, the difference in the carbonate-to-phosphate ratios for atherosclerotic calcifications (0.011) is larger than that of bone (0.004). Although it is not clear whether acidic phosphate is another substitute of the lattice, caution should be taken when interpreting these results because an acidic phosphate band (~870 cm^{-1}) may cause an overestimate of the carbonate content (LeGeros et al. 1987).

Carbonate has been found to increase in concentration with increasing age the bone tissue (Paschalis et al. 1996). If this is also true in atherosclerotic calcifications, then the large range in relative carbonate substitution may be an indication of differences in age of the calcification tissue. Since evidence also exists that the carbonate may significantly affect the initial stages of caries formation in enamel and bone reabsorption process, the amount of carbonate content may also be linked to the development or age of atherosclerotic calcifications (Biltz et al. 1981; Hallsworth et al. 1973). Further investigation should measure the amount of carbonate as a function of age to determine if carbonate content is indeed connected to calcification development or age.

5.2.4. Degree of Crystallinity and Maturity

Studies of the maturation of mineralized tissues have shown that labile (e.g., unstable) ionic environments tend to decrease while stable environments increase (Rey et al. 1995). In addition, during maturation, poorly crystalline apatites are believed to evolve into highly crystalline apatites by relocating their unstable phosphate and carbonate groups and increasing their phosphate and hydroxyl groups in the apatitic lattice (Cazalbou et al. 2004). This change in relative amount of unstable and stable environments may be measured in the degree of splitting of the v_4 phosphate peak, which has been correlated to the relative degree of crystallinity and maturity (Termine et al. 1966). These measurements were taken using equation (5.1). The average degree of crystallinity and maturity was significantly higher ($p<0.001$) for atherosclerotic calcifications (0.31) than for bone (0.27).

These results must be considered carefully, however. First of all, no previous measurements have been taken of human trabecular bone so that, although the atherosclerotic calcifications appear more crystalline and mature than the bone samples in this study, the results may not be true in general. If, however, these results are true, atherosclerotic tissue may have an environment that promotes greater crystallinity and maturity. In older bone, both the mineral content and crystallinity/maturity are higher than for newly deposited bone; thus the mineral-to-matrix ratio increased with increasing crystallinity and maturity (Paschalis et al. 1996) (Figure 5.4). This also seems to be the case in atherosclerotic calcifications as seen in Figure 5.4 and may indicate that both samples mature by similar mechanisms. To verify this, studies should determine how the mineral content and crystallinity changes with age.

5.2.5. Carbonate Substitution

The second derivative of the v_2 carbonate peak was taken to determine the underlying bands. As in bone, bands at 878 cm^{-1} and 871 cm^{-1} were found in atherosclerotic calcifications (Figure 5.3) (Rey et al. 1989). The 878 cm^{-1} is attributed to type A carbonate, which occupies the hydroxyl sites in the hydroxyapatite crystals (Rey et al. 1989). One the other hand, band 871 cm^{-1} occupies the phosphate site and is considered type B carbonate (Rey et al. 1989). Since the maximum height of the carbonate peak of atherosclerotic calcifications occurs at 871 cm^{-1}, then this band appears to be the most abundant, as in bone. A band at 866 cm^{-1} has been shown to exist in bone but it was not present in either bone or atherosclerotic calcifications in this study (Rey et al. 1989). This band corresponds to a carbonate in a labile (e.g., unstable) lattice location (Rey et al. 1989). That the band was not observed in bone suggests that the method of determining the underlying band may not have been sensitive enough to differentiate the band. This may have been the case since, in the second derivative of the spectrum, a negative peak may be masked by an overlapping positive peak if they are close to each other in wavenumber (Leung et al. 1990). Furthermore, the ratio of the amplitudes in the second derivative varies inversely to the square of their half width ratio (Maddams et al. 1982a); therefore, the second derivative of a broad band may have too small of an amplitude to discern and, thus, the numbers of underlying bands may be underestimated. In conclusion, it is not possible to discern, with this technique, whether the band exists for atherosclerotic calcifications.

In bone, ratios of Type A to Type B carbonate remain relatively constant while a pattern of decreasing labile carbonate seems to exist as the bone tissue matures and

become more similar to stoichiometric apatite (Paschalis et al. 1996). To understand better the role of carbonate substitution in the apatite of atherosclerotic calcifications, it would be important to measure the relative contributions of the different types of carbonate change with age.

5.2.6. Details of the Mineral Phase

The second derivative of the v_1, v_4 phosphate peak was also taken to determine its underlying bands (Table 5.2). Most of the underlying bands were found to be the same in atherosclerotic calcifications and bone. Several bands (1000, 1045, 1090, 1123, and 1145 cm^{-1}) should appear in this region of the bone's spectrum but do not do so consistently when applying the second derivative technique (Rey et al. 1991b). This might occur because the technique can underestimate the number of underlying bands.[24]

The information from the underlying peaks reveals that atherosclerotic calcifications may contain acidic phosphate that may also substitute into the hydroxyapatite lattice. Again, this may indicate similarities between atherosclerotic calcification and bone biominerization mechanisms. There are also bands from more newly formed, nonstoichimetric apatite and more mature, stoichiometric apatite within each sample of the two types of tissues. This suggests that as in bone, the mineral in atherosclerotic calcifications is not formed at the same time but, instead, are deposited with time.

No apparent trends exist between the bands and the mineral-to-matrix ratio or the degree of crystallinity and maturity. In other mineralized tissues, Paschalis et al.

[24] See discussion in Section 5.2.5

correlated the area ratios of the 1020 cm^{-1}-to-1030 cm^{-1} bands to the degree of crystallinity and maturity (Paschalis et al. 1996). However, attempts at curvefitting the v_1, v_3 phosphate peak using Moffat software (D.J. Moffat, National Research Council of Canada, Canada) failed because the code could not converge and hence, the area ratios of the 1020 cm^{-1}-to-1030 cm^{-1} bands could not be measured.

5.2.7. Limitations of Study

This research has several limitations that should be considered. Bone is a very heterogeneous tissue and its mineral content varies with age, anatomical location, and site even within the same bone sample (Grynpas et al. 1993; Paschalis et al. 1996). This may also be true for atherosclerotic calcifications. Since the bone samples and atherosclerotic calcifications in this study were ground and only one spectrum was taken per sample, trends within each tissue type must be considered carefully because there is no data on the spread of data for each sample.

Errors may also have occurred in the measurement of the mineral-to-matrix ratio and carbonate-to-mineral ratio since protein has been found to exist within the v_1, v_3 phosphate region, potentially making the area under the v_1, v_3 phosphate peak larger than it actually is. This may also obscure the presence of underlying bands in the v_1, v_3 phosphate region.

FTIR also has a disadvantage. Since the technique requires that samples be ground, this eliminates the possibility of detecting spatial variations. FTIR *imaging* and micro-FTIR, however, are alternatives that can be used to map spatial variations with a resolution as small as 7 μm. This technique could provide more evidence to determine

whether atherosclerotic calcifications have local variations in mineral content and crystallinity and maturity, thus providing clues about how the calcifications develop.

5.3. Conclusions

Using FTIR, this study compared the composition of trabecular bone to atherosclerotic calcifications. The results provide evidence that both of these mineralized tissues are similar in composition. The mineral phase in both tissues is mainly composed of carbonate hydroxyapatite though, as in bone, atherosclerotic calcifications may also have acidic phosphate substitutions. The measurements taken in this study also provide guidelines for future work and suggest that the mineral content and crystallinity and maturity of late-stage atherosclerotic calcifications may be higher than that of bone. However, future work should systematically study the mineral content, composition, and crystallinity of atherosclerotic calcifications to determine if there are variations that depend on anatomical sites, patient's age, calcification age, and location within the calcification. This would provide more information on the initiation, development, and maturation of atherosclerotic calcifications and hence the etiology of atherosclerotic calcifications.

5.4. References

Biltz, R. M.; Pellegrino, E. D.; and Letteri, J. M. 1981. Skeletal carbonates and acid-base regulation. *Mineral and Electrolyte Metabolism* 5(1): 1-7.

Boskey, A. L. et al. 1992. Applications of Fourier-transform infrared (FTIR) microscopy to the study of mineralization in bone and cartilage. *Cells and Materials* 2(3): 209-220.

Boskey, A. L. and Paschalis, E. P. 2000. Mineral and matrix quality and quantity in iliac crest biopsies from high- and low-turnover osteoporosis: An FTIR microspectroscopic study. *Osteoporosis International* 11: S59-S59.

Bostrom, K. et al. 1993. Bone morphogenetic protein expression in human atherosclerotic lesions. *Journal of Clinical Investigation* 91(4): 1800-1809.

Brown, W. E. 1966. Crystal growth of bone mineral. *Clinical Orthopaedics and Related Research* 44: 205-220.

Cazalbou, S. et al. 2004. Poorly crystalline apatites: Evolution and maturation in vitro and in vivo. *Journal of Bone and Mineral Metabolism* 22(4): 310-317.

Doherty, T. M. and Detrano, R. C. 1994. Coronary arterial calcification as an active process: A new perspective on an old problem. *Calcified Tissue International* 54(3): 224-230.

Ebenstein, D. 2002. Biomechanical characterization of atherosclerotic plaques: A combined nanoindentation and FTIR approach. Ph. D. Dissertation. UCSF/UCB Bioengineering Graduate Group, University of California, San Francisco and University of California, Berkeley.

Francis, M. D. and Webb, N. C. 1971. Hydroxyapatite formation from a hydrated calcium monohydrogen phosphate precursor. *Calcified Tissue Research* 6(4): 335.

Gadaleta, S. J. et al. 1996. Fourier transform infrared spectroscopy of the solution-mediated conversion of amorphous calcium phosphate to hydroxyapatite: New correlations between X-ray diffraction and infrared data. *Calcified Tissue International* 58(1): 9-16.

Gadeau, A. P. et al. 2001. Time course of osteopontin, osteocalcin, and osteonectin accumulation and calcification after acute vessel wall injury. *Journal of Histochemistry & Cytochemistry* 49(1): 79-86.

Gijsbers, B. et al. 1990. Characterization of a Gla-containing protein from calcified human atherosclerotic plaques. *Arteriosclerosis* 10(6): 991-995.

Gong, J. K.; Cohn, S. H.; and Arnold, J. S. 1964. The density of organic and volatile and non-volatile inorganic components of cone. *Anatomical Record* 149(3): 319-324.

Grynpas, M. et al. 1993. Age and disease-related changes in the mineral of bone. *Calcified Tissue International* 53: S57-S64.

Hallsworth, A. S.; Weatherell, J. A.; and Robinson, C. 1973. Loss of carbonate during first stages of enamel caries. *Caries Research* 7(4): 345-348.

Herring, G. M. 1977. Methods for study of glycoproteins and proteoglycans of bone using bacterial collagenase: Determination of bone sialoprotein and chondroitin sulfate. *Calcified Tissue Research* 24(1): 29-36.

Hsu, H. and Camacho, N. 1999. Isolation of calcifiable vesicles from human atherosclerotic aortas. *Atherosclerosis* 143(2): 353-362.

Hsu, H. et al. 2000. Isolation of calcifiable vesicles from aortas of rabbits fed with high cholesterol diets. *Atherosclerosis* 153(2): 337-348.

LeGeros, R. Z. et al. 1987. CO_3-for-OH (type A) and CO_3-for-PO_4 (type B) substitutions in precipitated carbonate-apaties. *Journal of Dental Research* 66: 190.

LeGeros, R. Z. and LeGeros, J. P. 1983. Carbonate analyses of synthetic, mineral, and biological apatites. *Journal of Dental Research* 62: 259.

Legros, R.; Balmain, N.; and Bonel, G. 1986. Structure and composition of the mineral phase of periosteal bone. *Journal of Chemical Research Synopsis* 77(1): 8-9.

Leung, Y. C.; Walters, M. A.; and Legeros, R. Z. 1990. Second derivative infrared spectra of hydroxyapatite. *Spectrochimica Acta Part A: Molecular and Biomolecular Spectroscopy* 46(10): 1453-1459.

Maddams, W. F. and Southon, M. J. 1982. *Spectrochimica Acta Part A: Molecular and Biomolecular Spectroscopy* 38A: 459.

Manoharan, R. et al. 1993. Biochemical analysis and mapping of atherosclerotic human artery using FT-IR microspectroscopy. *Atherosclerosis* 103(2): 181-193.

Mason, J. T. and Oleary, T. J. 1991. Effects of formaldehyde fixation on protein secondary structure: A calorimetric and infrared spectroscopic investigation. *Journal of Histochemistry & Cytochemistry* 39(2): 225-229.

Ott, S. M. 2002. Histomorphometric analysis of bone remodeling. *In*: J. Bilezikian, L. Raisz, and G. Rodan, eds. *Principles of bone biology*. San Diego: Academic Press. pgs. 303-319.

Paschalis, E. P. et al. 1996. FTIR microspectroscopic analysis of human osteonal bone. *Calcified Tissue International* 59(6): 480-487.

Paschalis, E. P. et al. 1997. FTIR microspectroscopic analysis of normal human cortical and trabecular bone. *Calcified Tissue International* 61(6): 480-486.

Paschalis, E. P. et al. 2001. Spectroscopic characterization of collagen cross-links in bone. *Journal of Bone & Mineral Research* 16(10): 1821-1828.

Pleshko, N.; Boskey, A.; and Mendelsohn, R. 1991. Novel infrared spectroscopic method for the determination of crystallinity of hydroxyapatite minerals. *Biophysical Journal* 60(4): 786-793.

Rey, C. et al. 1989. The carbonate environment in bone mineral a resolution-enhanced fourier transform IR spectroscopy study. *Calcified Tissue International* 45(3): 157-164.

Rey, C. et al. 1990. Resolution-enhanced fourier transform IR spectroscopy study of the environment of phosphate ions in the early deposits of a solid phase of calcium phosphate in bone and enamel and their evolution with age, I: Investigations in theν_4 phosphate domain. *Calcified Tissue International* 46(6): 384-394.

Rey, C. et al. 1991a. Fourier transform infrared spectroscopic study of the carbonate ions in bone mineral during aging. *Calcified Tissue International* 49(4): 251-258.

Rey, C. et al. 1991b. Resolution-enhanced fourier transform infrared spectroscopy study of the environment of phosphate ion in the early deposits of a solid phase of calcium phosphate in bone and enamel and their evolution with age, 2: Investigations in the ν_3 phosphate domain. *Calcified Tissue International* 49(6): 383-388.

Rey, C. et al. 1995. Maturation of poorly crystalline apatites: Chemical and structural aspects in vivo and in vitro. *Cells and Materials* 5(4): 345-356.

Schmid, K. et al. 1980. Chemical and physicochemical studies on the mineral deposits of the human atherosclerotic aorta. *Atherosclerosis* 37(2): 199-210.

Tanimura, A.; McGregor, D. H.; and Anderson, C. H. 1986. Calcification in atherosclerosis, I: Human studies. *Journal of Experimental Pathology* 2(4): 261-273.

Termine, J. D. et al. 1973. Hydrazine deproteinated bone mineral. *Calcified Tissue Research* 12: 73-90.

Termine, J. D. and Posner, A. S. 1966. Infra-Red Determination of Percentage of Crystallinity in Apatitic Calcium Phosphates. *Nature* 211(5046): 268-270.

Termine, J. D. and Posner, A. S. 1967. Amorphous/crystalline interrelationships in bone mineral. *Calcified Tissue International* 1(1): 8-23.

Tomazic, B. B. et al. 1988. Physicochemical characterization of cardiovascular calcified deposits .1. Isolation, purification and instrumental analysis. *Atherosclerosis* 69(1): 5-19.

Yu, S. Y. 1974. Calcification processes in atherosclerosis. *In*: T. Clarkson, ed. *Arterial mesenchyme and atherosclerosis*. New York: Plenum Press. pgs. 403-425.

Table 5.1: Mineral properties of atherosclerotic calcifications and bone
Measurements of the phosphate peak area-to-amide I peak area, carbonate peak area-to-phosphate peak area, and degree of crystallinity of atherosclerotic calcifications and trabecular bone taken from their respective FTIR spectra

Samples		Phosphate Area/Amide I Area	Carbonate Area / Phosphate Area	Degree of Crystallinity
Atherosclerotic Calcifications				
Plaque A	A1	15.1	0.015	0.33
	A3	9.9	0.022	0.29
	A4	16.1	0.017	0.32
	A6	15.0	0.017	0.32
	A7	18.2	0.014	0.32
Plaque B	B1	15.9	0.018	0.31
	B2	14.4	0.019	0.29
	B4	14.5	0.014	0.33
	B5	14.4	0.021	0.29
	B6	12.6	0.011	0.34
Plaque C	C1	17.3	0.013	0.33
	C2	12.9	0.021	0.29
	C3	16.8	0.019	0.31
Average		**14.9***	**0.017**	**0.31†**
Standard Deviation		**2.2**	**0.003**	**0.02**
Bone				
Bone A		4.9	0.019	0.28
Bone B		4.6	0.018	0.26
Bone C		5.0	0.018	0.27
Bone D		5.3	0.022	0.28
Average		**5.0***	**0.019**	**0.27†**
Standard Deviation		**0.3**	**0.002**	**0.01**

* or † significant difference between atherosclerotic calcifications and bone results ($p<0.001$)

Table 5.2: Composition of atherosclerotic calcification as determined by FTIR
Second derivative peak positions of underlying bands in the v_1, v_3 phosphate region and their assignments attained from literature

Band (cm^{-1})	Assignments*	References
958.5	**~960 cm^{-1} v_1 PO^{3-}_4**	Bailey et al. 1989
980.7-985.5	**PO^{3-}_4 cm^{-1} in HA (980 cm^{-1}) or PO_3 symmetric stretch in Brushite (984 cm^{-1})**	Baddiel et al. 1966, Berry et al. 1967
997.1-1004.7	~1004 cm^{-1} v_3 asymmetric stretch	Bailey et al. 1989
1018.2-1022.1	**~1020 cm^{-1} v_3 PO^{3-}_4 from nonstoichiometric apatite**	Rey et al. 1991b
1028.9-1031.7	**~1030 cm^{-1} v_3 PO_4 from stoichiometric apatite**	Rey et al. 1991b, Baddiel et al. 1966
1043.3	~1044 cm^{-1} HPO^{2-}_4 containing apatite or type B carbonate apatite	Rey et al. 1995
1058.7-1062.6	**~1055 cm^{-1} v_3 PO^{3-}_4 in poorly crystalline apatite**	Bailey et al. 1989
1072.2-1074.2	**~1075 cm^{-1} v_3 PO^{3-}_4**	Bailey et al. 1989, Baddiel et al. 1966
1093.5-1103	~1096 cm^{-1} PO^{3-}_4 stoichiometric apatite	Bailey et al. 1989, Baddiel et al. 1966
1108.9-1112.7	~1112 cm^{-1} newly formed apatite (not detected in bone)	Rey et al. 1991b
1114.7-1116	~1116 cm^{-1} mature poorly crystalline HA	Rey et al. 1991b
1124.3-1128.2	~1125 cm^{-1} HPO^{2-}_4 containing apatite (not detected in bone)	Rey et al. 1995
1139.7-1149.4	~1145 cm^{-1} HPO^{2-}_4 containing apatite	Rey et al. 1991b

* Bands in bold always appeared in both bone and atherosclerotic calcifications while those in normal font did not always appear

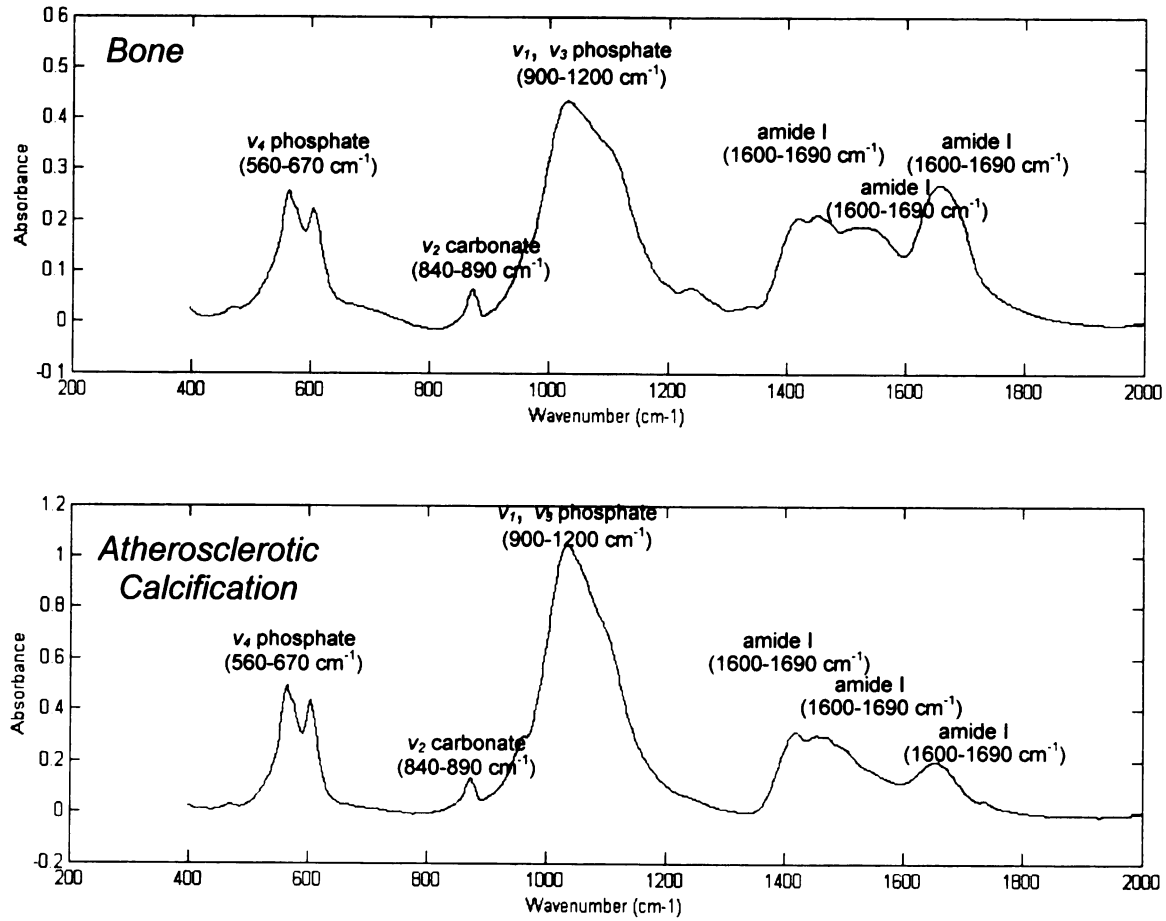

Figure 5.1: Typical FTIR spectra of bone and atherosclerotic calcification

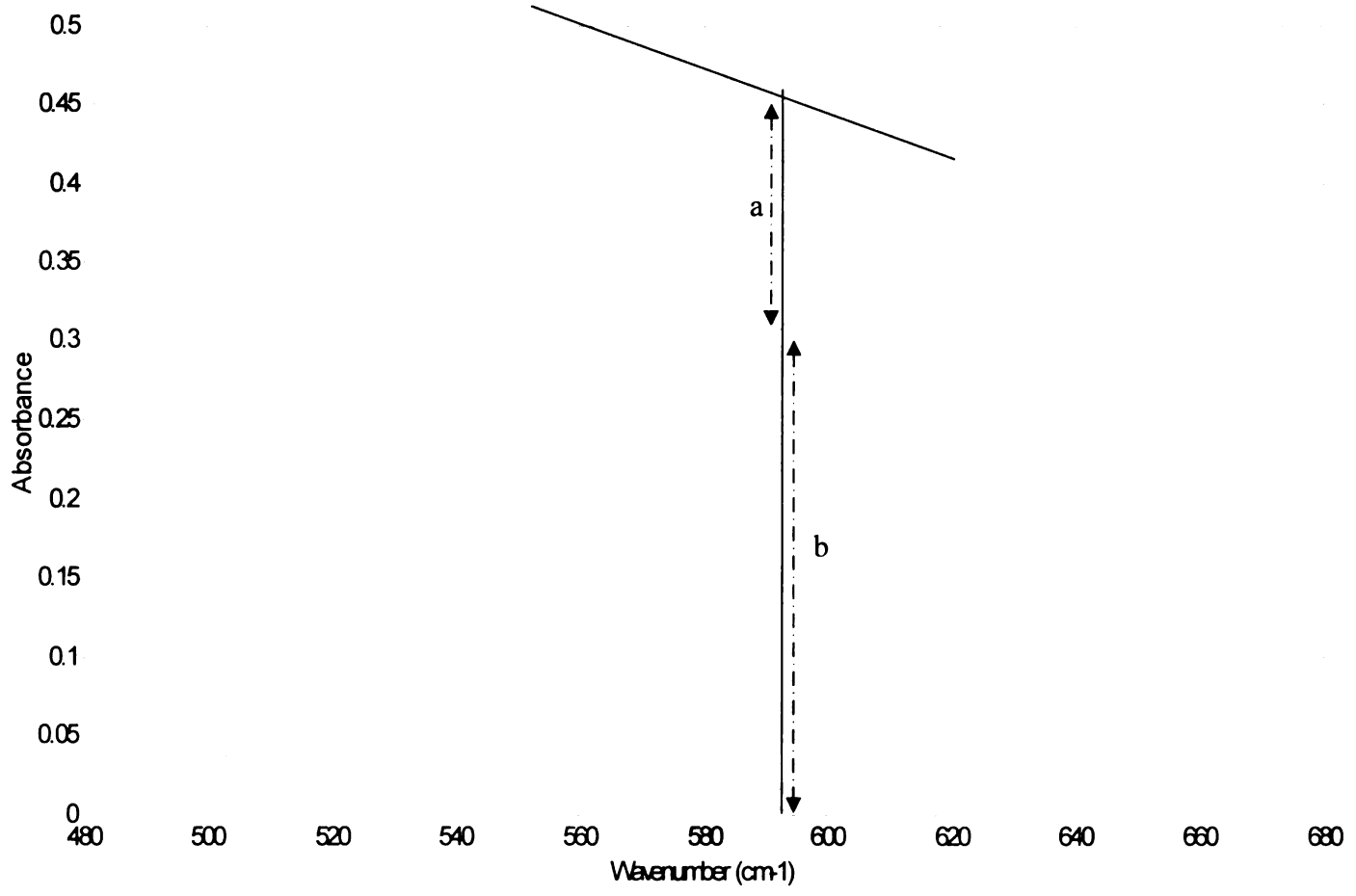

Figure 5.2: A close-up of the v_4 phosphate peak
Illustrates the two heights (*a* and *b*) of the v_4 phosphate peak of a calcification used to measure the degree of crystallinity/maturity

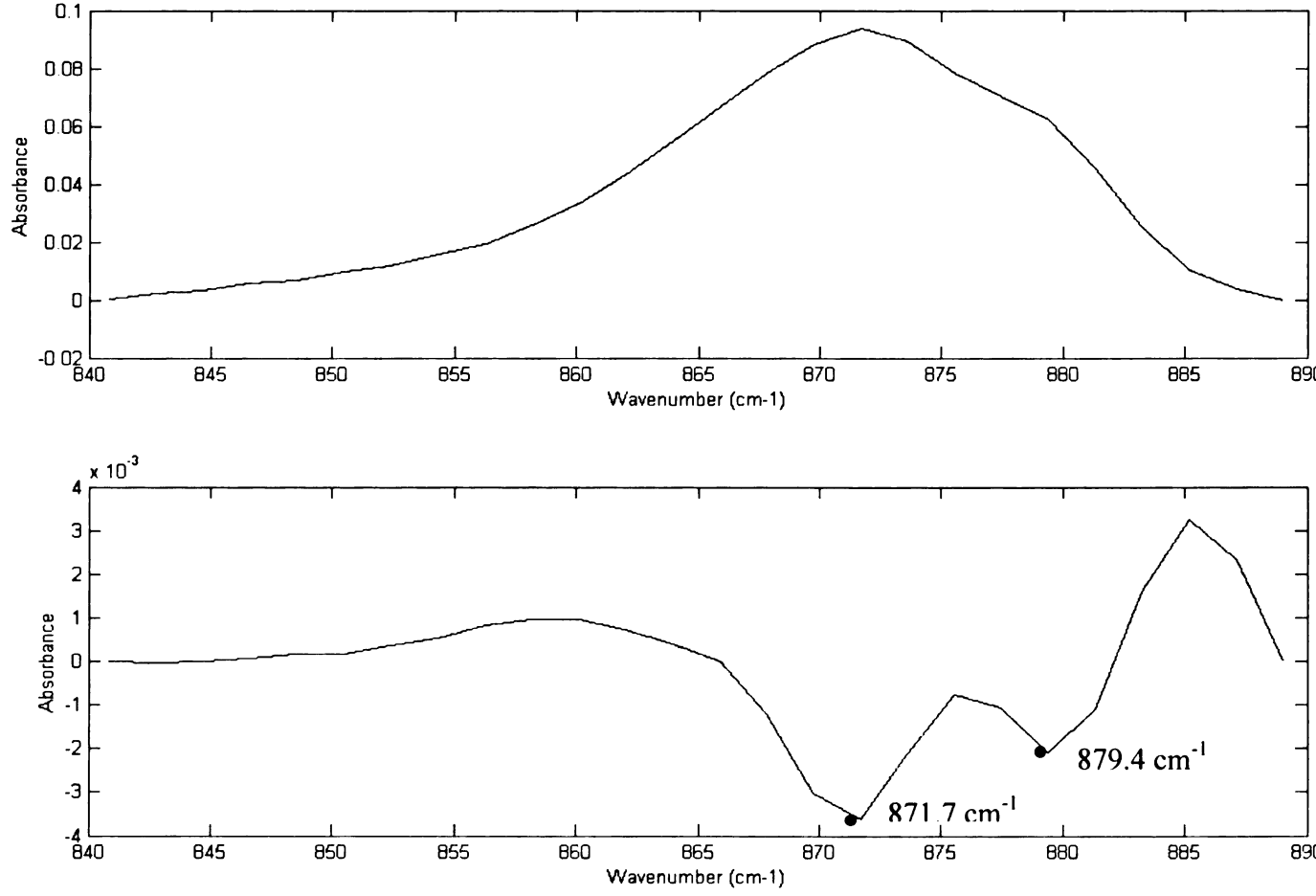

Figure 5.3: Second derivative of a FTIR spectra
(a) A close-up of a v_2 carbonate band of a calcification and (b) its second derivative

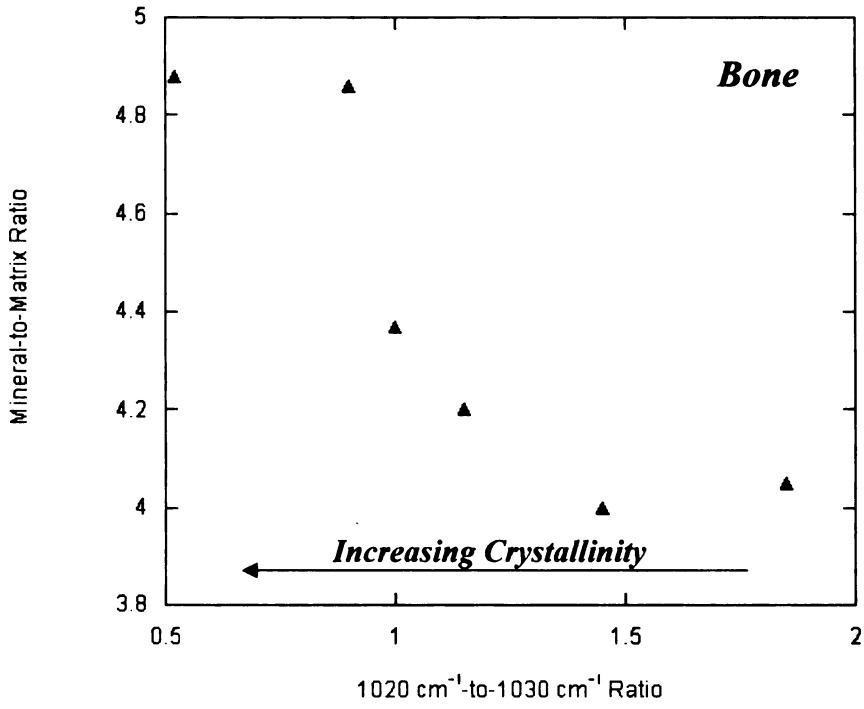

(a)

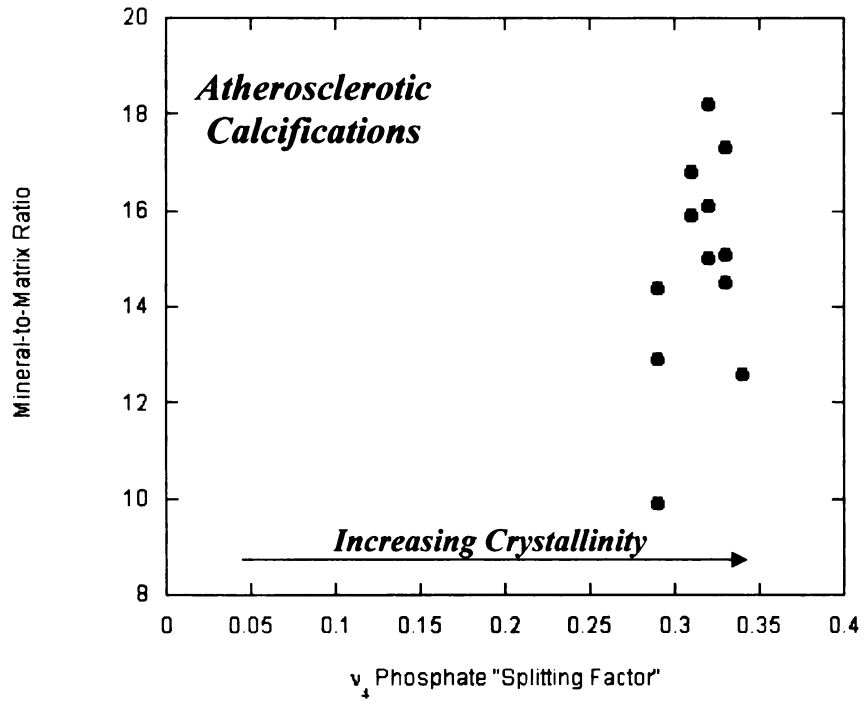

(b)

Figure 5.4: Mineral content versus crystallinity
Mineral content versus crystallinity for (a) bone (*Adapted from Paschalis et al. 1996*) and (b) atherosclerotic calcifications illustrating the increasing crystallinity with increasing mineral content

Chapter 6

Mineral-Density Distributions in Atherosclerotic Calcifications

6.0. Introduction

Atherosclerotic calcification deposits were initially thought to develop passively. Evidence now suggests that atherosclerotic biomineralization is an active process stimulated and inhibited by protein factors also found during bone biomineralization (Bostrom et al. 1993; Gadeau et al. 2001; Gijsbers et al. 1990). In bone, active biomineralization is controlled in a way that produces general growth patterns. For instance, trabecular bone is deposited in layers. The central core consists of the most mature mineral since it was deposited first and had time to mature; the outer layers consist of newly deposited mineral; and the outer most layer comprises the most recently deposited mineral (Figure 6.1). Since both atherosclerotic calcifications and bone are formed by an active process, it is plausible that, like bone, atherosclerotic calcifications may also have a distinctive mineral-deposition pattern.

General growth patterns are known. Small calcification particulates have been found in, as early as, type III lesions whereas granules and more solid, large deposits calcifications are in types IV through VII (Stary 2001).[25] This suggests that the particulates may form into granules that conglomerate and form into the more solid, larger deposits. The mechanics of mineral deposition are not known. If more specific

[25] Plaque types III through VII (according to Stary's classification) are described in detail in Chapter 2

mineral-deposition patterns were discovered, this information would be useful in the design of pharmaceutical therapies or devices to control the development and growth of atherosclerotic calcifications.

To examine whether a mineral-deposition pattern exists, this study uses micro-computed tomography (μCT) to qualitatively determine mineral-density distributions. This technique, reviewed in Chapter 3, has been extensively used to study the architecture and mineral-density distributions of bone (Bikle et al. 2001; Hara et al. 2002; Mulder et al. 2004; Nuzzo et al. 2002). Micro-computed tomography has also been used to measure the mass and volume of calcified plaques and, recently, to observe more general mineral distributions (Hoffmann et al. 2003; Langheinrich et al. 2004; Wolf et al. 2005).

In brief, the technique measures the mineral density of tissue by detecting how much x-ray energy the sample absorbs as measured by the linear attenuation coefficient. This coefficient can be converted to mineral density by calibrating the system with known mineral densities. In a reconstructed three-dimensional image, the different levels of attenuation are presented by the various grayscale levels (i.e., white being the most absorbent region and black, the least absorbent). Since the conversion of linear attenuation coefficients to mineral density is linear, the three-dimensional images of these coefficients can be used to assess the distribution of mineral densities.

6.1. Materials and Methods

6.1.1. Sample Preparation

In this study, three plaques were obtained from patients 50 years or older who underwent endarterectomy.[26] After surgery, the samples were placed in formalin until they were microdissected. Four calcifications were taken from plaque A; five, from plaque B; and one, from plaque C.

In preparation for imaging, the samples were placed in the base of a polymethymethacrylate cylindrical container and secured by foam. The container was then filled with distilled water since this medium scatters less x-ray signals than air. The container together with the samples, foam, and distilled water were placed in a vacuum until all visible air bubbles were removed and then imaged inside the μCT system (μCT-40, Scanco Medical AG, Bassersdorf, Switzerland).

6.1.2. Imaging

All micro-CT experiments were conducted using a μCT-40 (Scanco Medical AG, Bassersdorf, Switzerland) with an x-ray tube voltage of 70 kV and 180° acquisition. To discern whether the growth pattern revealed in the samples would, in fact, require high precision imaging, the first set of five samples was scanned with a high spatial resolution and a 20.48 mm field of view to create images reconstructed from 1,000 projections and formed with 12 μm cubical voxels. Since no growth pattern was discerned that needed such a high resolution, the spatial resolution was decreased to 36 μm for the second set of

[26] Section 4.1.1 explains how the samples were obtained and prepared.

samples. This set was measured at the lower spatial resolution and a 36.9 mm field of view to create images reconstructed from 500 projections and formed with 36 μm cubical voxels. In both sets of samples, the entire calcification volume was scanned. Volumes were reconstructed using a Feldkamp-cone-beam algorithm. In the image reconstruction, the linear attenuation coefficient is stored as a 16-bit number (e.g., -32,767 to 32,767). Hence, the linear attenuation coefficient was scaled by multiplying the coefficient by 4,096, and the result was stored as a positive integer.

Within each specimen, a region of interest was manually selected to isolate the calcification under analysis. To differentiate the atherosclerotic calcification from the background, a threshold scaled linear attenuation value (known as the threshold value) had to be selected; any voxel with a value below this threshold was deemed part of the background. For each specimen, the optimal threshold value was first selected visually by overlaying and comparing the edges of the thresholded image to the original image. The selected threshold value was that which best distinguished the calcification from the background. This method proved very subjective and sometimes it was difficult to decide which threshold value to use. If the threshold value is too high, the sample's volume is truncated and becomes smaller than it should be or, if the value is too low, the sample will include some of the background and be too large (Davis et al. 1975; Hara et al. 2002). So, instead, an automatic iterative thresholding method was used (Ridler et al. 1978).

Once the image was thresholded, the scaled linear attenuation coefficients (μ_s) were converted into mineral density data using the equation found during the mineral-density calibration[27]:

$$MD = \frac{423.8\mu_s}{4096} - 207.7 \tag{6.1}$$

where *MD* is the mineral density. Once converted, the mineral density data was used to calculate average mineral density for each sample. In addition, all the three-dimensional images displaying the distributions of the linear attenuation coefficients of the calcifications were qualitatively analyzed in color by restricting the color scale between zero (blue) and five (red) linear-attenuation-coefficient units. Since linear attenuation coefficients are related linearly to mineral density, these three-dimensional images illustrate the mineral-density distributions, with blue indicating the least mineral-dense regions and red, the most dense.

6.2. Results and Discussion

In the present study, most of the atherosclerotic calcifications are large, solid deposits (from 1 mm to 2.5 mm in the largest dimension). However, one calcification appears to be a conglomeration of several smaller granular spheres. The mineral densities of all these calcifications range from 0.74 g/cm^3 to 1.41 g/cm^3; the average mineral density being 1.19 g/cm^3 (Table 6.1). This range of mineral densities agrees with a recent study that used μCT to observe more general mineral distributions in whole calcified plaques (Wolf et al. 2005). In that study, the particulates had a mineral density of 0.77

[27] For a description of the procedures used to correct for beam hardening and to conduct mineral-density, see Chapter 3.

g/cm^3; the sheet-like regions had a mineral density of 1.02 g/cm^3; and the sclerotic regions, 1.46 g/cm^3, though overall the average mineral-density measurements ranged from 1.26 g/cm^3 to 6.23 g/cm^3 (Wolf et al. 2005). Similarly, in the present study, the least dense calcification comprises a conglomerate of granular spheres, with a mineral density of 0.74 g/cm^3. Therefore, once the calcifications are classified by shape, the values of the average mineral densities are more in agreement with those of the present study.

Similar to the study by Wolf et al., large differences are found between the mineral densities of calcifications within the same plaque (0.67 g/cm^3 in this study and 0.69 g/cm^3 in that by Wolf et al.) (Wolf et al. 2005). This confirms the previous FTIR study (Chapter 5) in which mineral-to-matrix-area ratios of the infrared absorption peaks (which have been correlated to mineral density) indicate that the mineral content of calcifications varies even from within the same plaque. If the mineral density indicates mineral maturity (i.e., regions with a high mineral density have older, more mature minerals), then the variations of mineral density within plaques may be used to study whether some regions within plaques are especially prone to mineral deposition. This topic needs further research.

Of the three-dimensional images containing mineral-density distributions, two types of growth patterns are distinguishable within each calcification. Very clear sedimentary-like[28] mineral deposition appears in three of the ten calcifications (Figure 6.2).[29] These calcifications possess an edge containing the highest mineral density

[28] The term sedimentary-like was used to indicate deposition that occurs in layers forming on top of each other in one direction.

[29] To clarify, in the three-dimensional image, the highest regions of linear attenuation coefficient (hence, the more dense and mature regions) are colored in hues closer to red while the less dense and more newly deposited mineral are colored in hues further away from red.

whereupon more recently deposited mineral is added. That edge is consistently found on the same side regardless of the angle at which the sample is cross-sectioned (Figure 6.2). This suggests that, within the plaque, some regions are more prone to mineral deposition.

The second, less common growth pattern is present in the spherical granules that had apparently conglomerated. Although the resolution of the image was not high enough to produce a clear image of the spheres, some spheres clearly have cores with a mineral density higher than on their surface (Figure 6.3). This suggests that the granules began as a particulate upon which minerals were deposited concentrically outward. Once formed, the spheres seem to conglomerate. Since this type of calcification had the lowest average mineral density (0.73 g/cm^3), it is not clear whether it remains a conglomerate or solidifies into a single calcification and then experiences additional sedimentary-like deposition.

Besides the two growth patterns distinguished above, most of the calcifications have an amorphous mineral distribution indicating complex growth patterns. In some of these calcifications, it seems that separate calcified deposits may have amalgamated into a single calcification. Indeed, sometimes, large regions of newly deposited mineral exist *inside* the calcifications, suggesting the junction of different calcified deposits (Figure 6.4).

From this study, no conclusions can be made with absolute certainty about the growth pattern of atherosclerotic calcification. It is not clear whether there are two distinct types of growth patterns or if one growth pattern is actually the predecessor of the other. Another limitation to this study is the partial voluming and thresholding that affects the edge of the image; this is why no conclusions were made about the edge appearing to

have low linear attenuation coefficients. Since each voxel is a finite dimension, the edge voxels contain information about both the background and the sample. Thus, the voxels, along the edges have a lower linear attenuation coefficient than they should, make the edge voxels appear green in the image. This is what is known as partial voluming. In addition, the automatic iterative threshold method used may also affect the edge of the image since high threshold values truncate the boundary and makes the sampler smaller than it should be and low threshold values include some of the background and makes the sample larger than its actual volume (Davis et al. 1975; Hara et al. 2002). Errors may also have been introduced in the measurements of mineral density. Since 0.8 g/cm^3 was the highest concentration of the hydroxyapatite-resin mixture used in the mineral-density calibrations, the mineral density calibration equation (6.1) had to be used to extrapolate data for regions with mineral densities greater than 0.8 g/cm^3.

6.3. Conclusions

The present research corroborates the results of earlier studies[30] that seem to indicate that calcifications within the same plaque can have different mineral densities. This suggests that certain regions within the plaque are especially prone to biomineralization. The research found two patterns of calcification growth: concentric- and sedimentary-like deposition. However, no conclusions can be made about whether these are indeed two types of growth patterns or of they are instead different stages of the same growth pattern. To accurately determine more detailed patterns of the growth of calcifications, it is essential to track and image the calcifications at different stages of growth. However, due to the high resolution required, it is currently not possible to this

[30] See chapters 4 and 5

do *in vivo*. If this were possible, it would provide information about the biomineralization growth process and whether certain regions are particularly prone to biomineralization. Since μCT can also be used to provide information about other tissue types, then *in vivo* μCT could be used to understand better the pathogenesis of atherosclerosis. This information would be useful in the design of pharmaceutical therapies or devices to control the development and growth of atherosclerotic plaques.

6.4. References

Bikle, D. et al. 2001. The skeletal structure of insulin-like growth factor I-deficient mice. *Journal of Bone and Mineral Research* 16(12): 2320-2329.

Bostrom, K. et al. 1993. Bone morphogenetic protein expression in human atherosclerotic lesions. *Journal of Clinical Investigation* 91(4): 1800-1809.

Davis, L. S.; Rosenfeld, A.; and Weszka, J. S. 1975. Region extraction by averaging and thresholding. *IEEE Transactions on Systems Man and Cybernetics* 5(3): 383-388.

Gadeau, A. P. et al. 2001. Time course of osteopontin, osteocalcin, and osteonectin accumulation and calcification after acute vessel wall injury. *Journal of Histochemistry & Cytochemistry* 49(1): 79-86.

Gijsbers, B. et al. 1990. Characterization of a Gla-containing protein from calcified human atherosclerotic plaques. *Arteriosclerosis* 10(6): 991-995.

Hara, T. et al. 2002. The influence of microcomputed tomography threshold variations on the assessment of structural and mechanical trabecular bone properties. *Bone* 31(1): 107-109.

Hoffmann, U. et al. 2003. Vascular calcification in ex vivo carotid specimens: Precision and accuracy of measurements with multi-detector row CT. *Radiology* 229(2): 375-381.

Langheinrich, A. C. et al. 2004. Atherosclerotic lesions at micro CT: Feasibility for analysis of coronary artery wall in autopsy specimens. *Radiology* 231(3): 675-681.

Mulder, L.; Koolstra, J. H.; and Van Euden, T. 2004. Accuracy of MicroCT in the quantitative determination of the degree and distribution of mineralization in developing bone. *Acta Radiologica* 45(7): 769-777.

Nuzzo, S. et al. 2002. Quantification of the degree of mineralization of bone in three dimensions using synchrotron radiation microtomography. *Medical Physics* 29(11): 2672-2681.

Ridler, T. W. and Calvard, S. 1978. Picture thresholding using an iterative selection method. *IEEE Transactions on Systems Man and Cybernetics* 8(8): 630-632.

Roschger, P. et al. 1997. Mineralization of cancellous bone after alendronate and sodium fluoride treatment: A quantitative backscattered electron imaging study on minipig ribs. *Bone* 20(5): 393-397.

Stary, H. C. 2001. The development of calcium deposits in atherosclerotic lesions and their persistence after lipid regression. *American Journal of Cardiology* 88(2A): 16E-19E.

Wolf, R. L. et al. 2005. Mineral volume and morphology in carotid plaque specimens using high-resolution MRI and CT. *Arteriosclerosis Thrombosis and Vascular Biology* 25(8): 1729-1735.

Table 6.1: Mineral density of atherosclerotic calcifications
Average and standard deviations of mineral density of atherosclerotic calcifications

	Calcification	Mineral Density (g/cm^3)	
		Average	Standard Deviation
Plaque A	A3	1.10	0.13
	A4	1.23	0.14
	A8	1.41	0.17
	A9	1.34	0.16
Plaque B	B1	0.74	0.20
	B2	1.23	0.13
	B5	1.19	0.13
	B6	1.17	0.15
	B7	1.15	0.19
Plaque C	C2	1.34	0.20
Overall Average		**1.19**	**0.16**

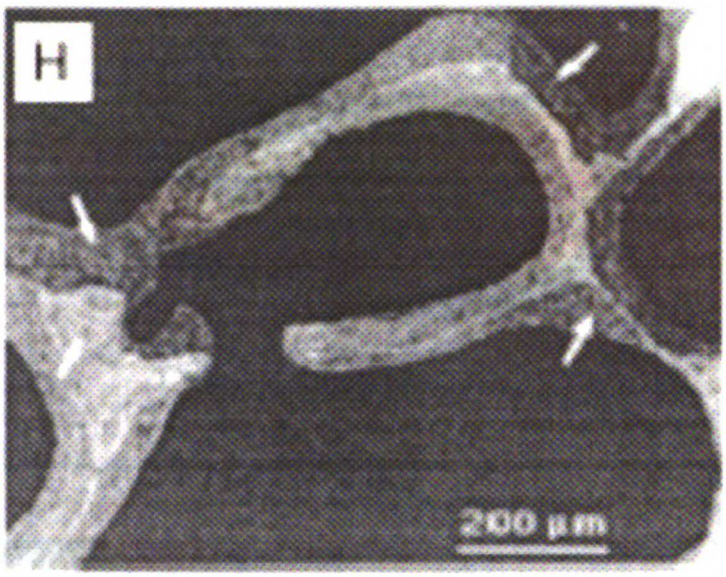

Figure 6.1: Degrees of bone mineralization
Quantitative backscattered electron image of the trabecular bone from the ribs of minipig illustrating that, in general, the bone is more mineralized in the middle of the trabecular bone (i.e., appears whiter) than near the outer surface (i.e., appears greyer) (*Source: Roschger 1997*)

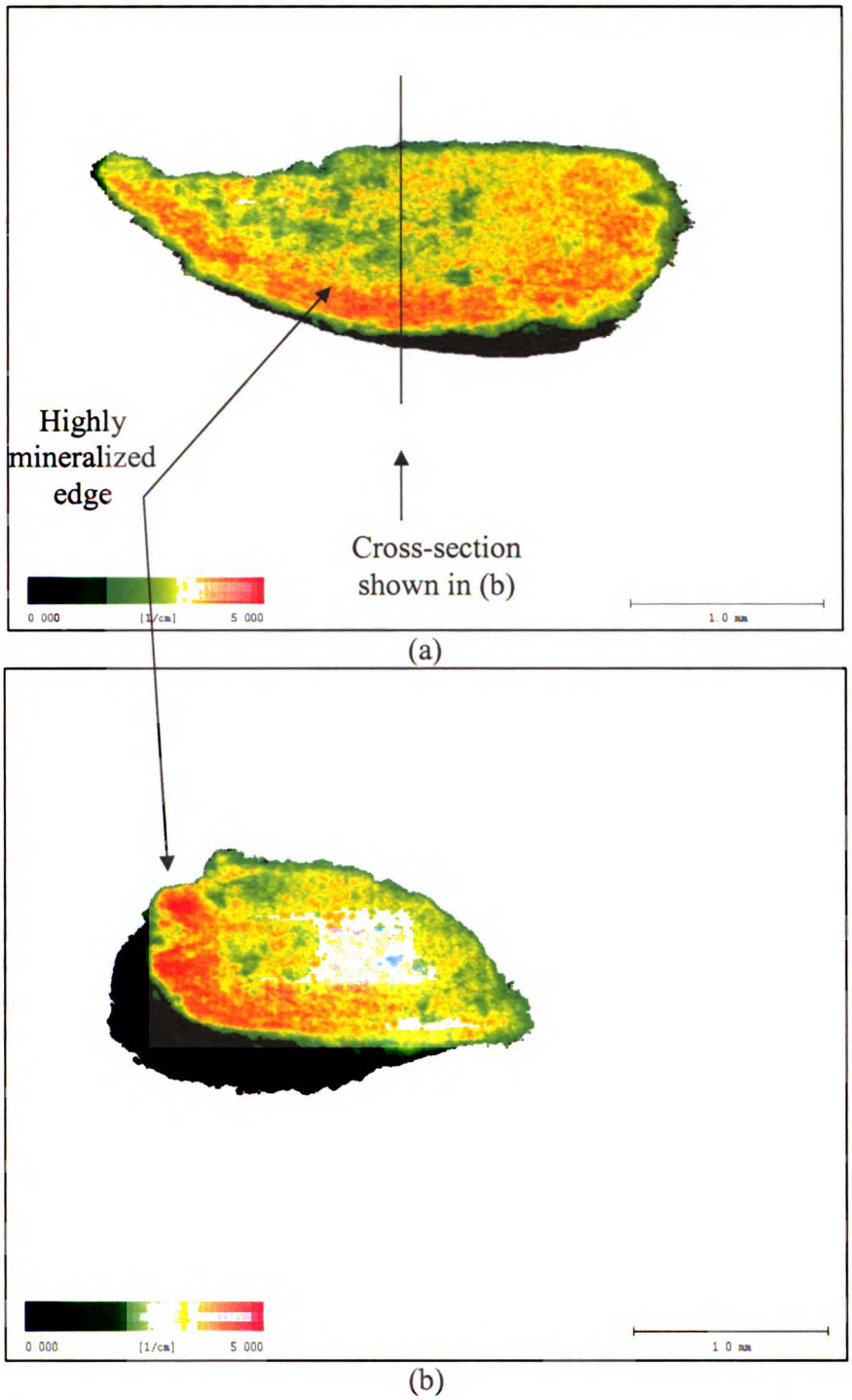

Figure 6.2: Sedimentary-like mineral deposition
Micro-computed tomography images of the linear attenuation coefficient values of an atherosclerotic calcification revealing sedimentary-like mineral deposition in two cross-sectional images of the same calcification

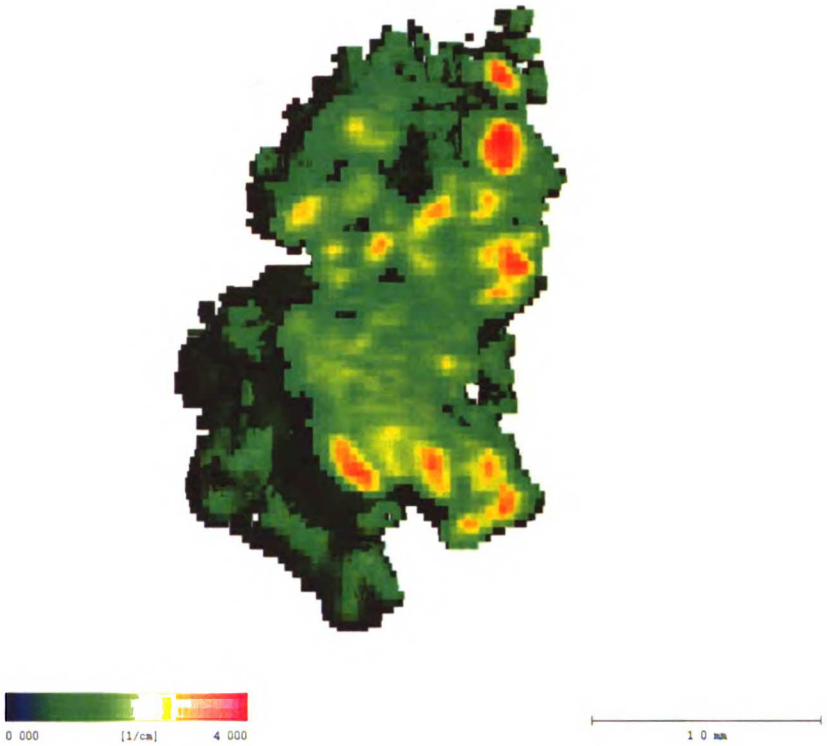

Figure 6.3: Concentric-like mineral deposition
Micro-computed tomography image of the linear attenuation coefficient values of an atherosclerotic calcification made up of many spherical granules illustrating concentric-like mineral deposition within the spheres. The scale was reduced to highlight differences in linear attenuation values.

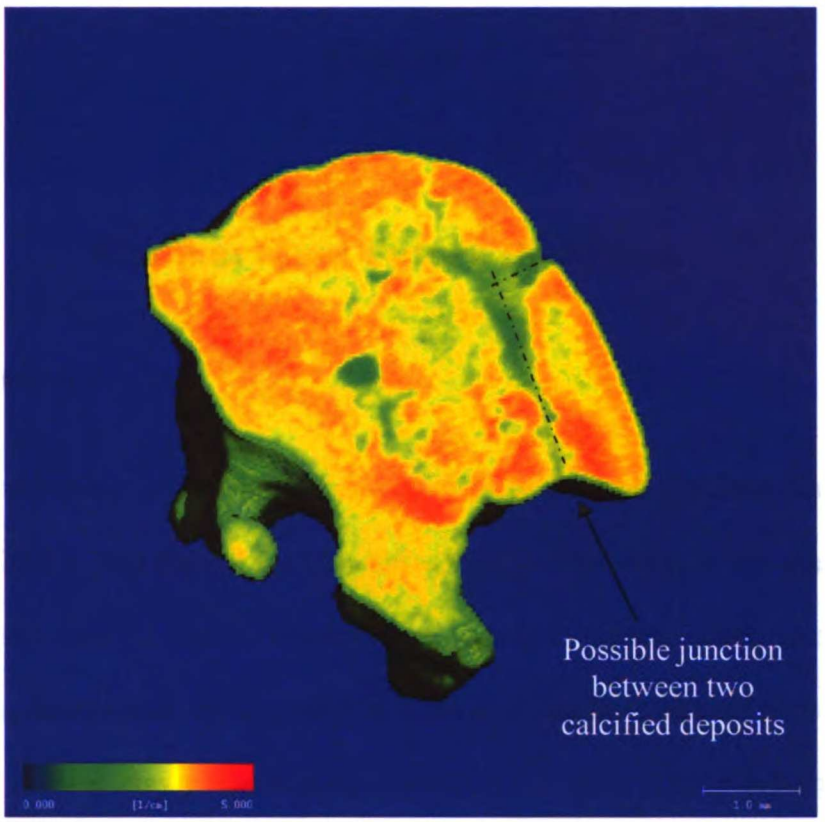

Figure 6.4: Complex growth patterns
Micro-computed tomography image of the linear attenuation coefficients for an atherosclerotic calcification illustrating complex growth patterns and possible union of separate calcifications.

Chapter 7

Summary and Future Directions

7.0. Summary

Atherosclerosis is the leading cause of death in the United States (American Heart Association 2005). This disease is characterized by the thickening of the arterial wall due to the accumulation of lipids, macrophages, smooth muscle cells, necrotic debris, calcifications, thrombosis and/or hematoma, which together form what is known as a plaque. This disease may cause a clinical event (such as a heart attack) if the plaque occludes a vessel or ruptures. If the plaque ruptures, a thrombosis may form on the plaque, perhaps also leading to vessel occlusion (Fuster et al. 1992). In either scenario, an occlusion in the coronary, cerebral, or peripheral arteries can cause insufficient blood flow to these areas and could cause, respectively, a heart attack, a stroke, or gangrene.

The factors that affect plaques' vulnerability to rupture are only partly known (Cheng et al. 1993; Falk et al. 1995; Lendon et al. 1991; Loree et al. 1994a; Richardson et al. 1989). Debate still exists about other possible rupture mechanisms such as the presence of calcifications within the plaque. It is not clear whether calcifications increase or decrease a plaque's probability of rupture. However, evidence suggests that calcifications affect the functionality and remodeling of arteries and sometimes complicates the treatments of diseased arteries (Demer 1991; Fitzgerald et al. 1992;

Fuessl et al. 2001; Lee et al. 1991; Nobuyoshi et al. 1991; Park et al. 1993; Salunke et al. 2001).

To better access how calcifications affect plaque vulnerability, arterial remodeling, and treatments for atherosclerosis, it is imperative to learn more about the composition and physical properties of these calcifications. Hence, the objective of the present study, comprising three projects, was to characterize the physical and compositional properties of atherosclerotic calcifications. To do so, the elastic mechanical properties were measured using nanoindentation for the future use in finite element models; the composition of calcifications was analyzed using Fourier transform infrared (FTIR) spectroscopy to determine the similarities and differences in the biomineralization process to that of bone; the nanoindentation was coupled with FTIR to determine structure-property relationships; and the mineral-density distribution of atherosclerotic calcifications was determined using micro-computed tomography (μCT) to evaluate the general patterns in the way calcifications grow.

In a previous nanoindentation study, the measured values for reduced elastic modulus of atherosclerotic calcifications had a large range (0.18 MPa to 21.3 GPa) seemingly due to surface roughness and poor isolation (Ebenstein 2002). The first project (Chapter 4) addressed these issues by performing more methodical microdissections and by microtoming the surfaces to reduce surface roughness prior to testing. These two methods proved to be an effective means for prepping the atherosclerotic calcifications for nanoindentation as evidenced by the narrower range of reduced elastic modulus (14.8 GPa to 25.7 GPa). These elastic properties can be used to create more accurate finite

element models used to study the development of atherosclerosis and in the design of its treatments.

The coupling of nanoindentation with FTIR in an attenuated total reflectance mode (FTIR-ATR) allowed for the analysis of the structure-property relationships of bone and atherosclerotic calcifications: the mineral content of the samples' surface was measured from FTIR-ATR spectra. The mineral content then compared to the average reduced elastic moduli of several indents taken on the same surface. The comparative results suggest that, as with other mineralized tissues, the mineral content of an atherosclerotic calcification affects its elastic properties with elastic modulus scaling with mineral content. Accurate means of making one-to-one correlations between elastic properties and mineral content will enable the development of quantitative structure-property relationships.

In the second project (Chapter 5), regular FTIR was used to compare the composition of trabecular bone and atherosclerotic calcifications as an initial step towards a better understanding of biomineralization from the perspective of composition. The analysis of the FTIR spectra revealed that both of these calcified tissues have a similar composition mainly composed of carbonate hydroxyapatite though both tissues can also have acidic phosphate substitutions. Analysis of the FTIR spectra also revealed that although the biomineralization processes between bone and atherosclerotic calcification may produce similar composition of tissues, other factors could raise the mineral content of atherosclerotic calcifications and make them more crystalline.

Finally, the third project (Chapter 6) used μCT to evaluate qualitatively the growth patterns of atherosclerotic calcifications. The three-dimensional images of the

calcifications' linear attenuation coefficients, which are linearly related to mineral density, revealed that, although most of the calcifications studied had complex growth patterns, some calcifications had very distinctive growth patterns, clearly manifesting either concentric- or sedimentary-like deposition. This information on calcification growth patterns, together with the results of their composition from Chapter 5, provides biochemists with more insight into the biomineralization process of atherosclerotic calcifications. More detailed studies of the composition and growth patterns could aid in the development of pharmaceutical therapies or devices for controlling the development and growth of atherosclerotic calcifications.

In all three studies, whether tested by nanoindentation, FTIR, or μCT, one finding was prevalent: the atherosclerotic calcifications had elastic properties and mineral densities that varied even within the same plaque. Hence, tissue calcification properties are inherently varied and modeling with such values must be done with caution.

7.1. Future Directions

The results of this work provide insight into the composition and properties of atherosclerotic calcifications. However, a limitation of this study is that there were a limited number of samples evaluated. Future work will include more samples for statistical analysis and validation. In addition, the study only focused on the properties of calcifications from atherosclerotic carotid arteries from patients over 50 years old. A more thorough understanding of atherosclerotic calcifications requires investigating whether the properties measured in the present study depend on anatomical sites, patient's age, calcification age, and location within the plaque.

7.1.1. Nanoindentation

Nanoindentation is intended for the study of elastic materials. Given the wide range in reduced elastic properties of the atherosclerotic calcifications studies, it is not clear whether that range is caused by variations in composition and/or anisotropy. Future work could use more recent nanoindentation techniques for measuring the material's anisotropy though this may be challenging since, unlike bone, atherosclerotic calcifications are small and do not display obvious directionality (Fan et al. 2002; Swadener et al. 2001). In addition, the nanomechanical properties of calcifications should be validated by other techniques. Though costly, ion milling[31] might be able to shape calcifications into standard testing geometries thus allowing other micro-tests to be performed. However, the process—usually done in a chamber cooled by nitrogen gas—may affect the material's mechanical properties and, thus, impair the validity of the results.

The present study's measurements of the calcifications' nanomechanical properties may have been affected by yet other conditions that need verification and, perhaps, alternative techniques for their avoidance:

- Since formalin fixation and dehydration affects the mechanical properties of bones, future work should also measure the nanomechanical properties of fresh, hydrated samples (Bushby et al. 2004; Currey et al. 1995; McElhaney et al. 1964; Sedlin et al. 1966).

[31] Ion milling uses accelerated ions of an inert gas, such as argon, to precisely sputter off material from a sample's surface, thus accurately shaping the material.

- To avoid the adhesive forces of the hydrating fluid that occur when the tip contacts the fluid surface, it is now possible to make fully submerged indents in a hydrating fluid.

- An embedding medium like polymethylmethacrylate (PMMA) might infiltrate into the calcification and affect its mechanical properties (Bushby et al. 2004). Ideally, it would be best not to embed the calcifications though this would not be easy since atherosclerotic calcifications are tiny and, without embedment, it would be difficult to handle the sample and smoothen its surface (as recommended for nanoindentation) (Hoffler et al. 1997; Xu et al. 2003).

Future work should also use a better means of independently determining the tip area function. With the technique used by the present study, the polycarbonate (unlike a true calibrating material) did not have a constant elastic modulus with depth throughout the range of indentation depths. To correct this, one should use either a better calibrating material or another technique like direct imaging of the tip by using atomic force microscopy (Briscoe et al. 1998).

Future research should also consider the viscoelasticity of atherosclerotic calcifications. Viscoelasticity was observed in the calcifications since significant differences were found in their reduced elastic moduli depending on the loading rate of the indentation. It would be better to perform dynamic tests on atherosclerotic calcifications since such tests would provide information about viscoelastic properties (Asif et al. 1999).

7.1.2. Spectroscopy

Though studies using FTIR show that formalin-fixation and embedding in PMMA have minimal effects on the composition of more mature calcified tissues, no specific studies have been conducted on atherosclerotic calcifications (Boskey et al. 1982; Pleshko et al. 1992). Therefore, future work should perform FTIR on fresh and non-embedded calcifications to obtain more accurate spectra. Again, not embedding the sample may present a challenge in prepping the sample for FTIR-ATR since this technique also requires a smooth sample surface. A smooth sample surface allows close contact between the sample and the FTIR-ATR crystal in order to decrease air gaps between the contacting surfaces since such gaps introduce noise into the signal.

Future research may apply Raman spectroscopy, which complements FTIR information since Raman measures the scattered signal caused by asymmetric bond vibrations while FTIR measures the absorbed signal. Raman spectroscopy has been used to study biological tissues especially because it has the advantage that a water peak is very weak and, unlike in FTIR, does not overlap with important peaks (Buschman et al. 2001a; Buschman et al. 2001b; Schrader et al. 1999). Hence, dehydration is less important in Raman spectroscopy (Schrader et al. 1999).

To obtain better structure-property relationships, it would be best to use micro-FTIR and/or micro-Raman spectroscopy. This would yield better one-to-one correlations between compositional information and nanomechanical properties. The present study used a Berkovich tip and produced indents of at most 4 μm^2 in area whereas the FTIR-ATR scanned an area of at most 6.3 mm^2. Both micro-FTIR and micro-Raman can

measure an area as small as 7 μm by 7 μm (49 μm^2). In addition, nanoindentation can be conducted with a 20 μm spherical tip to achieve an area closer to that measured by micro-FTIR and, thus, obtain more accurate one-to-one correlations between composition and nanomechanical properties. Though the one-to-one correlations may be appealing, caution should be taken because the sample preparation is not trivial. For instances, if thin samples are needed for spectroscopy, acquiring the thin samples may be challenging since calcifications are very brittle and it is difficult to obtain a solid microtomed section without pieces of the calcification falling off (Figure 4.4).

For a better understanding of the constituents of the mineral phase of atherosclerotic calcifications, future FTIR work should conduct more rigorous analysis of atherosclerotic calcifications at different stages of growth. In the present study, the constituents of the mineral phase of these calcifications were not always the same. This may be attributed to changes in mineral maturity and/or disease progression so studying the calcifications at different stages of growth and disease progression would provide information about theses changes. This information would be invaluable to biochemists that are trying to determine and control the constituents that are involved in the synthesis of atherosclerotic calcifications.

7.1.3. Micro-Computed Tomography

Future work should use μCT to scan entire plaques and evaluate mineral distributions in different age groups. Since older individuals tend to have more progressive disease, evaluating a group with a large range in ages would provide a better

understanding of calcification growth patterns. That information would help to evaluate the regions most susceptible to biomineralization.

In addition, future studies could correlate μCT to micro-FTIR or to high-resolution magnetic resonance imaging (MRI) (Wolf et al. 2005). Since both micro-FTIR and high-resolution MRI provide additional information about soft tissues, either technique can be used to obtain more accurate information about the regions most prone to biomineralization.

7.2. Concluding Remarks

Nanoindentation, FTIR, and μCT have proven to be valuable tools in the characterization of atherosclerotic calcifications. The elastic properties obtained by nanoindentation provide information about the mechanical behavior of calcifications, which can be used in future finite element studies. Nevertheless, to thoroughly understand the mechanical properties of calcifications, other types of mechanical tests should be performed under conditions that are more realistic.

Finally, the present study also provides insight into structure-property relationships and the compositional similarities and differences between atherosclerotic calcifications and bone. A more rigorous investigation of the compositional properties affecting mechanical behavior might require the coupling of nanoindentation with micro-FTIR and/or micro-Raman spectroscopy. Moreover, by using calcifications from patients of various ages, further FTIR studies of composition and μCT studies of mineral density would provide additional insight into the development and progression of atherosclerotic calcifications.

7.3. References

Asif, S.; Wahl, K.; and Colton, R. 1999. Nanoindentation and contact stiffness measurement using force modulation with a capacitive load-displacement transducer. *Review of Scientific Instruments* 70(5): 2408-2413.

American Heart Association. 2005. Heart Disease and Stroke Statistics: 2005 Update. Report by the American Heart Association, Dallas.

Boskey, A. L.; Cohen, M. L.; and Bullough, P. G. 1982. Hard tissue biochemistry: A comparison of fresh-frozen and formalin-fixed tissue samples. *Calcified Tissue International* 34(4): 328-331.

Briscoe, B. J.; Fiori, L.; and Pelillo, E. 1998. Nano-indentation of polymeric surfaces. *Journal of Physics D: Applied Physics* 31(19): 2395-2405.

Buschman, H. P. et al. 2001a. Raman microspectroscopy of human coronary atherosclerosis: Biochemical assessment of cellular and extracellular morphologic structures in situ. *Cardiovascular Pathology* 10(2): 69-82.

Buschman, H. P. et al. 2001b. Diagnosis of human coronary atherosclerosis by morphology-based Raman spectroscopy. *Cardiovascular Pathology* 10(2): 59-68.

Bushby, A. J.; Ferguson, V. L.; and Boyde, A. 2004. Nanoindentation of bone: comparison of specimens tested in liquid and embedded in polymethylmethacrylate. *Journal of Materials Research* 19(1): 249-59.

Cheng, G. C. et al. 1993. Distribution of circumferential stress in ruptured and stable atherosclerotic lesions: A structural analysis with histopathological correlation. *Circulation* 87(4): 1179-1187.

Currey, J. D. et al. 1995. Effect of formaldehyde fixation on some mechanical properties of bovine bone. *Biomaterials* 16(16): 1267-1271.

Demer, L. L. 1991. Effect of calcification on in-vivo mechanical response of rabbit arteries to balloon dilation. *Circulation* 83(6): 2083-2093.

Ebenstein, D. 2002. Biomechanical characterization of atherosclerotic plaques: A combined nanoindentation and FTIR approach. Ph. D. dissertation. UCSF/UCB Bioengineering Graduate Group, University of California, San Francisco and University of California, Berkeley.

Falk, E.; Shah, P. K.; and Fuster, V. 1995. Coronary plaque disruption. *Circulation* 92(3): 657-671.

Fan, Z. et al. 2002. Anisotropic properties of human tibial cortical bone as measured by nanoindentation. *Journal of Orthopaedic Research* 20(4): 806-810.

Fitzgerald, P. J.; Ports, T. A.; and Yock, P. G. 1992. Contribution of localized calcium deposits to dissection after angioplasty an observational study using intravascular ultrasound. *Circulation* 86(1): 64-70.

Fuessl, R. T. et al. 2001. Vascular remodeling in atherosclerotic coronary arteries is affected by plaque composition. *Coronary Artery Disease* 12(2): 91-97.

Fuster, V. et al. 1992. Mechanisms of disease: The pathogenesis of coronary artery disease and the acute coronary syndromes, part 2. *New England Journal of Medicine* 326(5): 310-18.

Hoffler, C. E. et al. 1997. Evaluation of bone microstructural properties: Effect of testing conditions, depth, repetition, time delay, and displacement rate. *Proceedings of the 1997 Bioengineering Conference*, Sunriver, Oregon, USA. pgs. 567-568.

Lee, R. T. et al. 1991. Structure-dependent dynamic mechanical behavior of fibrous caps from human atherosclerotic plaques. *Circulation* 83(5): 1764-1770.

Lendon, C. L. et al. 1991. Atherosclerotic plaque caps are locally weakened when macrophages density is increased. *Atherosclerosis* 87(1): 87-90.

Loree, H. M. et al. 1994. Static circumferential tangential modulus of human atherosclerotic tissue. *Journal of Biomechanics* 27(2): 195-204.

McElhaney, J. et al. 1964. Effect of embalming on mechanical properties of beef bone. *Journal of Applied Physiology* 19(6): 1234-1236.

Nobuyoshi, M. et al. 1991. Restenosis after percutaneous transluminal coronary angioplasty: Pathological observations in 20 patients. *Journal of the American College of Cardiology* 17(2): 433-439.

Park, J. C.; Siegel, R. J.; and Demer, L. L. 1993. Effect of calcification and formalin fixation on in vitro distensibility of human femoral arteries. *American Heart Journal* 125(2 part 1): 344-349.

Pleshko, N. L.; Boskey, A. L.; and Mendelsohn, R. 1992. An FT-IR microscopic investigation of the effects of tissue preservation on bone. *Calcified Tissue International* 51(1): 72-77.

Richardson, P.; Davies, M.; and Born, G. 1989. Influence of plaque configuration and stress distribution on fissuring of coronary atherosclerotic plaques. *Lancet* 2(8669): 941-944.

Salunke, N. V. et al. 2001. Compressive stress-relaxation of human atherosclerotic plaque. *Journal of Biomedical Materials Research* 55(2): 236-241.

Schrader, B. et al. 1999. NIR Raman spectroscopy in medicine and biology: Results and aspects. *Journal of Molecular Structure* 481: 21-32.

Sedlin, E. D. and Hirsch, C. 1966. Factors affecting determination of physical properties of femoral cortical bone. *Acta Orthopaedica Scandinavica* 37(1): 29.

Swadener, J. G.; Rho, J. Y.; and Pharr, G. M. 2001. Effects of anisotropy on elastic moduli measured by nanoindentation in human tibial cortical bone. *Journal of Biomedical Materials Research* 57(1): 108-112.

Wolf, R. L. et al. 2005. Mineral volume and morphology in carotid plaque specimens using high-resolution MRI and CT. *Arteriosclerosis Thrombosis and Vascular Biology* 25(8): 1729-1735.

Xu, J. et al. 2003. Atomic force microscopy and nanoindentation characterization of human lamellar bone prepared by microtome sectioning and mechanical polishing technique. *Journal of Biomedical Materials Research Part A* 67A(3): 719-726.

Appendix A

Microdissecting and Embedding Calcifications

Version 2
January 25, 2004

Author: Dezba Coughlin
Principle Investigator: Lisa Pruitt

Summary: The following standard operating procedure (SOP) describes the procedure for microdissecting and embedding excised calcification. This SOP is adapted from Prof. Tony Keaveny's lab staining and embedding protocol for trabecular bone from March 5, 1997 developed by Sean M. Haddock and Tony Chen. NOTE: most of the protocol has been copied verbatim from their lab to ensure consistency.

Key Words: calcifications, microdissecting, embedding, specimen preparation, solutions, dehydration, ethanol, polymethylmethacrylate

I. INTRODUCTION

One downside of testing calcifications is that they are extremely small and thus, are hard to handle and test. Although nanoindentation allows for the testing of the mechanical properties of calcifications, it requires very smooth specimen surface. However, given calcification specimen size, it is extremely hard to achieve this smooth surface. Yet, we have found that if you embed the calcifications in PMMA rods, you are able to suspend the calcifications in this polymer and thus create a big enough sample that now allows you to grip the specimen and smoothen its surface either by microtoming or polishing its surface. The following procedure was adopted from Prof. Tony Keaveny's lab to obtain a fast-polymerization embedding process that would allow use to prepare our specimen's surface for microtoming or polishing and nanoindentation. This fast-polymerization process allows for minimal infiltration into the tissue, which is important in order to maintain the integrity of the tissue's mechanical properties.

II. METHODS

Excising and Microdissecting Calcifications

Materials: tissue safety equipment, tissue scissors, scalpel, tweezers, Sharpie, epindoff tubes, small rack for the epindoff tubes, saline, and (if you are transporting the specimen) a container with ice to store the specimen.

---

a. Take note of the patient's age and sex (if provided)
b. Put on gloves and eye protection and place the entire plaque on a tissue protection sheet
c. Locate calcifications with the aid of MR images and by physically finding them; calcified regions will feel very hard
d. Cut the plaque in the longitudinal direction with scissors
e. Use a scalpel or scissors to cut a square around the calcification. Then remove the calcification with the tweezers, scissors, and/or scalpel but try to keep the rest of the tissue in tact
f. Under a dissecting microscope, remove all fibrous tissue around the microdissected calcifications
g. Put the specimen in the epindoff tube with 10% buffered formalin and place in ice or refrigerator at 5°C until further use
    i. ***Note:*** Remember to label the sample, what type of specimen it is (e.g., calcification), date of excision from the patient, and what solution it is stored in

Dehydrating

Materials: tissue safety equipment, tweezers, Sharpie pen, epindorff tubes, rack for epindorff tubes, small beaker or vial for ethanol waste, pipette or dropper for formalin and each ethanol solution, and ethanol solutions (70%, 80%, 85%, 90%, 95%, 100%).

---

h. Put on gloves and eye protection and place the entire plaque on a tissue protection sheet and work under the fume hood
i. Label each pipette end or dropper with "formalin" or the "concentrations of each ethanol solution" so as not to mix the solutions
    i. Note: Do not mix the ends used for the different concentrations of ethanol and fill each epindorff tube at least 5 times higher than the height of the calcification
j. Remove the specimen form the formalin-filled epindorff tubes using tweezers or your hand and place it into a new epindorff tube with 50% ethanol solution for 12 hours
k. Change to 70% ethanol solution (EtOH) for 12 hours
l. Change to 80% EtOH for 12 hours
m. Change to 85% EtOH for 12 hours
n. Change to 90% EtOH for 12 hours
o. Change to 95% EtOH for 12 hours

p. Change to 100% EtOH for 12 hours
q. Change to 100% fresh EtOH for 12 hours

Embedding

Materials: tissue safety equipment, polymethylmethacrylate (PMMA), vacuum, flat bottom BEEM capsules, rack for flat bottom BEEM holder, Superglue, water heater, waste container for PMMA, Sharpie pen, pencil, tweezers, flat plastic circular bases (hole-punched from thin PET sheet), paper label, dropper or pipette, razor blade, container to hold the rack, a weight to hold down the rack, plastic wrap

---

r. Remove dehydrated specimen from the 100% EtOH solution
s. Measure the longest and shortest dimensions (approximate width, length, height, or diameter) and sketch shape and dimensions in your log book
t. Glue the specimens roughest (not flattest) end onto the center of the plastic circular bases with Superglue
u. Wait about 2 minutes for the glue to set
v. Place the bases into the BEEM capsule using tweezers (make sure the part without the calcification is touching the BEEM capsule's bottom so that the base lays flat within the capsule)
w. Cut thin, long pieces of white paper and write the name of the calcification on it with a pencil
x. Curl up the label by folding it around the pencil and then place it about midway in the BEEM capsule using tweezers
y. Rinse with PMMA:
    i. Pour PMMA into the capsule to at least five times height of calcification with a dropper or pipette
    ii. Place the capsule, without the lid, into the vacuum in a holding apparatus to avoid spilling
    iii. Connect the hose, leaving the valve open, to the vacuum and allow the pressure gauge to increase to 25 Hg.
    iv. Turn off the vacuum and close the valve at the same time
    v. Let the samples sit in the vacuum for 20 minutes
    vi. Open the valve slowly to let the air out

    Note 1: Use the vacuum under the hood

    Note 2: During the degassing, the caps of the vials *must be left off.*
z. Check to make sure that the calcifications are still centered and stuck to the plastic bases. If not re-glue and start again.
aa. Remove PMMA by removing it with a dropper and pouring it into a PMMA waste container. *Do not pour down the drain!*
bb. Repeat steps "y" through "aa" twice

    Note: Put PMMA solution in an extra capsule and place it in the vacuum chamber as well on the third vacuum cycle. This will be used to top off the specimens.
cc. Make sure the label is still about midway of the height of the capsule and along the edge. If not then reposition it.

dd. Top off the capsule using the vacuumed PMMA solution, leaving slight room for the cap (just enough so that it will be tall enough to fit into the microtome holder)

ee. *Carefully* put glue around the edges of where the caps will go and put on the capsule's caps WITHOUT shaking the capsules.
Note: Great care must be taken so that the specimens are not knocked out of their center position. Also, agitation can cause an increase in air bubble formation in the embedding.

ff. *Carefully* place the capsules in their stand and into the glass or plastic container that will hold the stand. This container should already be in the water heater. Make sure that this container is already filled with water up to about the capsule level when the stand is placed into the container.

gg. Fill the container with water just below the PMMA level

hh. Fold up a piece of paper towel to the size of a weight that will be placed over the capsules. This will absorb any humidity.

ii. Place the paper towel and then the weight over the capsules

jj. Cover the top of the beaker with plastic wrap

kk. Set the water heater to 35°C. Let the specimens cure for 48-72 hours.
Note: The water heater temperature needs to be controlled carefully. Overheating the PMMA will cause runaway polymerization. Make sure that the oven temperature has equalized before you place the specimens into it.

ll. Once polymerized, remove the stand from the water heater and the capsules from the stand

mm. To obtain the embedded samples, get a razor blade and carefully cut vertically all the way down two opposite edges and pull the two cut edges apart until the sample is loose enough to be taken out.

III. SOLUTIONS

Ethanol

Materials: chemical safety equipment, 100% ethanol, distilled water, beaker

---

a. For the ethanol solutions, mix the prescribed amounts in a beaker and transfer to glass containers.

Polymethylmethacrylate (PMMA)

Materials: tissue safety equipment, dibenzoylperoxide, PMMA stock solution, beaker, plastic wrap, magnet stirrer, stirring and heating plate

---

a. Add 2 g dried dibenzoylperoxide to 100 ml of PMMA stock (polymethyl-methacrylate monomer) solution in a beaker. It is best to make just enough for your experiment.

Note: *Please look at the section below for instructions on knowing whether the dibenzoylperoxide is dry.*

b. Cover the beaker with plastic wrap to prevent evaporation
c. Mix on magnet-stir-plate in a water bath with heat off (or set to low) and medium to low stir setting until there is no more visible dried dibenzoylperoxide powder. Keep under the fume hood.
d. Store in a dark, tightly capped glass bottle in the refrigerator to prevent polymerization
e. NOTE: Do not add new solution to any excess in storage container.

Drying Dibenzoylperoxide

a. Place dibenzoylperoxide/benzoylperoxide in the mini-desiccator with CaCl on the bottom. The desiccator is located under the fume hood. The process is complete when the dibenzoylperoxide appears as dry; this normally takes several days.
b. **Note:** - If the dessicator pellets are blue they are still good but if they are pink, they need to be replaced. This must be done prior to use in mixing solutions above.

UC
San Francisco
LIBRARY
UNIVERSITY OF CALIFORNIA · UNIVERSITY OF CALIFORNIA

7487203
3 1378 00748 7203

For reference
Not to be taken from the room.